

A spectroscopic study of Λ hypernuclei,
 $^{10}_{\Lambda}\text{B}$, $^{12}_{\Lambda}\text{C}$, $^{28}_{\Lambda}\text{Si}$, $^{89}_{\Lambda}\text{Y}$, $^{139}_{\Lambda}\text{La}$ and $^{208}_{\Lambda}\text{Pb}$,
 by the (π^+, K^+) reaction

(π^+, K^+) 反応による Λ ハイパー核,
 $^{10}_{\Lambda}\text{B}$, $^{12}_{\Lambda}\text{C}$, $^{28}_{\Lambda}\text{Si}$, $^{89}_{\Lambda}\text{Y}$, $^{139}_{\Lambda}\text{La}$, $^{208}_{\Lambda}\text{Pb}$,
 の分光学的研究

July 1984

Graduate School, University of Tokyo
 Doctor Thesis
 東京大学大学院理学系研究科、物理学専攻
 学位論文

Takayuki Hasegawa
 長谷川 尊行



①

A spectroscopic study of Λ hypernuclei,
 ${}^{10}_{\Lambda}\text{B}$, ${}^{12}_{\Lambda}\text{C}$, ${}^{28}_{\Lambda}\text{Si}$, ${}^{89}_{\Lambda}\text{Y}$, ${}^{139}_{\Lambda}\text{La}$ and ${}^{208}_{\Lambda}\text{Pb}$,
by the (π^+, K^+) reaction

Doctor thesis

Tomoyuki Hasegawa
Graduate School, University of Tokyo

June, 1994

Abstract

Hypernuclei, ${}^{10}_{\Lambda}\text{B}$, ${}^{12}_{\Lambda}\text{C}$, ${}^{28}_{\Lambda}\text{Si}$, ${}^{89}_{\Lambda}\text{Y}$, ${}^{139}_{\Lambda}\text{La}$, and ${}^{208}_{\Lambda}\text{Pb}$, were produced by the (π^+, K^+) reaction, and the hypernuclear mass spectra were measured with an energy resolution of 2 MeV (FWHM). The present thesis reports on systematic high-resolution spectroscopy over a wide mass-number range for obtaining a unified understanding of Λ hypernuclei. In particular, this represents the first attempt to resolve deeply bound states of heavy Λ hypernuclei whose mass number exceeds 89, in order to investigate the behavior of a Λ hyperon inside a nucleus. This study also aimed at a precise spectroscopy of light hypernuclei in order to study the ΛN interaction.

The experiment used a 1.06 GeV/c π^+ beam at the K6 beam line of KEK 12-GeV PS and the superconducting kaon spectrometer (SKS), which was newly constructed. This spectrometer features a large angular acceptance of 100 msr and a short flight path of 5 m together with a powerful kaon trigger system.

In the ${}^{12}_{\Lambda}\text{C}$, ${}^{10}_{\Lambda}\text{B}$ and ${}^{28}_{\Lambda}\text{Si}$ spectra, peak structure corresponding to core-excited states was resolved. The spectra were compared with calculations based on configuration-mixing shell models in order to understand the hypernuclear structure and to extract information concerning the ΛN interaction.

In the ${}^{89}_{\Lambda}\text{Y}$, ${}^{139}_{\Lambda}\text{La}$ and ${}^{208}_{\Lambda}\text{Pb}$ spectra, peak structure possibly reflecting the Λ shell structure was observed. These peaks could be attributed to angular-momentum stretched states of Λ -particle neutron-hole configurations: $[0g_{9/2}^{-1}, l_{\Lambda}]$, $[0h_{11/2}^{-1}, l_{\Lambda}]$ and $[0i_{13/2}^{-1}, l_{\Lambda}]$, respectively. In particular, peaks which could be interpreted as being deeply bound s_{Λ} states were identified. The obtained spectra were compared with DWIA calculations.

The mass-number dependence of the obtained Λ binding energies was well reproduced by a simple Woods-Saxon potential. In this respect, the present results are consistent with the independent single-particle picture and the distinguishability of a Λ hyperon in a nucleus.

Contents

1	Introduction	4
1.1	Interesting physics related to Λ hypernuclear spectroscopy	4
1.2	Historical background	5
1.3	(π^+, K^+) reaction	6
1.4	Present experiment	8
2	Experimental apparatus	9
2.1	Requirements	9
2.2	K6 beam line	11
2.3	Beam spectrometer	13
2.4	Scattered-particle spectrometer (SKS)	19
2.5	Trigger system	28
2.6	Data-acquisition system	31
2.7	Off-line analysis system	32
2.8	Targets	32
2.9	Data summary	33
2.10	Physics constants and parameters	34
3	Data analysis	35
3.1	Outline	35
3.2	Momentum of a beam particle	37
3.3	Momentum of a scattered particle	38
3.4	Scattering angle	40
3.5	Particle identification in SKS	40
3.6	Cross section	44
3.6.1	Efficiency	44
3.6.2	Systematic errors	53
3.6.3	Consistency of the $^{12}_\Lambda\text{C}$ ground-state cross section	53

3.7	Energy precision and resolution	56
3.7.1	Calibration data	57
3.7.2	Energy precision	62
3.7.3	Energy resolution	63
3.8	Background level	65
3.8.1	Overbound regions in the spectra	65
3.8.2	No-target (π^+ , K^+) data	65
3.8.3	K^+ decay	69
3.8.4	Summary	69
4	Experimental results	70
4.1	Hypernuclear mass spectra	70
5	Discussion	78
5.1	Outline	78
5.2	Light Λ hypernuclei	79
5.2.1	$^{12}_{\Lambda}\text{C}$	79
5.2.2	$^{10}_{\Lambda}\text{B}$	83
5.2.3	$^{28}_{\Lambda}\text{Si}$	84
5.3	Heavy Λ hypernuclei	88
5.3.1	$^{89}_{\Lambda}\text{Y}$, $^{139}_{\Lambda}\text{La}$ and $^{208}_{\Lambda}\text{Pb}$	88
5.4	Mass-number dependence of B_{Λ}	92
6	Summary	97
A	Magnetic field measurement of SKS	102
A.1	Introduction	102
A.2	Apparatus	102
A.3	Field measurement	106
A.4	Hall-probe calibration	107
A.5	Analysis	109
A.5.1	Field reconstruction	109
A.5.2	Internal consistency	110
A.5.3	Field subroutines	112
A.6	Summary	113
B	Monte-Carlo simulation of the SKS momentum resolution	114

C	Beam momentum correction	116
D	Acceptance of SKS	117
E	Binding energy of the $^{12}_{\Lambda}\text{C}$ ground state	121
F	Hypernuclear mass spectra as tables	122
G	S-factors for neutron pick-up reactions	129

Chapter 1

Introduction

1.1 Interesting physics related to Λ hypernuclear spectroscopy

A Λ hypernucleus is a many-body system comprising nucleons and a Λ hyperon. A Λ hyperon is free from the Pauli blocking by nucleons. Furthermore, the ΛN interaction is generally weaker than the NN interaction. Consequently, it forms a characteristic hadronic system which is different from an ordinary nucleus. As a first approximation, a Λ hyperon is considered to occupy various single-particle orbits independent of those of nucleons. Thus, Λ hypernuclear spectroscopy involves a study of new and unusual hadronic many-body systems, which have attracted our interest.

A Λ hypernucleus can provide information concerning the behavior of a baryon in a nuclear medium. It is well known that the independent single-particle picture can be successfully applied to the outer nucleon orbits of a nucleus [1]. However, the inner parts have not been well understood. It would be interesting to understand both the validity and limitation of the single-particle aspect deep inside a nucleus. This situation is related to an intriguing possibility of a manifestation of sub-nucleonic degrees of freedom. How does a baryon keep its identity and distinguishability in a nuclear medium? Are quark degrees of freedom necessary for their description? In an ordinary nucleus, deep-hole states could not provide us with clear spectroscopic information owing to their large widths. On the other hand, a Λ hyperon can serve as a good tracer for probing the inside, moving relatively freely within a nucleus. Thus, investigating Λ hypernuclear states embedded within a nucleus offers a good opportunity to understand the behavior of a baryon in a nuclear medium.

A Λ hypernucleus is a good tool for studying the ΛN interaction at low energy.

Understanding the nuclear force on the basis of sub-nucleonic degrees of freedom, such as mesons and quarks, has been one of the most interesting subjects. In order to study this subject, it is important to understand the ΛN interaction as well as the NN interaction. Although scattering experiments using a Λ hyperon beam would be the best way to investigate the ΛN interaction, such experiments have so far not been feasible because of practical difficulties due to limited beam intensities and the short life time of the Λ hyperon. Experimental data concerning the ΛN interaction are very limited at present [2, 3]. Instead, the Λ hypernucleus can provide invaluable information about the ΛN interaction.

1.2 Historical background

The Λ hypernucleus was discovered in an airborne emulsion in 1952 [4]. In both emulsion and bubble-chamber experiments, light hypernuclei ($A < 15$) have been identified mostly by using π^- decay modes [5]. The binding energies of their ground states have been obtained. As a result, it was found that the Λ potential depth is about two thirds of that in the nucleon case, and that the spin-dependent forces are small.

New experimental progress was initiated by an experiment employing counter technique at CERN in 1973 [6]. This technique is crucial for obtaining high-statistics hypernuclear spectra. Since then, several counter experiments have been carried out by the (K^-, π^-) reaction with K^- beams at CERN and BNL [7, 8, 9, 10, 11]. In these experiments, the beam momentum was chosen so that the momentum transfer should be small so as to maintain large cross sections. Because of the small momentum transfer, it strongly populates substitutional states, where a neutron is converted to a Λ hyperon having the same orbital angular momentum. By this reaction, in particular, p-shell hypernuclei have been intensively studied. The measured angular distribution helped state assignment. Then, for example, a precise comparison between the observed $^{12}_\Lambda\text{C}$ and $^{16}_\Lambda\text{O}$ spectra showed smallness of the l s splitting for Λ orbits [10]. Various p-shell hypernuclear spectra, such as that of $^{13}_\Lambda\text{C}$, have been compared in detail with theoretical calculations based on a configuration-mixing shell model [12]. They obtained successful agreement. These studies reconfirmed that the spin-dependent ΛN interaction is weak [13] and, that the weak-coupling picture is a good approximation for Λ hypernuclei.

On the other hand, (stopped K^-, π^-) reaction experiments using the counter technique were first carried out at CERN [6], and have subsequently been developed at KEK [14, 15, 16]. Various aspects of light Λ hypernuclei, for example the forma-

tion rate of hyperfragments, have been studied. This reaction has an advantage in its large cross section, but possesses some ambiguity and complexity originating in the K^- atomic structure [17].

For a unified understanding of Λ hypernuclei, high-quality and systematic spectroscopy is very important. However, the present experimental data are mostly limited to light hypernuclei. In this respect, experimental data of heavy hypernuclear bound states have been awaited, particularly to investigate the behavior of a Λ hyperon in a nuclear medium. The (π^+, K^+) reaction was thus proposed as being the best method to systematically study Λ hypernuclei over the entire mass-number range up to heavy hypernuclei, such as $^{208}_\Lambda\text{Pb}$, down to the s_Λ orbits [18].

1.3 (π^+, K^+) reaction

The (π^+, K^+) reaction is characterized by a large momentum transfer (as much as 0.4 GeV/c) that is comparable to the Fermi momentum as shown in Fig. 1.1. Owing to this large momentum transfer, the reaction most probably populates angular-momentum stretched states with the largest l neutron-hole configurations for all of the Λ orbits [19, 20, 21]. In addition, even highly excited Λ single-particle states are expected to maintain narrow widths of less than 0.5 MeV because of the relatively weak ΛN interaction and a centrifugal barrier due to the large angular momentum [21, 22, 23]. This situation is in contrast with the nucleon case, in which both the deep-hole states and the highly excited states are too broad to be observed as well-defined peaks. This selectivity and the narrowness can be used to resolve characteristic peak structure representing the Λ shell structure. In particular, deeply bound single-particle states could be observed as peaks. Then, a spectroscopic study of heavy Λ hypernuclear bound states would provide invaluable information about the inside of a nucleus.

A complementary role of the (π^+, K^+) reaction to the other methods should also be emphasized. The (π^+, K^+) reaction selectively populates angular-momentum stretched states for all of the Λ orbits. On the other hand, the (K^-, π^-) reaction favors substitutional states, because of its small momentum transfer. The (stopped K^-, π^-) reaction also has a sizable momentum transfer, but is not so selective as the (π^+, K^+) reaction owing to the complexity related to the atomic structure. Therefore, the characteristic selectivity produces different sets of hypernuclear states [17]. Thus, the (π^+, K^+) method is not only suitable for studying heavy hypernuclear bound states, but is also important for extracting new complementary spectroscopic

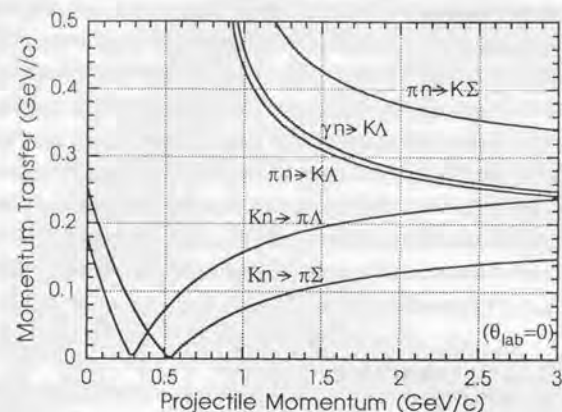


Figure 1.1: Momentum transfer to a hyperon as a function of the projectile momentum for various reactions.

information even from light hypernuclei. It should thus extend our systematic and unified understanding of Λ hypernuclei.

Experimentally, the selectivity and the usefulness of the (π^+, K^+) reaction were demonstrated at BNL [24, 25, 26] and KEK [27] up to a mass number of 89 with limited energy resolutions. The observed spectra exhibited characteristic peak structure reflecting the Λ shell structure. The results were consistent with the notion that a Λ hyperon occupies independent single-particle states in a nucleus and behaves as a distinguishable particle. Beyond a simple Woods-Saxon potential, a phenomenological Λ -nucleus potential based on a spherical Skyrme-Hartree-Fock approach has been studied in order to reproduce the mass-number dependence of the measured Λ binding energies [28]. Another approach has been developed starting from phenomenological ΛN interaction models in order to extract information concerning the ΛN interaction by global fitting to the binding energies [29, 30, 31]. More precise and systematic experimental data with a better energy resolution over a wider mass-number range, particularly of heavy hypernuclear deeply bound states, are highly desired and indispensable for conclusive discussions.

1.4 Present experiment

The present experiment was proposed [32] while aiming at a systematic spectroscopic study of Λ hypernuclei over a wider mass-number range up to 208 with a better energy resolution of 2 MeV(FWHM). The (π^+, K^+) reaction with the good energy resolution will resolve a series of Λ hypernuclear bound states for all Λ orbits down to s_Λ . It thus offers new systematic data which will precisely determine the average properties of the Λ -nucleus potential. In particular, this is the first attempt to directly observe deeply bound single-particle states of heavy hypernuclei whose mass number exceeds 89. Direct observations will shed some light on the behavior of a Λ hyperon deep inside a nuclear medium. Furthermore, even for light hypernuclei, new fine peak structure will be resolved owing to the characteristic selectivity of the reaction. New precise and complementary spectroscopic information will not only deepen our understanding of the Λ hypernuclear structure, but will also provide us with information about the ΛN interaction.

The present thesis comprises six chapters and seven appendices. Chapter 2 describes the experimental apparatus, chapter 3 the data analysis, chapter 4 the experimental results, chapter 5 physics discussions about the results, and chapter 6 a summary.

Chapter 2

Experimental apparatus

2.1 Requirements

For spectroscopic studies of nuclei, the energy resolution is one of the most important specifications of the experimental system. In heavy Λ hypernuclei, such as $^{139}_{\Lambda}\text{La}$ and $^{208}_{\Lambda}\text{Pb}$, a typical level spacing of Λ single-particle states is as small as 4 MeV. Therefore, in order to resolve the Λ shell structure of heavy Λ hypernuclei, an energy resolution of better than 2 MeV (FWHM) is indispensable. Such a good energy resolution is also required for a high-quality spectroscopic study of light Λ hypernuclei, in which core-excited states should be resolved. Experimentally, the energy resolution is determined by the momentum resolution for beam particles and scattered particles as well as the target energy-loss fluctuation. Consequently, pion and kaon spectrometers should have a momentum resolution of about 1 MeV/c (0.1%) while the energy-loss fluctuation should be kept at about 1 MeV.

In (π^+, K^+) experiments, we need a pion beam having a momentum range of around 1 GeV/c, because the cross section of the elementary process, $\pi N \rightarrow \Lambda K$, has a sharp maximum at about 1.05 GeV/c as shown in Fig. 2.1. Then, kaons are produced within a momentum range of around 0.7 GeV/c. These higher momentum ranges make it relatively difficult to achieve the required momentum resolution.

Even at the maximum, the production cross section of Λ hypernuclei by the (π^+, K^+) reaction is much smaller than that by the (K^-, π^-) and (stopped K^-, π^-) reactions. In particular, for heavy Λ hypernuclear bound states, it is as small as $\mu\text{b/sr}$. Although typically a two-order higher beam intensity of pions compared to that of kaons partly compensates for the smaller cross section, the kaon spectrometer should detect kaons with the highest possible efficiency. In this respect, the angular acceptance of the kaon spectrometer should be as large as possible. The larger

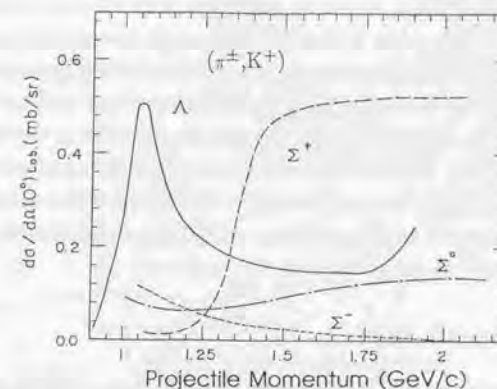


Figure 2.1: Cross section of the elementary process $\pi N \rightarrow \Lambda K$ as a function of the projectile momentum.

is the angular acceptance, the more difficult it is to maintain a good momentum resolution. We should therefore find a good compromise between a large angular acceptance and a good momentum resolution. Furthermore, in order to minimize kaon decay, the kaon spectrometer should be as short as possible. For example, about 60% of 0.7 GeV/c kaons decay after 5 m.

With the pion beam intensity being high, much more background particles other than kaons are produced through various pion-nucleus reactions, such as $(\pi, \pi'X)$ and (π, pX) . Therefore, a powerful kaon trigger is indispensable. In general, a kaon trigger in the GeV/c momentum range requires a careful consideration of a trigger counter which should have a sufficient pion rejection efficiency. At the off-line analysis stage, good kaon identification is also essential for obtaining background-free spectra.

These various requirements can be summarized as follows. The kaon spectrometer should have a momentum resolution of about 0.1% within a momentum range of around 0.7 GeV/c. Simultaneously, it should maintain a large angular acceptance and a short flight path. In addition, it must have a powerful kaon trigger and a good kaon-identification ability within this momentum range. On the other hand, the beam spectrometer must maintain a momentum resolution of about 0.1% in a momentum range around 1 GeV/c under a high counting rate of a few million per second.

The experiment was carried out with a 1.06 GeV/c π^+ beam at the K6 beam line of KEK 12-GeV PS. It should be noted that KEK-PS is presently a unique facility in the world except for BNL-AGS where a high intensity GeV/c π beam is available for nuclear physics experiments. To meet the challenging requirements, the superconducting kaon spectrometer (SKS) was designed and constructed [33, 34]. On the other hand, a QQDQQ magnet system was installed in the beam line as the pion spectrometer. Details concerning these experimental systems are described in the following sections. The data-acquisition system, the off-line analysis system, specifications of targets, a data summary, and physics constants and parameters used in the analysis are also described in this chapter.

2.2 K6 beam line

The K6 beam line is a general-purpose high-intensity beam line that can supply various secondary beams in the 1-GeV/c momentum range [35]. These beams are produced by 12-GeV protons on a production target. The primary proton beam was extracted for 1.4 sec in each 4.0 sec synchronized to the KEK 12-GeV PS operation cycle. A platinum rod of $\phi 6 \times 60$ mm² was used as the production target in this experiment. Figure 2.2 shows a schematic view of the K6 beam line. The beam line comprises two bending magnets, ten quadrupole magnets, a sextupole magnet, a DC separator with two correction magnets, and four slits. The slits are installed between D1 and Q1 (acceptance slit), between Q2 and Q3 (intermediate focus slit), between the DC separator and Q5 (momentum slit), and between Q6 and Q7 (mass slit).

Figure 2.3 shows the beam envelopes calculated with *Transport* [36] for the (π^+ , K^+) beam-transport condition. It is a special feature of the K6 beam line that there is a vertical focus point at the intermediate focus slit to reduce the background beam halos. The beam was achromatically focussed at the experimental target. The measured beam size was typically 6.0(H) \times 7.5(V) mm² in rms.

The central beam momentum was set at 1.06 GeV/c under the (π^+ , K^+) condition, as shown in Fig. 2.4. The beam intensity at the experimental target was adjusted to be about 3.0 M/spill in order to avoid a large decrease of the beam-spectrometer efficiency at high counting rates; it was not the available maximum intensity. The p/π^+ and e^+/π^+ ratios were measured to be typically 10 and 20%, respectively. The μ^+/π^+ ratio is estimated in section 3.6 to be about 6%. The K^+/π^+ ratio was estimated to be as small as 10^{-3} by using the Sanford-Wang formula [37].

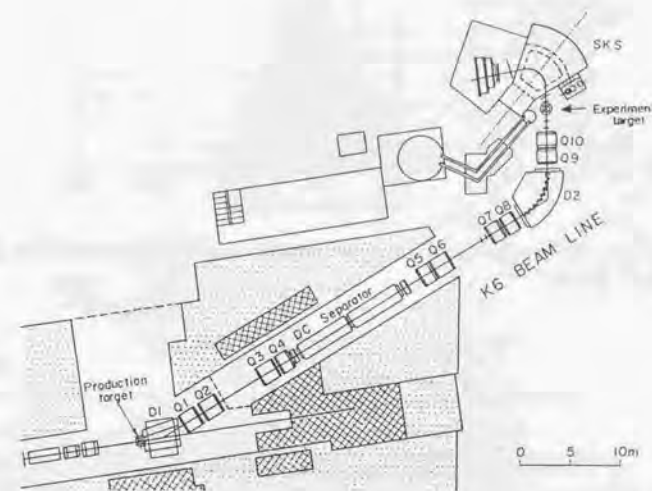


Figure 2.2: Schematic view of the K6 beam line of KEK 12-GeV PS.

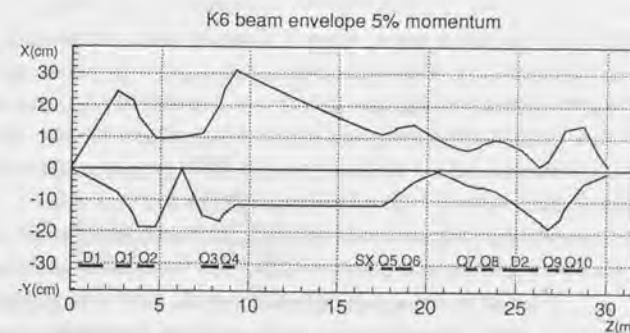


Figure 2.3: Beam envelopes of the K6 beam line for the (π^+ , K^+) beam-transport condition calculated by *Transport*.

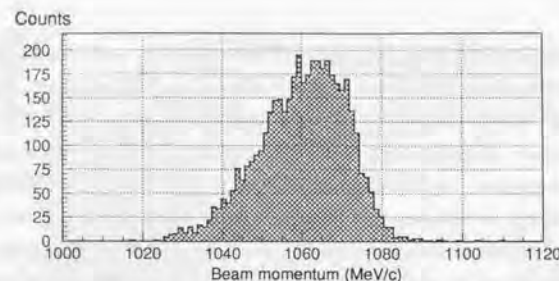


Figure 2.4: Momentum spectrum at the experimental target measured for a 1.06 GeV/c π^+ beam.

Momentum resolution	0.1% (FWHM)
Maximum momentum	1.1 GeV/c
Magnet configuration	QQDQQ
Bending angle	60°
Total length	9 m

Table 2.1: Design parameters of the beam-spectrometer system.

2.3 Beam spectrometer

As mentioned in section 2.1, the beam-spectrometer system is required to maintain a momentum resolution of 0.1% (FWHM) in a momentum range of around 1 GeV/c under a high counting rate of several M/spill. Table 2.1 shows design parameters of the beam spectrometer. Figure 2.5 shows a schematic view. It comprises a QQDQQ magnet system with four sets of drift chambers (BDC1-2-3-4) and trigger counters. The trigger counters comprise a segmented scintillation counter (BH1) as the time-zero counter, another scintillation counter (BH2) for proton rejection, and a Freon-gas Čerenkov counter (GC) for positron rejection.

The beam momentum is measured by the QQDQQ system with the drift chambers by using a transfer matrix, particle by particle. In order to minimize the multiple-scattering effect on the momentum resolution, the $\langle x|\theta \rangle$ term of the transfer matrix between BDC2 and BDC3 was set to be zero to the first order. A vacuum chamber was installed between BDC2 and BDC3 in the magnets. In addition, the drift chambers were made as thin as possible in substance. A Monte-Carlo simulation showed that the momentum resolution was 0.04% (FWHM) assuming $\sigma=300\mu\text{m}$

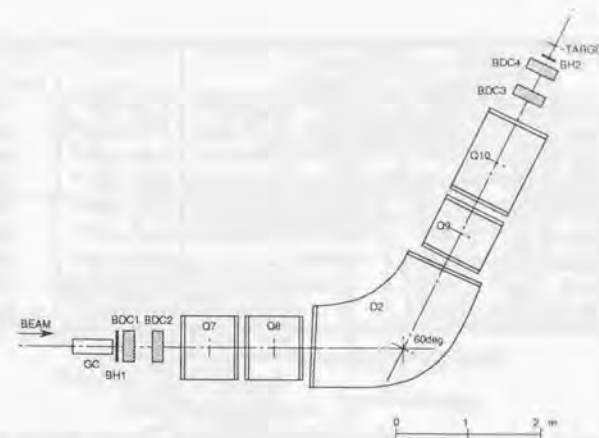


Figure 2.5: Schematic view of the beam-spectrometer system.

for the drift-chamber resolution. In reality, since the QQDQQ system was calibrated with SKS (as described in section 3.2), the resolution of the beam spectrometer may be comparable to that of SKS. The magnetic field of D2 was monitored during the experiment every 30 sec with a high-precision Hall probe¹ to correct its fluctuation in the off-line analysis. The fluctuation was less than $\pm 0.05\%$, which was due to that of the magnet current.

Specifications of the beam drift chambers are shown in Table 2.2. The four chambers have the same structure as that shown in Fig.2.6. To be used under a high counting rate, the sense-wire spacing was made to be short (5 mm), as shown in Fig.2.7. Each chamber included six layers of sense-wire planes ($xx'uu'vv'$), where vertical and $\pm 15^\circ$ tilted wire planes are denoted by x , u and v , respectively. The primed planes were half-cell displaced ones in order to solve the left-right ambiguity. To minimize multiple scattering, the material thickness was made to be as small as possible, as already mentioned. The sense and potential wires were made of gold-plated tungsten ($\phi 12.5\mu\text{m}$) and gold-plated copper beryllium ($\phi 50\mu\text{m}$), respectively. The cathode planes were made of $7.5\mu\text{m}$ kapton foils coated with $0.1\mu\text{m}$ aluminum on both sides and $0.0015\mu\text{m}$ chromium for preventing oxidization of the aluminum coating. The gas mixture was Ar (79%) + C_4H_{10} (17%) + Methylal (4%) at STP.

¹The Hall probe was of the same type as those used in the SKS field measurement (see appendix A).

Name	Area (cm)	Drift space (mm)	Wires	Thickness (L_R)	Resolution (μm in σ)
BDC1	$24^W \times 15^H$	2.5	$xx'uu'vv'$	1.79×10^{-3}	250
BDC2	$24^W \times 15^H$	2.5	$xx'uu'vv'$	1.79×10^{-3}	250
BDC3	$24^W \times 15^H$	2.5	$xx'uu'vv'$	1.79×10^{-3}	250
BDC4	$24^W \times 15^H$	2.5	$xx'uu'vv'$	1.79×10^{-3}	250
SDC1	$40^W \times 15^H$	2.5	$xx'uu'vv'$	1.79×10^{-3}	250
SDC2	$56^W \times 15^H$	2.5	$xx'uu'$	1.18×10^{-3}	250
SDC3	$100^W \times 100^H$	21	x	0.53×10^{-3}	250
SDC4X	$100^W \times 100^H$	21	$x \times 6$	1.05×10^{-3}	250
SDC4Y	$100^W \times 100^H$	21	$y \times 6$	1.05×10^{-3}	250

Table 2.2: Specifications of the drift chambers.

The readout system is schematically shown in Fig.2.6. Typical plateau curves and operation high voltage are shown in Fig.2.8. A typical intrinsic resolution was $\sigma=250 \mu\text{m}$ for one plane, as shown in Fig.2.9. The figure shows the drift-length sum for a pair of planes displaced by a half cell to each other, where the width of a peak represents $\sqrt{2}$ -times the intrinsic resolution.

Specifications of the three trigger counters are given in Table 2.3. The beam hodoscope (BH1) was used as the time-zero counter. To avoid degeneration of the time resolution under the high counting rate, it was divided into seven vertical segments. Each segment was equipped with photomultipliers having three-stage booster on both ends (Fig.2.10). The time resolution of BH1 is described in section 2.4. A coincidence of BH1 with BH2 rejects not only proton contamination in the beam, but also background particles which cannot pass through the QQDQQ system; the single counting rate of BH1 was twice as high as that of BH2. Since BH2 was placed between the beam spectrometer and the scattered-particle spectrometer, it was made thin (2 mm) in order to minimize the energy-loss straggling by this counter. The gas Čerenkov counter (GC) vetoed e^+ contamination in the beam with a rejection efficiency of better than 99.9%; the mean photoelectron number was measured to be about eight.

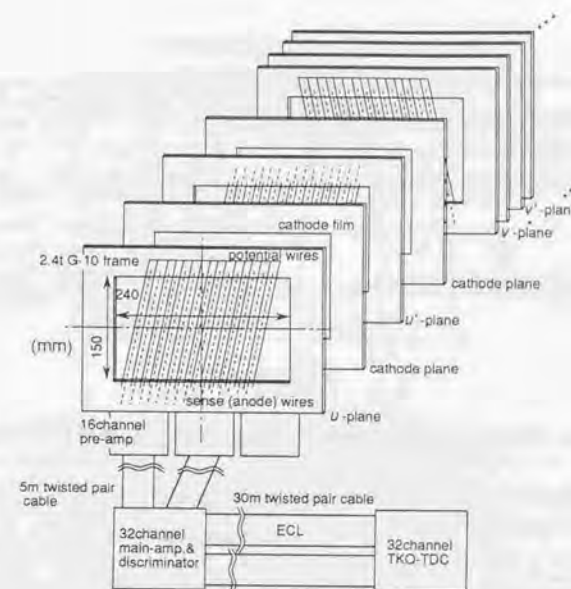


Figure 2.6: Schematic figure of the beam drift chamber and the readout system.

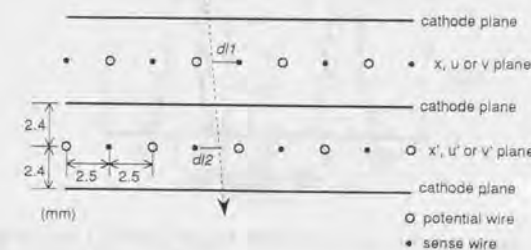


Figure 2.7: Cell structure of the beam drift chambers.

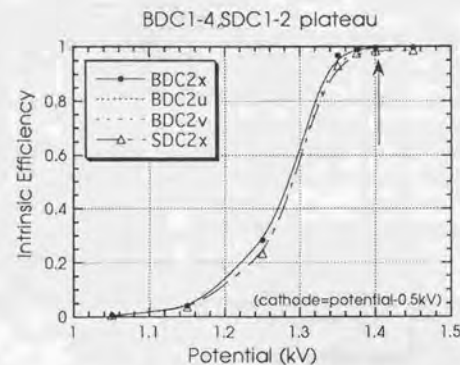


Figure 2.8: Typical plateau curves and operation high voltage of BDC1-4 and SDC1-2.

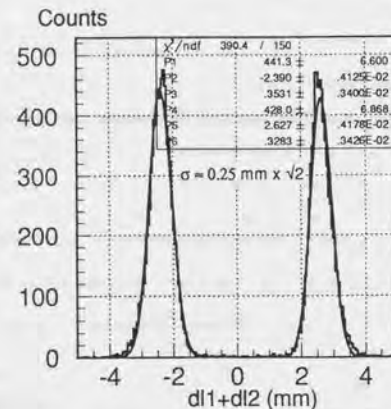


Figure 2.9: Typical distribution of the drift-length sum for a pair of planes which are displaced by a half cell to each other, measured for a 1.06 GeV/c π^+ beam. The width of the peaks represent the intrinsic position resolution.

Name	Sensitive area (cm)	PMT (Hamamatsu)	etc.
GC	$\phi 20 \times 29^L$	R1584-02 \times 1	Freon-12, n=1.00245
BH1	$19^W \times 9^H \times 0.5^T$	R1450 \times 14	7-segments, 3-stage-booster
BH2	$8^W \times 10^H \times 0.2^T$	H1161 \times 2	1-segment, 3-stage-booster
TOF	$105^W \times 100^H \times 3^T$	H1949 \times 30	15-segments
AC1	$105^W \times 120^H \times 9^T$	R1584-02 \times 18	n=1.06
AC2	$140^W \times 140^H \times 12^T$	R1584-02 \times 20	n=1.06
LC	$140^W \times 140^H \times 4^T$	H1949 \times 28	n=1.49, 14-segments

Table 2.3: Specifications of the counters.

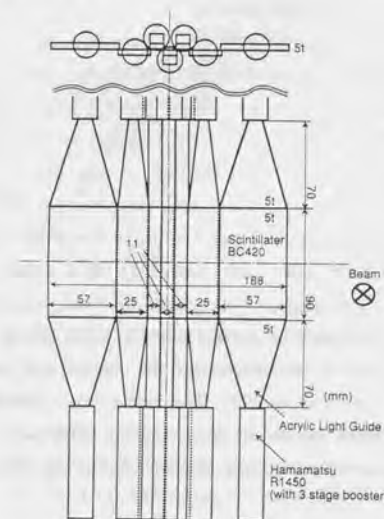


Figure 2.10: Schematic view of BH1.

Momentum resolution	0.1% (FWHM)
Angular acceptance	100 msr
Flight path (central trajectory)	5 m
Momentum coverage (2.2 T mode)	0.7 ± 0.1 GeV/c
Maximum momentum (3.0 T mode)	1.1 GeV/c
Bending angle	100°
Gap	50 cm

Table 2.4: Design parameters of SKS.

2.4 Scattered-particle spectrometer (SKS)

To meet the challenging requirements mentioned in section 2.1, the superconducting kaon spectrometer (SKS) was designed and constructed. Table 2.4 shows design parameters of SKS. A special characteristic feature is compatibility of a better momentum resolution of 0.1% (FWHM) with a large angular acceptance of 100 msr in the momentum range of around 1 GeV/c. Simultaneously, it keeps the flight path as short as 5 m, and has a powerful kaon identification ability.

Figures 2.11 and 2.12 show schematic views of SKS. The spectrometer comprises a sector-shape superconducting dipole magnet with five sets of drift chambers (SDC1-2-3-4X-4Y) for momentum measurement and three kinds of trigger counters for particle identification: a scintillation counter wall (TOF), two silica aerogel Čerenkov counters (AC1 and AC2), and a Lucite Čerenkov counter wall (LC).

To realize these specifications simultaneously, we adopted the configuration of a single sector-shape dipole magnet with a large aperture. Unlike a conventional high-resolution spectrometer used in nuclear physics, there are no precise focus planes. For the momentum resolution requirement, the magnet is so large and powerful that the bending angle is as large as 100°. The sector shape gives SKS an approximate focusing property, which makes the large angular acceptance possible with a large aperture. This property minimizes multiple-scattering effect on the momentum resolution.

Table 2.5 shows design parameters of the superconducting magnet [38, 39]. The maximum excitation is called the 3.0 T mode (500 A), where the central trajectory corresponds to 0.96 GeV/c. Under the (π^+, K^+) condition, the magnet was operated in the 2.2 T mode (272 A), where the central trajectory corresponded to 0.72 GeV/c. The magnetic field was monitored with an NMR probe during the experiment to

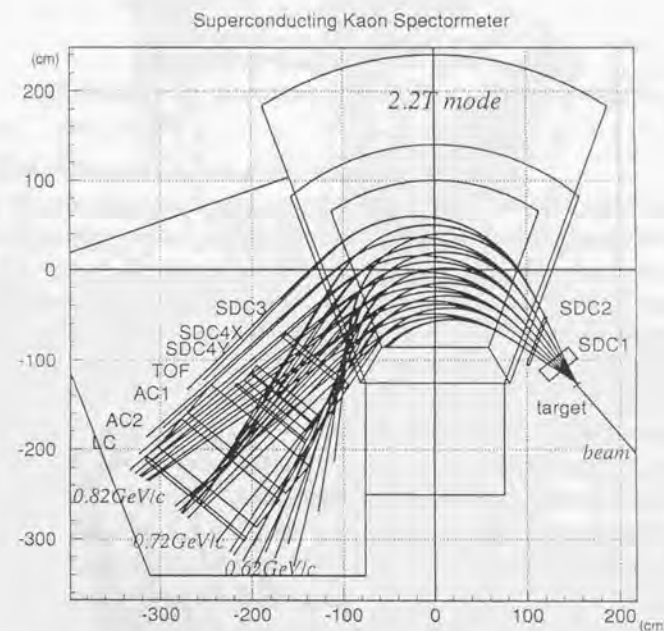


Figure 2.11: Schematic top view of SKS.

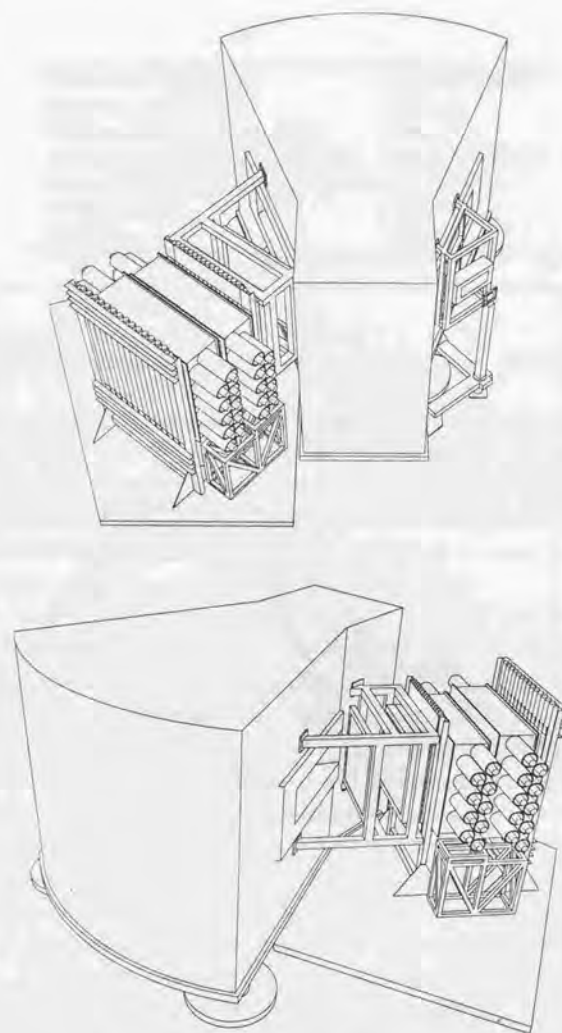


Figure 2.12: Bird's-eye views of SKS.

Type	Sector-shape dipole
Maximum magnetic field	3.0 T
Maximum current	500 A
Field stability	$\pm 0.05\%$
Aperture	$1.5^W \times 0.5^H \text{ m}^2$
Stored energy	11.8 MJ
Ampere turn	2.1 MA turn
Weight	290 t
Heat load	4.5 W (4K)

Table 2.5: Design parameters of the SKS superconducting magnet.

correct its fluctuation in the off-line analysis.

The momentum is determined by reconstructing a particle track with the Runge-Kutta tracking method particle by particle using a measured magnetic field map. In this method, the momentum resolution is limited by the following three factors: multiple scattering, the drift-chamber resolution, and the precision of the magnetic field map. In order to reduce the multiple scattering, SDC2 and SDC3 were made as thin as possible in substance. Furthermore, He bags were installed instead of air between SDC1 and SDC4X. The higher momentum range also made the multiple-scattering effect smaller. Then, this factor is kept small compared to the other two factors. The drift-chamber resolution is also not a critical factor owing to the large bending angle. Consequently, the precision of the magnetic field map is the most important factor limiting the momentum resolution, as shown in appendix B. Prior to the data acquisition, the magnetic field was measured using high-precision Hall probes, as described in appendix A.

Table 2.2 shows specifications of the drift chambers. Since SDC1 and SDC2 are exposed to the beam, the structure of SDC1-2 is the same as that of BDC1-2-3-4, which were designed to be used under a high counting rate.

The sizes of SDC3-4X-4Y are larger in order to match the large angular and momentum acceptances. The SDC4X-4Y have six sense wires in a cell, as shown in Fig.2.13. Their positions are staggered alternatively by $200 \mu\text{m}$ in order to solve the left-right ambiguity. Figure 2.14 shows a distribution of $(x_{\#3} + x_{\#5})/2 - x_{\#4}$ in SDC4X, where $x_{\#3}$, $x_{\#4}$ and $x_{\#5}$ are for the 3rd, 4th and 5th sense wires in a cell. The two peaks correspond to the left and right-hand sides of the sense wires. The width of a peak represents the intrinsic position resolution (typically $\sigma=250$

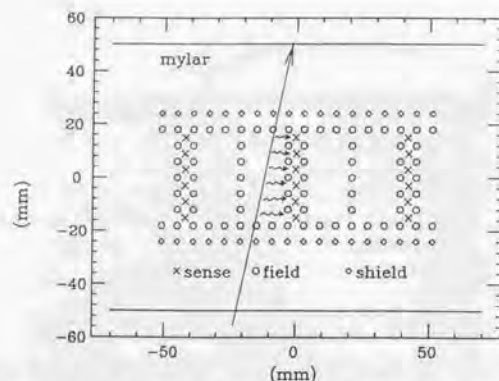


Figure 2.13: Wire configuration of SDC4X-4Y. The sense wires are staggered by $200\mu\text{m}$ to left-hand or right-hand sides alternatively.

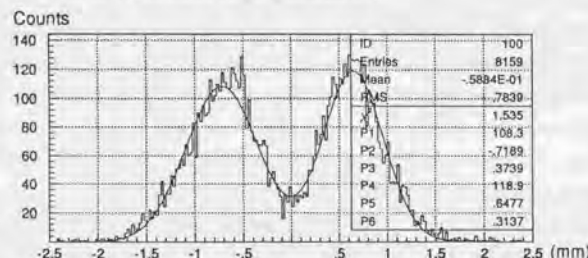


Figure 2.14: Distribution of $(x_{\#3} + x_{\#5})/2 - x_{\#4}$ of SDC4X measured for a $1.06\text{ GeV}/c$ π^+ beam; $x_{\#3}$, $x_{\#4}$ and $x_{\#5}$ are the 3rd, 4th and 5th sense wires of the six in a cell.

μm). The sense and the other wires are made of gold-plated tungsten ($\phi 20\mu\text{m}$) and gold-plated aluminum ($\phi 80\mu\text{m}$), respectively. The gas mixture for SDC3-4X-4Y is Ar (50%) + C_2H_6 (50%) at STP. Typical plateau curves and operation high voltage are shown in Fig.2.15. The two outermost sense wires in a cell were not used in the analysis, since they were noisier because of their incomplete field shape. The readout system was the same as that for BDC1-2-3-4.

Table 2.3 shows specifications of the trigger counters. In the trigger, a combination of three kinds of counters discriminate π , K and p ; TOF is sensitive to charged particles; AC1-2 are sensitive only to π ; LC is insensitive to p . On the other hand, in the off-line analysis, the time-of-flight measurement between TOF and BH1 offers the finest event selection.² Furthermore, the ADC data were used for particle

²Typical time-of-flight values between TOF and the target are 12, 15 and 20 ns for $0.72\text{ GeV}/c$

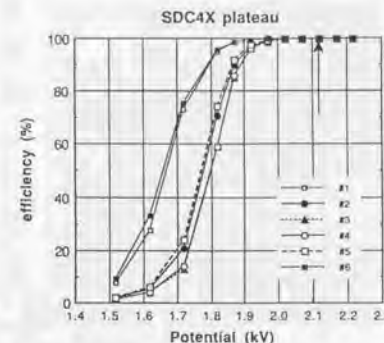


Figure 2.15: Typical plateau curves and operation high voltage of SDC4X; the six sense wires in a cell are denoted by #1~#6.

identification, as described in section 3.5.

Figure 2.16 shows a schematic view of the TOF counter, a scintillation counter wall comprising fifteen independent vertical segments. Fast photomultipliers are attached to both ends of a segment. Figure 2.17 shows a time-of-flight spectrum between BH1 and TOF measured for a $0.72\text{ GeV}/c$ π^+ beam with a correction of the flight path in SKS. A typical time resolution is 200 psec in rms, including that of the two counters and the time jitter of the circuit modules. The timing offset parameters were determined cycle by cycle in the off-line analysis using π^+ beam data; they were found to be stable in each experimental cycle. The photomultiplier gains were stable during the experiment.

Figure 2.18 shows a schematic view of the AC1 counter. The structure of AC2 is essentially the same as that of AC1, except for the sizes. These are threshold-type Čerenkov counters and veto pions with a threshold of $0.4\text{ GeV}/c$. In general, for π/K separation in the $1\text{-GeV}/c$ momentum range, the refractive index must be just between those of gas and liquid, as shown in Fig. 2.20. Silica aerogel is an irreplaceable solid material as a Čerenkov radiator filling this refractive index range. Although liquid helium and liquid hydrogen have appropriate refractive indexes, they are hard to handle.

To realize uniform efficiency without any dead spaces over a large sensitive area of $1.4\text{ m} \times 1.4\text{ m}$, we adopted a two-layer counter system in which each one was of the large one-box type. When covering a large sensitive area, a counter is usually segmented into several smaller ones. However, such a segmented-type counter in π , K and p , respectively.

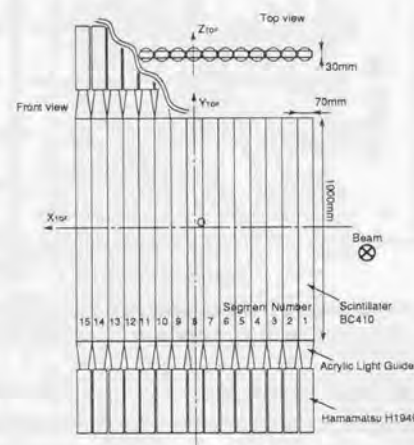


Figure 2.16: Schematic view of the TOF counter.

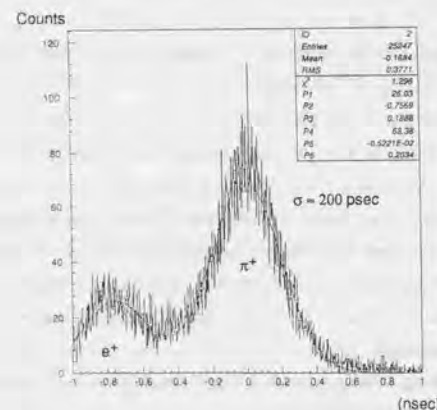


Figure 2.17: Time-of-flight spectrum between TOF and BH1 for a 0.72 GeV/c beam corrected with a flight path and momentum obtained by SKS tracking.

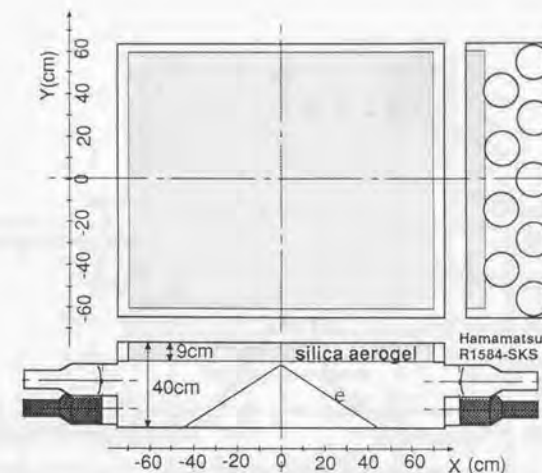


Figure 2.18: Schematic view of AC1.

evitably has dead spaces around the boundary walls. Furthermore, in order to make the spectrometer short, each counter was made as thin as 40 cm. This type of large, but thin, counter box is very unique compared to previously constructed counters. In this case, optimization of the reflector is very important. Details concerning the design process are described in the reference paper [40], where the reflector was optimized in shape and material by a beam test with a proto-type counter.

Silica aerogel blocks were manufactured by *Airglass*.³ The refractive index was set to be 1.06 so as to fit the momentum region. The inner surfaces of the counter boxes were covered with aluminized mylar sheets. The relative gains of the PMTs were adjusted by referring to the one-photoelectron peak in the ADC spectra (Fig.2.19). Figure 2.21 shows the incident-position dependence of the mean photoelectron number for AC1 measured with a 0.72 GeV/c π^+ beam, where a mean photoelectron number of six corresponds to about a 99% efficiency. In order to avoid deterioration of the transparency of the silica aerogel due to moisture, nitrogen gas was flowed in the counter boxes. No degradation was detected by the end of the experiment.

Figure 2.22 shows a schematic view of the LC counter. It was a threshold-type Čerenkov counter comprising fourteen independent vertical segments. Protons were discriminated from pions and kaons using this counter. The threshold momentum for protons is about 0.85 GeV/c. In order to reduce the position dependence of

³Airglass AB, Box 150, S-245 00 Staffanstorps, Sweden.

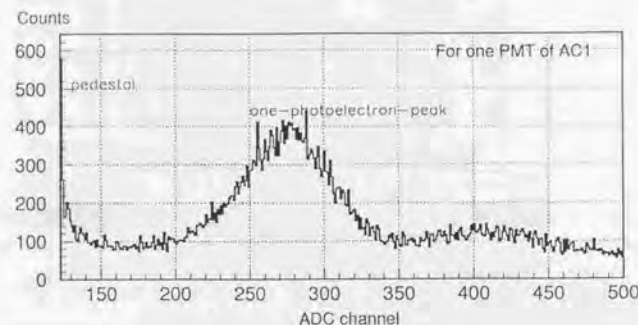


Figure 2.19: ADC spectrum for one PMT of AC1.

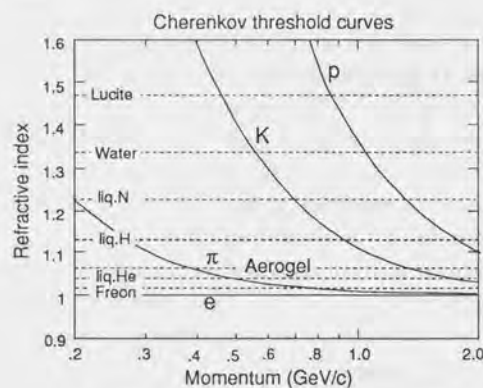


Figure 2.20: Threshold refractive index for Čerenkov radiation as a function of the momentum.

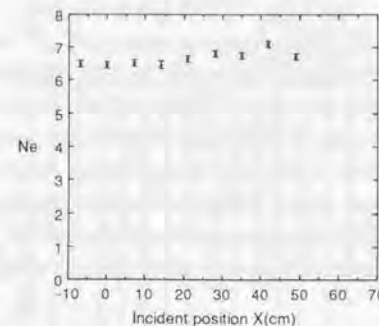


Figure 2.21: Position dependence of the mean photoelectron number for AC1 measured for a 0.72 GeV/c π^+ beam.

the pulse height, the lucite contained 10 ppm of a wavelength shifter (bis-MSB), by which directional Čerenkov photons were diffused. Because the wavelength shifter scintillates, LC is slightly sensitive to protons: typically 10% at 0.7 GeV/c. The photomultiplier gains were stable during the experiment.

2.5 Trigger system

Owing to a higher beam rate of a few million per second, much more background particles were produced through various pion-nucleus reactions, such as $(\pi, \pi'X)$ and (π, pX) , whose cross sections are typically three-orders of magnitude larger than that for the (π^+, K^+) reaction. Therefore, a powerful trigger system was of vital importance for the experiment. In the present system, the (π^+, K^+) trigger comprised three kinds of trigger counters in the beam spectrometer (BH1, BH2 and GC), and three kinds of trigger counters in SKS (TOF, AC1-2 and LC), as mentioned in the previous two sections.

Figure 2.23 shows a trigger diagram. The BEAM trigger is defined by $BH1 \times BH2 \times GC$. Mean timer modules were used to remove the incident-position dependence of the trigger timing for BH1 and BH2. The proton contamination in the beam was rejected by a timing coincidence between BH1 and BH2 with a coincidence width of about 5 nsec. The time difference between pions and protons was about 10 nsec at 1.06 GeV/c.

The (π^+, K^+) trigger is defined by $BEAM \times TOF \times AC1 \times AC2 \times LC$. Mean timer modules were used to remove the incident-position dependence of the trigger

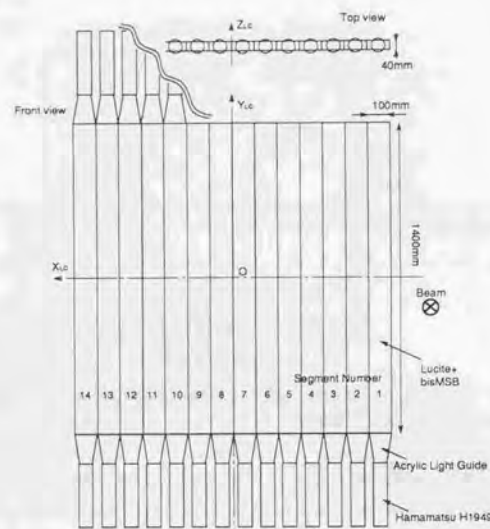


Figure 2.22: Schematic view of LC.

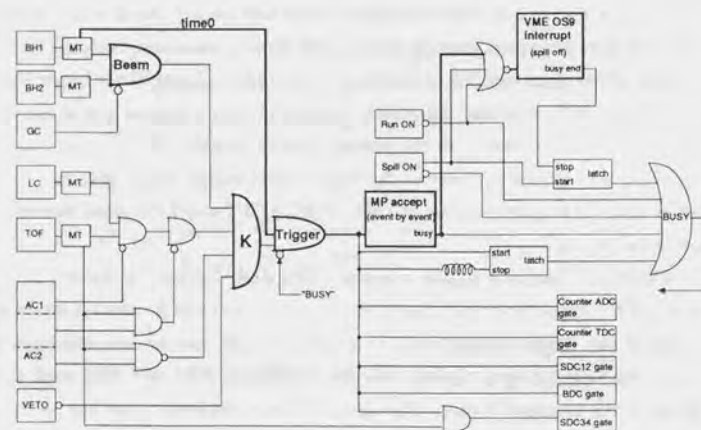


Figure 2.23: Trigger diagram; "MT" represents mean timer modules. No veto counters were used in the present experiment.

timing for TOF and LC. The trigger rate was typically 400 counts/spill for a pion beam rate of 3.0 M/spill. Most of these events came from background pions and protons from the target and other materials, such as the SDC4X·Y support pillars.

The trigger timing was determined by BH1. In order to avoid time jitter by several circuits modules, the BH1 signal was taken a coincidence again after the (π^+, K^+) logic was constructed, as shown in the trigger diagram. It determines the gate timing of the TDC and ADC modules, except for SDC3·4X·4Y, for which the TOF timing determines the gate timing to avoid flight-time difference in SKS.

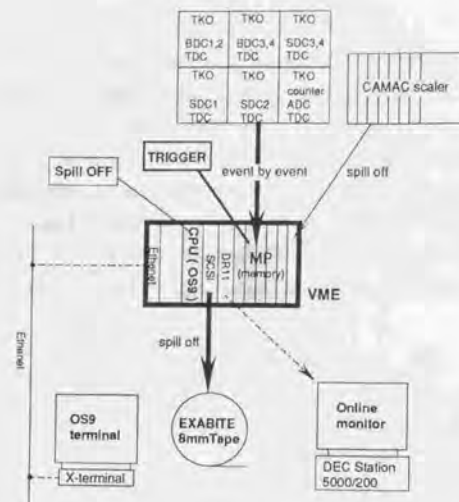


Figure 2.24: Diagram of the data-acquisition system.

2.6 Data-acquisition system

Figure 2.24 shows a diagram of the data-acquisition system. The system operates synchronized to the accelerator cycle, where a beam is extracted for 1.4 sec in each 4.0 sec. First, event by event, raw data are fed into the TDC and ADC modules of the KEK-TKO standard [41]. Their digital data are then stored in VME memory modules (MP). During a spill-off period of 2.6 sec, those accumulated data are written on an 8-mm-tape device after being processed by a CPU module (with 68020 on OS9) in VME. A CAMAC crate is also connected to the system to handle scaler data spill by spill. A typical data size was about 150 long-words per event. A typical dead time was 10% for a trigger rate of 400 counts/spill. For on-line monitoring, the raw data were transferred to a workstation through a DR11 module. The data-acquisition task in VME was independent of the data-monitoring tasks in the workstation.

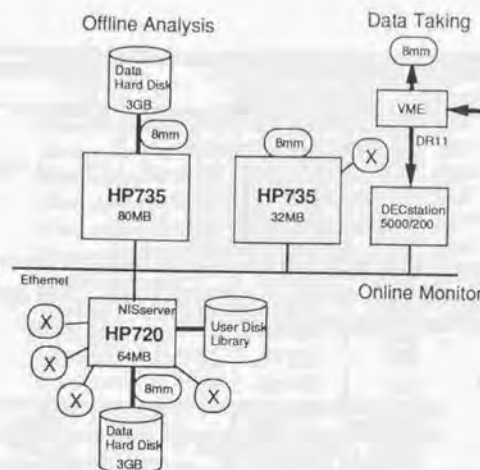


Figure 2.25: Diagram of the off-line data-analysis system; "X" represents an X-terminal.

2.7 Off-line analysis system

Figure 2.25 shows a schematic of the off-line data-analysis system. We adopted latest workstations with faster RISC-CPU's instead of a main-frame computer which have been used for many years in KEK-PS experiments. A typical analysis time for a good (π^+ , K^+) event was a few hundreds msec on HP735.

2.8 Targets

Table 2.6 shows specifications of the targets used in the present experiment.

A target should have simple neutron shell structure, since a neutron is converted into a Λ hyperon in the (π^+ , K^+) reaction. In this respect, ^{208}Pb , ^{139}La , ^{89}Y and ^{28}Si were selected because they have a neutron-closed shell structure. Since fine peak structure belonging to core-excited states are expected to be resolved with the medium energy resolution (see section 5.2), ^{12}C and ^{10}B were chosen. Another important merit of using ^{12}C is that the ^{12}C spectrum has two well-separated narrow peaks which can be used for experimental system calibration.

The thickness was chosen so as to make the energy-loss straggling sufficiently small, in order to keep the energy resolution at about 2 MeV. The target energy-

Targets Targets	Thickness (g/cm ²)	Purity (%)	Contamination (%)
¹² C	0.887±0.026	98.9 (natural)	¹³ C :1.1
¹⁰ B	2.141±0.043	99 (enriched)	
²⁸ Si	2.371±0.047	92.2 (natural)	²⁹ Si :4.7, ³⁰ Si :3.1
⁸⁹ Y	3.126±0.037	100.0 (natural)	
¹³⁹ La	3.662±0.037	99.9 (natural)	
²⁰⁸ Pb	3.407±0.170	99 (enriched)	

Table 2.6: Specifications of the experimental targets. The quoted errors of the thickness come from target size measurements.

Cycles	Date	Targets	N_{BEAM}
92-11	1993/2/07~2/17	¹² C	30.12G
		²⁸ Si	147.86G
		⁸⁹ Y	254.53G
92-12	1993/2/26~3/09	¹² C	58.48G
		¹³⁹ La	513.20G
93-02	1993/5/16~5/20	¹² C	76.81G
		²⁰⁸ Pb	113.73G
93-03	1993/6/04~6/17	¹² C	83.28G
		²⁰⁸ Pb	571.25G
93-04	1993/6/25~7/07	¹² C	70.93G
		¹⁰ B	144.99G
		²⁰⁸ Pb	168.70G

Table 2.7: Data summary; N_{BEAM} is the integrated BEAM count.

loss straggling is described in section 3.7.

2.9 Data summary

Table 2.7 is a data summary. The data were taken in five separated experimental cycles from February to July in 1993: 92-11, 92-12, 93-02, 93-03 and 93-04 cycles. In each experimental cycle, $^{12}\text{C}(\pi^+, K^+)$ data were taken for the total system calibration. One run was defined to be for about three hours.

Parameters	Values (MeV)	References
Mass excess of ⁹ B	12.4161	[42]
Mass excess of ¹⁰ B	12.0517	[42]
Mass excess of ¹¹ C	10.6500	[42]
Mass excess of ¹² C	0.0000	[42]
Mass excess of ²⁷ Si	-12.3853	[42]
Mass excess of ²⁸ Si	-21.4912	[42]
Mass excess of ⁸⁸ Y	-84.298	[42]
Mass excess of ⁸⁹ Y	-87.6953	[42]
Mass excess of ¹³⁸ La	-86.524	[42]
Mass excess of ¹³⁹ La	-87.231	[42]
Mass excess of ²⁰⁷ Pb	-22.463	[42]
Mass excess of ²⁰⁸ Pb	-21.759	[42]
Mass of π^+	139.5679	[43]
Mass of K^+	493.646	[43]
Mass of n	939.56563	[43]
Mass of p	938.27231	[43]
Mass of Λ	1115.63	[43]
Atomic mass unit	931.494	[43]

Table 2.8: Physics constants and parameters used in the analysis.

2.10 Physics constants and parameters

Table 2.8 shows physics constants and parameters used in the analysis.

Chapter 3

Data analysis

3.1 Outline

The goals of the data analysis in the present experiment were to obtain hypernuclear mass spectra and to specify their quality quantitatively. In this chapter, those procedures are described. The hypernuclear mass (M_{HY}) is calculated by a kinematical relation of the (π^+, K^+) reaction,

$$M_{HY} = \sqrt{(E_\pi + M_A - E_K)^2 - (p_\pi^2 + p_K^2 - 2p_\pi p_K \cos \theta)}, \quad (3.1)$$

where M_A is the target nuclear mass, θ is the scattering angle, and p_π , p_K , E_π and E_K are the momentum and energy of π^+ and K^+ , respectively. Thus, there are three kinematical variables to be measured experimentally: p_π , p_K and θ . Sections 3.2, 3.3 and 3.4 describe how to determine these three kinematical variables, respectively. In the off-line analysis, particle identification was essential for obtaining background-free spectra, because only a very small portion of the data taken with the (π^+, K^+) trigger belonged to the (π^+, K^+) events. Section 3.5 describes the particle identification procedures. The quality of the spectra could be characterized in terms of the precision of the vertical (cross section) scale, the precision of the horizontal (energy) scale, and the background level. These three factors are discussed in sections 3.6, 3.7 and 3.8, respectively. For convenience, a flow chart of the off-line program is shown in Fig. 3.1.

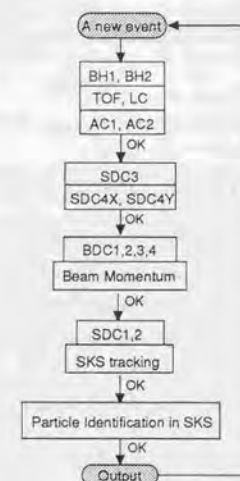


Figure 3.1: Flow chart of the off-line analysis program. Faster routines are placed before time-consuming ones.

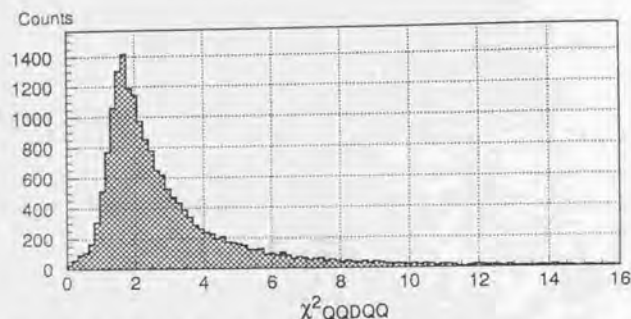


Figure 3.2: Typical distribution of χ^2_{QQDQQ} for a 1.06 GeV/c π^+ beam.

3.2 Momentum of a beam particle

The beam momentum was calculated from beam drift-chamber data as follows. At first, straight tracks were defined locally at the entrance of QQDQQ by BDC1-2 and at the exit by BDC3-4 by a least-square method. For a multihit event, all possible combinations were examined. The consistency with the BH1, BH2, Q7 and Q10 sizes was checked. Next, for each track at the exit, the best track at the entrance was selected by comparing the chi-square defined by

$$\chi^2_{QQDQQ} = \frac{1}{4-1} \left(\frac{\vec{x}_{out} - \mathcal{M}\vec{x}_{in}}{\vec{w}_{out}} \right)^2, \quad (3.2)$$

where the four components of a vector are the horizontal and vertical coordinates and tangents; the subscripts (*in* and *out*) stand for the entrance and exit of QQDQQ; \vec{w}_{out} are appropriate weights determined by the drift-chamber resolution. The operator \mathcal{M} represents a 3rd-order transfer matrix from \vec{x}_{in} to \vec{x}_{out} , depending on the momentum. This matrix was calculated by *Orbit* [44]. The momentum is determined so as to minimize χ^2_{QQDQQ} . A typical distribution of χ^2_{QQDQQ} is shown in Fig.3.2. Candidates whose χ^2_{QQDQQ} s were less than 16 were accepted.

In order to achieve the required momentum resolution, the momentum calculated with the *Orbit* matrix was corrected. The correction terms were calibrated by SKS by leading a 1.06 GeV/c π^+ beam through the two spectrometers. Details concerning the calibration procedure are described in appendix C. By this correction,

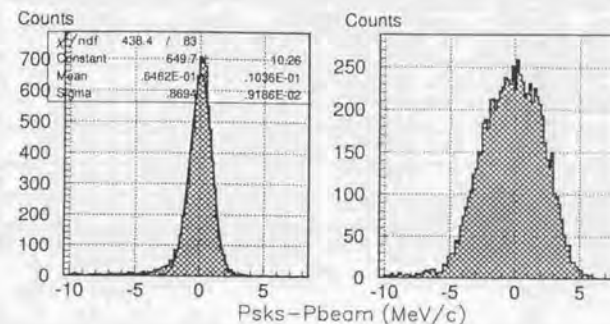


Figure 3.3: Total momentum resolution of the two spectrometers, QQDQQ and SKS, for a 1.06 GeV/c π^+ beam seen as the momentum difference. The left-hand and right-hand figures are with and without the momentum correction described in the text, respectively.

the momentum resolution was improved from 4.9 to 2.0 MeV/c (FWHM)¹ for a 1.06 GeV/c π^+ beam, as shown in Fig.3.3.

3.3 Momentum of a scattered particle

The momentum of a scattered particle was calculated from drift-chamber data as follows. At first, straight tracks were defined by SDC1 and SDC2 in order to find good combinations of hit positions in several planes. For a multihit event, all possible combinations were examined in order to construct straight tracks. In SDC4X and SDC4Y, at least three of the four middle sense wires in a cell were used to construct one candidate.

Next, the momentum was determined with those hit positions by reconstructing a track in the spectrometer by the Runge-Kutta tracking method using a measured magnetic field map. In this method, the chi-square defined below was minimized by iteration to optimize five parameters: the momentum, two independent positions,

¹These values include the momentum resolution of the two spectrometers. The results are consistent with a Monte-Carlo calculations (appendix B).

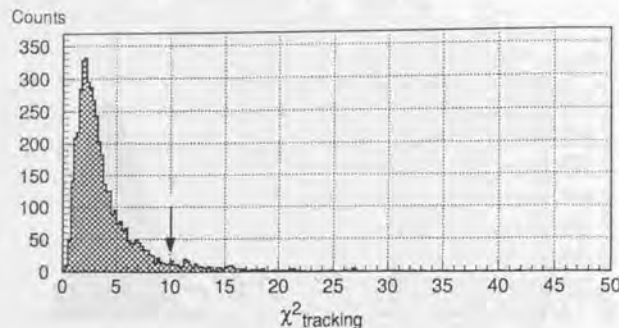


Figure 3.4: Typical distribution of $\chi^2_{tracking}$ for $^{12}\text{C}(\pi^+, K^+)$ data. The event-selection criterion is indicated as the arrow.

and two independent angles at the target. The chi-square ($\chi^2_{tracking}$) is defined by

$$\chi^2_{tracking} = \frac{1}{n-5} \sum_{i=1}^n \left(\frac{x_{tracking,i} - x_{data,i}}{w_i} \right)^2, \quad (3.3)$$

where n is the number of drift-chamber planes having hits; $x_{tracking,i}$ and $x_{data,i}$ are the hit positions on the i -th hit plane in tracking and data, respectively; w_i are proper weights determined by the drift-chamber resolution. The SDC3 data were not used in the tracking, but were used only for background rejection, as described in section 3.6. The convergence criterion in the iteration is $(\chi^2_{i+1} - \chi^2_i)/\chi^2_i < 10^{-3}$, where i is the number of iterations and χ^2_i is the tracking chi-square for the i -th iteration. The divergence criterion was $i > 45$ or $\chi^2_i > 10^{10}$. In the program, a linear approximation [45] and a simultaneous calculation method of derivatives [46] were adopted in order to save computation time. Figure 3.4 shows a typical distribution of $\chi^2_{tracking}$ for $^{12}\text{C}(\pi^+, K^+)$ data.

The consistency with TOP and LC segment positions was examined. For each candidate of SDC4X-4Y, the best track of SDC1-2 was selected by comparing $\chi^2_{tracking}$. Then, for each track of SDC1-2, the best track of BDC3-4 was selected by comparing the horizontal and vertical positions at the target. From these combinations, the minimum $\chi^2_{tracking}$ event was selected as the best candidate of the tracking.

The momentum determination by tracking suffers systematic errors of the magnetic field map and geometry parameters of the drift chambers. Therefore, the momentum had to be corrected, as described in section 3.7.

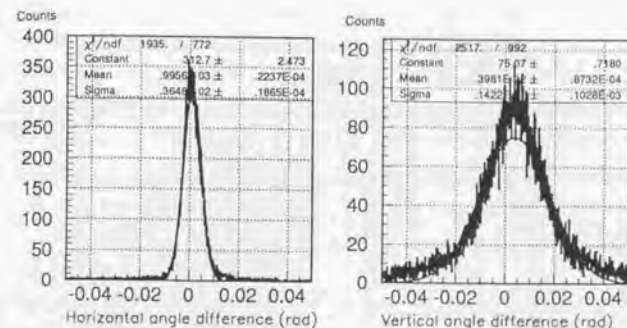


Figure 3.5: Typical distributions of the horizontal (left-hand) and vertical (right-hand) scattering angles measured by BDC3-4 and SDC1-2 for a 1.06 GeV/c π^+ beam without a target.

3.4 Scattering angle

The scattering angle was determined by two local straight tracks respectively defined in BDC3-4 and SDC1-2. Figure 3.5 shows typical horizontal and vertical scattering-angle resolutions; they are 0.004 and 0.014 rad in rms, respectively. Because of the special wire configuration of the drift chambers, the vertical resolution was worse than the horizontal one.

The scattering-angle resolution was important for rejecting background events associated with beam particles scattered into very forward angles. Figure 3.6 shows a scatter plot between the horizontal scattering angle and the Λ binding energy for $^{12}\text{C}(\pi^+, K^+)$ data. Those background events can be identified in the overbound region. Events whose horizontal scattering angles were less than 0.01 rad (0.035 rad) were rejected for ^{12}C , ^{10}B and ^{28}Si (^{89}Y , ^{139}La and ^{208}Pb).

3.5 Particle identification in SKS

The scattered particle mass ($M_{scattered}$) was calculated using

$$M_{scattered} = \frac{p}{\beta} \sqrt{1 - \beta^2}, \quad (3.4)$$

where β is the velocity determined by the time-of-flight measurement between BH1 and TOF assuming that the beam particle is a pion; p is the momentum determined

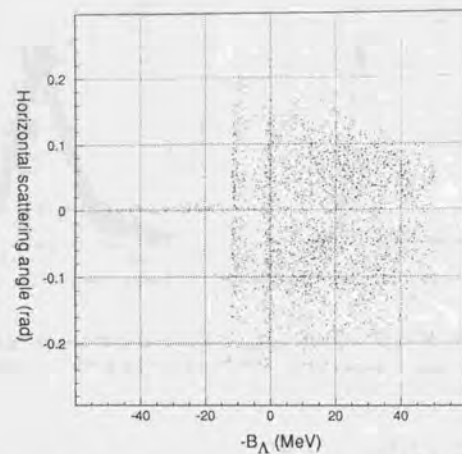


Figure 3.6: Scatter plot between the horizontal scattering angle and the Λ binding energy for $^{12}\text{C}(\pi^+, K^+)$ data.

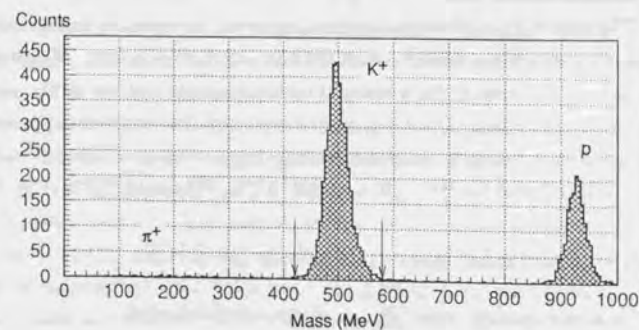


Figure 3.7: Scattered particle mass spectrum for $^{12}\text{C}(\pi^+, K^+)$ data. The arrows indicate the event-selection criteria.

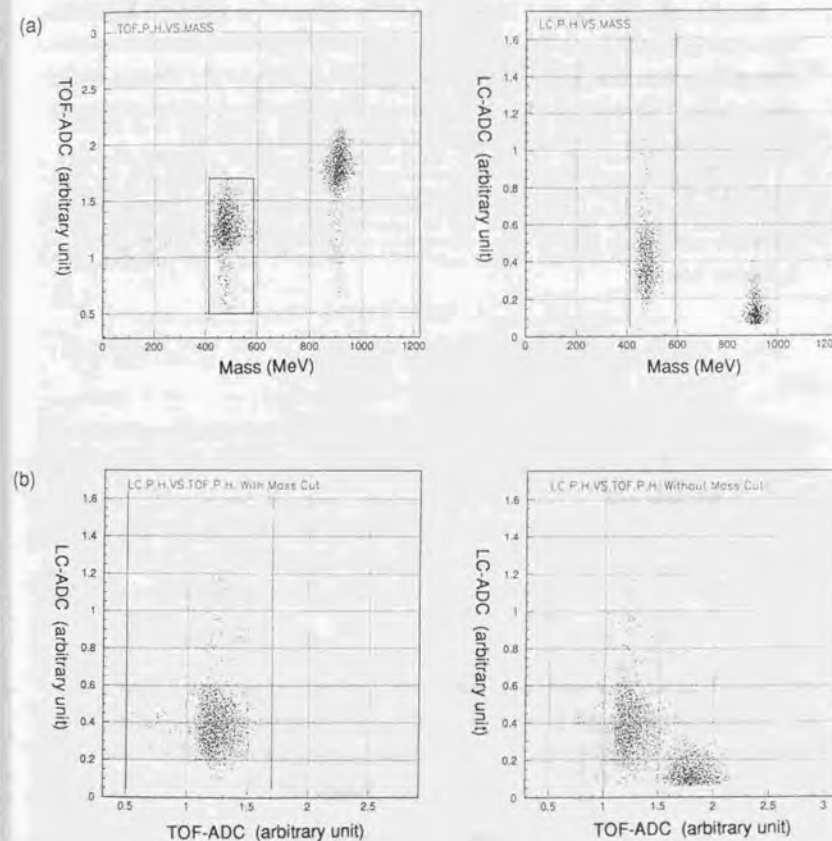


Figure 3.8: (a) Scatter plots between the scattered particle mass and the TOF-ADC (left-hand) or LC-ADC (right-hand) for $^{12}\text{C}(\pi^+, K^+)$ data. (b) Scatter plots between TOF-ADC and LC-ADC for $^{12}\text{C}(\pi^+, K^+)$ data with (left-hand) or without (right-hand) the scattered particle mass cuts.

in the SKS tracking. Figure 3.7 shows a typical mass spectrum for $^{12}\text{C}(\pi^+, K^+)$ data and event-selection criteria. It is remarkable that π^+ events were well suppressed because of the excellent performance of AC1 and AC2.

Background particles other than K^+ could be separated in various scatter plots related to TOF-ADC or LC-ADC. Figure 3.8-(a) shows a scatter plot between the scattered particle mass and TOF-ADC or LC-ADC. Figure 3.8-(b) shows a scatter plot between TOF-ADC and LC-ADC with or without scattered-particle mass cuts. The event-selection criteria are indicated by solid lines in the figures.

The efficiencies associated with these cuts are estimated in section 3.6. In addition to these cuts, for a background-level reduction, appropriate cuts were applied to the beam profiles, the SKS tracking chi-square, and the target z-vertex, as described in section 3.6.

3.6 Cross section

The cross section was calculated from the experimental yields divided by the experimental efficiency,

$$\left(\frac{d\sigma}{d\Omega}\right) = \frac{A}{(\rho x)N_A} \cdot \frac{1}{N_{BEAM}} \cdot \sum_{i=1}^{N_K} \frac{1}{\varepsilon_{total}d\Omega}, \quad (3.5)$$

where A is the target mass number, (ρx) the target thickness in g/cm^2 , N_A Avogadro's number, N_{BEAM} the beam count defined by $\text{BH1} \times \text{BH2} \times \overline{\text{GC}}$, N_K the number of K^+ events, $d\Omega$ the angular acceptance of SKS, and ε_{total} the experimental efficiency. Consequently, the precision of the cross section was determined by that of (ρx) , $d\Omega$ and ε_{total} . We assume that ε_{total} can be written as

$$\begin{aligned} \varepsilon_{total} = & f_{BEAM} \cdot \varepsilon_{BDC} \\ & \cdot \varepsilon_{SDC1,2} \cdot \varepsilon_{SDC3} \cdot \varepsilon_{SDC4X,Y} \cdot \varepsilon_{TOF} \cdot \varepsilon_{LC} \\ & \cdot f_{AC} \cdot \varepsilon_{es} \cdot \varepsilon_{daq} \cdot f_{decay} \cdot f_{absorption}, \end{aligned} \quad (3.6)$$

where the symbols are defined in Table 3.1. In this section, we discuss how these efficiency factors were estimated using calibration data or by a Monte-Carlo simulation. The target thickness is described in section 2.8. The acceptance of SKS, estimated by a Monte-Carlo calculation, is given in appendix D.

3.6.1 Efficiency

N_{BEAM} correction factor

The N_{BEAM} correction factor (f_{BEAM}) represents the rate of π^+ out of N_{BEAM} . The e^+ contamination was vetoed by GC with an efficiency of better than 99.9%. The p contamination was rejected by the DC separator and timing coincidence between BH1 and BH2. Therefore, f_{BEAM} can be written as

$$f_{BEAM} = (1 - r_\mu) \cdot f_{BH1,2} \cdot f_{profile}, \quad (3.7)$$

where r_μ is the μ^+ contamination rate in the beam, $f_{BH1,2}$ is a correction for accidental coincidence of BH1 and BH2, and $f_{profile}$ stands for the beam-profile cuts described below.

The μ^+ contamination rate (r_μ) was estimated to be 5.9~6.5% at 1.00~1.10 GeV/c by using *Decay Turtle* [47]. Under a different beam-transport condition, the μ^+ contamination was measured directly with an additional high-pressure Freon-gas

Factors	Names	Typical values (%)
f_{BEAM}	N_{BEAM} correction factor	85.5 ± 4.1
ϵ_{BDC}	BDC efficiency	70 ± 2
ϵ_{SDC1-2}	SDC1-2 efficiency	80 ± 2
ϵ_{SDC3}	SDC3 efficiency	98.0 ± 1.5
$\epsilon_{SDC4X-Y}$	SDC4X-Y efficiency	94.0 ± 1.5
ϵ_{TOF}	TOF efficiency	99.8 ± 0.2
ϵ_{LC}	LC efficiency	99.0 ± 1.0
f_{AC}	AC1-2 accidental veto factor	93.0 ± 1.0
ϵ_{daq}	Data-acquisition efficiency	92.0 ± 0.1
f_{decay}	K^+ decay factor	40 ± 2
$f_{absorption}$	K^+ absorption factor	99.8 ± 0.2
ϵ_{es}	Event-selection efficiency	74 ± 3
	The total relative error	± 10

Table 3.1: List of the experimental efficiency factors and estimated percentages.

Čerenkov counter. In this case, a *Decay Turtle* calculation agreed with the measured result within $\pm 1.5\%$. Therefore, we assume that the error is $\pm 2.0\%$, including the momentum dependence: $r_\mu = 6.2 \pm 2.0\%$.

The accidental coincidence factor (f_{BH1-2}) was estimated run by run with BEAM trigger data mixed in the (π^+ , K^+) data as $f_{BH1-2} = N_{BH1-2}/N_{BEAM}$. The numerator (N_{BH1-2}) is the number of events for which the time-of-flight values between BH1 and BH2 are proper for π^+ . This estimation takes account of TDC pile-up effects implicitly. A typical result is $f_{BH1-2} = 97.0 \pm 0.5\%$, where the error is the statistical fluctuation of the estimation.

The beam-profile cut factor ($f_{profile}$) stands for cuts rejecting the tails of beam profiles. For example, Fig.3.9 shows a distribution of x at BDC2 for a 1.06 GeV/c π^+ beam and cut points. Similar cuts were applied to y , x' , y' at BDC2 and x , x' , y , y' at the target. The cut efficiency was estimated by Gaussian fitting to be $f_{profile} = 94.0\% \pm 2.0\%$ in total, where the error is the statistical fluctuation of the estimation.

In total, a typical result is $f_{BEAM} = 85.5 \pm 4.1\%$.

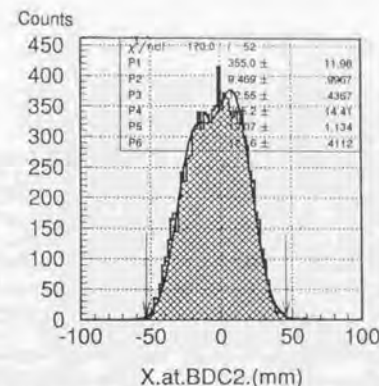


Figure 3.9: Distribution of x at BDC2 for a 1.06 GeV/c π^+ beam. The arrows indicate the cut points. The solid line is a Gaussian fitting curve.

BDC and SDC1-2 efficiency

The BDC efficiency (ϵ_{BDC}) represents the detector efficiency and the analysis efficiency. It was directly estimated run by run with the BEAM trigger data mixed in the (π^+ , K^+) data, where beam particles were defined by BH1 and BH2. Typical results are shown in Fig.3.10 as a function of the BEAM rate. The efficiency decreases with increasing rate because of the intrinsic inefficiency, pile-ups, and algorithm limitation. Note that the actual particle rate at around BDC1-2 was as much as twice the BEAM rate because of background particles from upstream (section 2.3). A typical result is $\epsilon_{BDC} = 70 \pm 2\%$, where the error is the statistical fluctuation of the estimation.

The SDC1-2 efficiency (ϵ_{SDC1-2}) was estimated in the same way. Typical results are shown in Fig.3.10 as a function of the BEAM rate. The rate dependence is small in this case. Since the energy-loss difference between 1 GeV/c π^+ and 0.7 GeV/c K^+ is small (K^+ 's energy-loss is 97% of π^+ 's), we assume the result is the same for K^+ . A typical result is $\epsilon_{SDC1-2} = 80 \pm 2\%$.

SDC3 and SDC4X-Y efficiency

The SDC3 efficiency and the SDC4X-Y efficiency (ϵ_{SDC3} and $\epsilon_{SDC4X-Y}$) represent the detector efficiency and the analysis efficiency. Since SDC4X-Y has the complex wire configuration, the incident-angle dependence had to be considered. The efficiency was estimated with a 0.72 GeV/c π^+ beam, where beam particles were defined by BEAM \times TOF \times LC. The results are plotted versus the incident position, angle

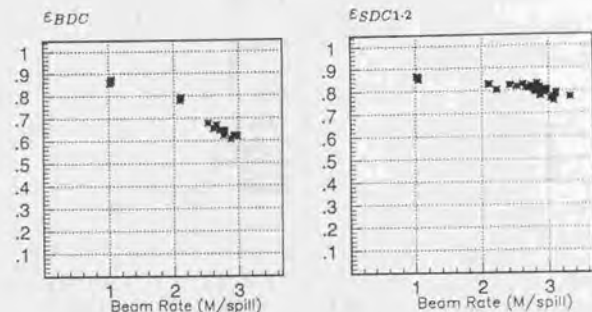


Figure 3.10: Typical BDC (left-hand) and SDC1-2 (right-hand) efficiencies (ϵ_{BDC} and ϵ_{SDC1-2}) as a function of the BEAM rate.

and counting rate in Figs.3.11-(a), (b) and (c), respectively. The position and angle dependence is small, as shown in the figures. The efficiency decreases slightly with increasing rate. Since the counting rate was typically less than 0.1 M/cell/spill under the (π^+ , K^+) condition, this dependence could be ignored. As a result, we obtained $\epsilon_{SDC3} = 98.0 \pm 1.5\%$ and $\epsilon_{SDC4XY} = 94.0 \pm 1.5\%$. The errors include the small dependence on those parameters. Since the energy-loss difference between K^+ and π^+ is small (K^+ 's energy loss is about 87% of π^+ 's at 0.72 GeV/c), we assume the results are the same for K^+ .

TOF and LC efficiency

The TOF efficiency (ϵ_{TOF}) was estimated with 0.72 GeV/c π^+ beam data, where the beam particles were defined by BEAM, SDC3, SDC4X-Y and LC. The result is $\epsilon_{TOF} = 99.8 \pm 0.2\%$, where the error is the statistical fluctuation of the estimation. Incident angles from -0.2 to 0.2 rad were averaged. We assume that the result is the same for K^+ because of the small energy-loss difference between π^+ and K^+ .

The LC efficiency (ϵ_{LC}) was similarly estimated to be $99.8 \pm 0.2\%$, where the beam particles were defined by BEAM, SDC3, SDC4X-Y, AC1-2 and TOF. For LC, however, we could not simply assume that the efficiency was the same for K^+ , since the pulse height for K^+ was typically 40% of that for π^+ . Unfortunately, the efficiency was not measured for K^+ , because a good-quality K^+ beam was not

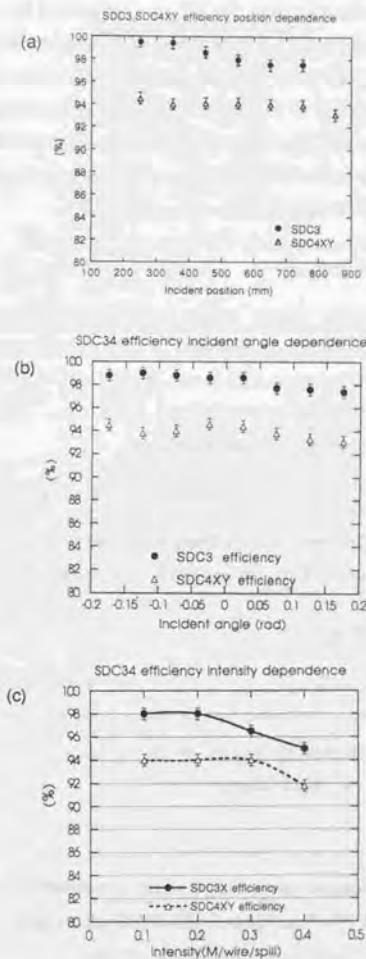


Figure 3.11: SDC3 and SDC4X-Y efficiency as a function of (a) the incident position ($|x', y'| < 0.2$ and rate < 0.1 M/cell/spill), (b) the incident angle. ($|x| < 350$ mm and rate < 0.1 M/cell/spill), and (c) the counting rate ($|x| \simeq 0$ and $|x', y'| < 0.1$).

available. Therefore, the efficiency for K^+ was estimated by a simple Monte-Carlo simulation. In this simulation, a measured pulse-height distribution for K^+ was assumed. The threshold level was set at $2.5 \pm 0.5\sigma$, where the error came from attenuation and dispersion of the pulse height for segment by segment. A realistic segment configuration was also taken into account. The result is $\varepsilon_{LC} = 99.0 \pm 1.0\%$. The small inefficiency comes from dead spaces between segments of 1.5 ± 0.5 mm and the relatively high threshold.

AC accidental veto factor

The accidental veto in the trigger had to be taken into account, because of a high single counting rate of AC1-2. It was due to background particles other than K^+ . The coincidence width between AC1-2 and BEAM \times TOF \times LC was 60 ± 5 ns, where the minimum allowed coincidence width was about 4 ns. Thus, the accidental veto rate, $1 - f_{AC}$, can be written approximately as

$$\frac{R_{AC} \times (60 \pm 5) \times 10^{-9}}{(1.4 \pm 0.1)} = 1 - f_{AC}, \quad (3.8)$$

where R_{AC} is the single count of AC1-2 per spill, and the denominator is the interval of a spill. A typical value of R_{AC} was 1.6 M/spill; we thus obtain $f_{AC} = 93 \pm 1\%$.

Data-acquisition efficiency

The data-acquisition efficiency (ε_{daq}) stands for the dead time of the data-acquisition system. This factor was calculated as the ratio of the number of accepted events to that of triggers, run by run. A typical result is $92.0 \pm 0.1\%$, where the error is the statistical fluctuation of the estimation.

K^+ decay factor

Some of the kaons produced in the target decayed before they reached the detectors. In this subsection, an efficiency factor associated with the K^+ decay (f_{decay}), which was estimated by a Monte-Carlo simulation, is described. Note that the $\beta\gamma c\tau$ of 720 MeV/c K^+ is 5.4 m, comparable to the flight path in SKS. For convenience, the principal decay channels of K^+ are listed in Table 3.2.

In the case in which they decay before SDC4X-Y (TOF), these events may not have been accepted as good K^+ events, or may have been accepted accidentally as background events. In this case, the following criteria were imposed in the simulation. All of the detectors were required to have hits. High β particles were rejected

Channel	Fraction (%)
$\mu^+\nu$	63.5
$\pi^+\pi^0$	21.2
$\pi^+\pi^+\pi^-$	5.6
$\pi^+\pi^0\pi^0$	1.7
$\pi^0\mu^+\nu$	3.2
$\pi^0e^+\nu$	4.8

Table 3.2: Principal K^+ decay channels.

Decay	Criteria	Fraction (%)
No decay		*35.1
Decay before SDC4X-Y		54.0
	All hits	35.4
	Tracking χ^2	1.8
	Deviation at SDC3	1.5
	AC1-2	0.0
Decay after SDC4X-Y		10.9
	AC1-2	9.5
	Deviation at LC	*4.6

Table 3.3: Rejection of K^+ decay events by the criteria described in the text ($p_{SKS}=700\sim 740$ MeV/c, $\theta_{SKS} < 3^\circ$). The asterisks indicate the parameters relevant to the efficiency estimation.

by AC1 and AC2. The tracking chi-square and the tracking SDC3 deviation had to be less than 50 and 1 cm, respectively. These were very loose cuts in the sense that they hardly rejected good events without decay. Then, all of the decay events were rejected, as shown in Table 3.3. In the simulation, events were generated with a uniform momentum distribution ($p_{SKS}=700\sim 740$ MeV/c), a uniform angle distribution ($\theta_{SKS} < 3^\circ$), and a realistic reaction point distribution ($\sigma_{x,y}=6.0, 7.5$ mm), at the target.

In the case where they decayed after SDC4X-Y (TOF), some may have been accepted by charged decay particles. Fortunately, since the momentum reconstruction and the time-of-flight measurement were not affected, these events did not contribute to the background. In this case, the imposed criteria were the rejection by AC1-2 and a consistency check of the LC segment number. Then, 4.6% of the generated events were accepted as good K^+ events, as shown in Table 3.3. In total, we obtain

$$f_{\text{decay}} = 34.9 + 4.6 = 39.5\%.$$

Next, to estimate the momentum and incident-angle dependence of f_{decay} , a simulation was repeated for a set of events covering wider momentum and angle ranges ($p_{\text{SKS}} = 640 \sim 800$ MeV/c, $\theta_{\text{SKS}} < 15^\circ$). The results can be parametrized approximately as

$$f_{\text{decay}} = 34.9 + 0.039(p_{\text{SKS}} - 720) \pm 1.5\% \\ + 3.9 - 0.00044(p_{\text{SKS}} - 727)^2 \pm 0.5\%, \quad (3.9)$$

where p_{SKS} is in MeV/c; the first and second lines correspond to a simple K^+ decay rate and a factor associated with the decay after SDC4X-Y, respectively. The angle dependence was small and averaged into the errors.

K^+ absorption factor

Some of the kaons produced in the target were absorbed by various materials in the spectrometer. This reaction rate ($1 - f_{\text{absorption}}$) can be calculated by

$$1 - f_{\text{absorption}} = \frac{\sigma_{\text{inel}}}{M} N_A (\rho x), \quad (3.10)$$

where σ_{inel} is the inelastic cross section, M the atomic weight, N_A Avogadro's number, and (ρx) the thickness of the material in g/cm². Considering the He bags, the drift-chamber gas, the counters and a target, $N_A(\rho x)$ amounts to $0.52 \sim 0.69\%$ /mb. Fortunately, the K^+N cross section is dominated by the elastic one in the momentum range below 0.8 GeV/c. The inelastic cross section is expected to be less than 0.5 mb around 0.7 GeV/c [48]. Therefore, the absorption rate was less than 0.4%. Thus, this correction factor is negligibly small compared to the other efficiency factors.

Event-selection efficiency

In order to reduce background levels sufficiently, proper cuts were applied to some parameters. These cuts not only rejected background events, but also true (π^+ , K^+) events. In this subsection, the efficiency factors associated with these cuts are calculated by using the 93-02 cycle $^{12}\text{C}(\pi^+, K^+)$ data as an example. The same procedure was repeated for each cycle.

Cuts were applied to χ^2_{tracking} and the deviation at each drift-chamber plane in the SKS tracking. As an example, Fig.3.4 shows a χ^2_{tracking} distribution and a cut

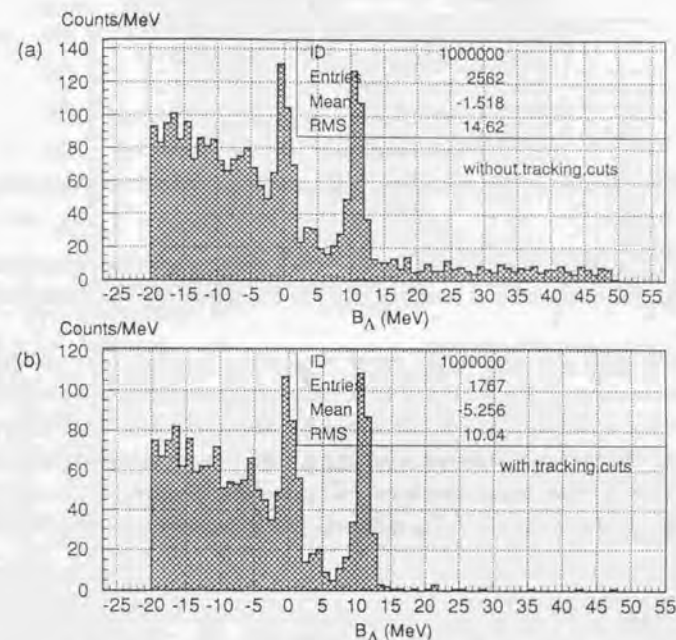


Figure 3.12: Mass spectra for the 93-02 cycle ^{12}C data without (a) and with (b) the SKS tracking chi-square and deviation cuts.

point. Since SDC3 data were not used in the SKS tracking (as mentioned in section 3.3), the SDC3 deviation cut was effective for reducing the background. Figure 3.12 shows mass spectra with and without these cuts, showing how well the background level was reduced. Assuming that the background level was approximately uniform over the energy scale (as discussed in section 3.8), the corresponding cut efficiency was estimated to be $84.0 \pm 2.0\%$ in total from those spectra, where the error is the statistical fluctuation of the estimation.

Cuts were applied to the target z-vertex of the reaction point, as shown in Fig.3.13-(a). This was for selecting good events which had a reaction in the target. Rather tight cuts were required in order to sufficiently reduce the background level. The large tails came from forward events, as shown in Fig.3.13-(b), because the

Cuts	Typical values (%)
Tracking χ^2 & deviation	84.0 ± 2.0
Target z-vertex	90.0 ± 2.0
Scattered particle mass	99.0 ± 1.0
TOF-ADC	99.0 ± 1.0
Total (ϵ_{cs})	74 ± 3

Table 3.4: Contents of the event-selection efficiency (ϵ_{cs}) and estimated percentages.

z-vertex resolution was worse for the forward scattering angle. The corresponding cut efficiency was estimated to be $90.0 \pm 2.0\%$ by the same method as in the previous case.

With these cuts applied, K^+ events were clearly separated from background events, as shown in Figs.3.7 and 3.8-(a). In these figures, event-selection criteria on the scattered particle mass and TOF-ADC are shown as solid lines. The corresponding cut efficiency was estimated to be $99.0 \pm 1.0\%$ for each parameter, where the tails of those distributions were fitted with Gaussians. The error is the statistical fluctuation of the estimation. The obtained cut efficiencies are summarized in Table 3.4.

Summary

The estimated efficiency factors are summarized in Table 3.1. The total relative error was calculated as the root-sum-square of the relative errors, considering that they were estimated statistically.

3.6.2 Systematic errors

The total systematic error of the cross section is summarized in Table 3.5 for each target. The error in the acceptance is assumed to be the statistical fluctuation of the Monte-Carlo calculation described in appendix D. The error of the target thickness is taken from Table 2.6.

3.6.3 Consistency of the $^{12}_\Lambda\text{C}$ ground-state cross section

In order to examine the consistency of the cross section calculation, particularly about the beam-intensity dependence of the efficiency, the $^{12}_\Lambda\text{C}$ ground-state cross section was calculated for each experimental cycle separately, and for special $^{12}_\Lambda\text{C}$ data

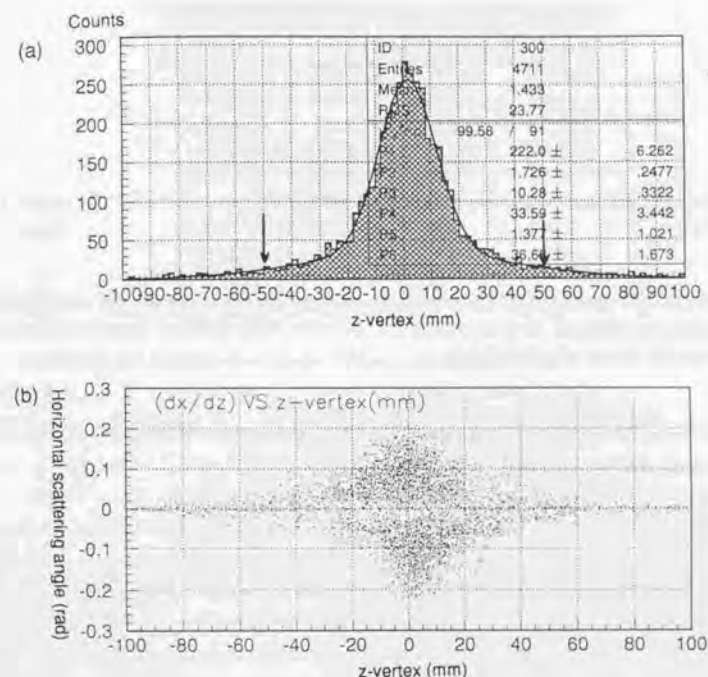


Figure 3.13: (a) z-vertex distribution at the target for the 93-02 cycle $^{12}_\Lambda\text{C}$ data. The solid line shows a Gaussian fitting curve. The arrows indicate the cut points. (b) A scatter plot between the z-vertex and the horizontal scattering angle at the target for the 93-02 cycle $^{12}_\Lambda\text{C}$ data.

Targets	Systematic errors (%)			
	$d\Omega$	Thickness	ϵ_{total}	Total
$^{12}_\Lambda\text{C}$	± 1.0	± 2.9	± 10	± 14
^{10}B	± 1.0	± 2.0	± 10	± 13
^{28}Si	± 1.0	± 2.0	± 10	± 13
^{89}Y	± 1.0	± 1.2	± 10	± 12
^{139}La	± 1.0	± 1.0	± 10	± 12
^{208}Pb	± 1.0	± 5.0	± 10	± 16

Table 3.5: Total systematic error of the cross section for each target.

Cycles	BEAM rates (M/spill)	N_{BEAM} (G)	Cross section ($\mu\text{b/sr}$)
92-11	3.4	30.12	7.6 ± 0.6
92-12	3.9	58.48	6.9 ± 0.4
93-02	2.4	76.81	6.5 ± 0.4
93-03	2.9	82.28	6.5 ± 0.4
93-04	2.9	70.93	7.3 ± 0.4
93-04	1.0	3.69	7.7 ± 1.2
93-04	2.1	4.64	7.7 ± 1.2
93-04	2.9	3.56	7.3 ± 1.2

Table 3.6: ^{12}C ground-state cross section averaged over the spectrometer acceptance for each experimental cycle and that for ^{12}C data with different beam intensities. The quoted errors are statistical.

taken with different beam intensities. The results are given in Table 3.6. They are consistent with one another.

Calibration data	QQDQQ (GeV/c)	SKS (mode)
$^{12}\text{C}(\pi^+, K^+)$	1.06	2.2 T
π^+ beam	$0.65 \sim 0.82$	2.2 T
π^+ beam	1.06	3.0 T
π^+ beam with a target	1.06	3.0 T

Table 3.7: List of the calibration data used for examining and calibrating the energy scale.

3.7 Energy precision and resolution

A shift in the hypernuclear mass (δM_{HY}) can be written as

$$\begin{aligned}
\delta M_{HY} &= \left(\frac{\partial M_{HY}}{\partial p_\pi} \right) \delta p_\pi + \left(\frac{\partial M_{HY}}{\partial p_K} \right) \delta p_K + \left(\frac{\partial M_{HY}}{\partial \theta} \right) \delta \theta \\
&\sim \frac{1}{\beta_\pi} \delta p_\pi - \frac{1}{\beta_K} \delta p_K - \frac{p_\pi p_K}{M_{HY}} \sin \theta \delta \theta \\
&\sim \frac{1}{\beta_\pi} \delta p_\pi - \frac{1}{\beta_K} \delta p_K
\end{aligned} \tag{3.11}$$

by using Eq.(3.1). The third term involving θ is negligible even for the lightest target, because $|\sin \theta \delta \theta|$ is typically smaller than 0.001. Since the beam spectrometer was calibrated with SKS (described in section 3.2), the momentum precision of the beam spectrometer is determined by that of SKS. Thus, the energy precision is determined by the momentum precision of SKS.

As mentioned in section 3.3, the momentum precision of SKS suffers systematic errors in the magnetic field map and in the drift-chamber geometry parameters. Therefore, in order to achieve an energy precision as small as 0.1 MeV (0.01%), the momentum scale had to be calibrated using some calibration data.

In this section, at first, the calibration data used for examining and calibrating the momentum scale are described in detail. Table 3.7 lists those calibration data and their spectrometer settings. Next, the energy scale precision and the energy resolution are discussed on the basis of the calibration.

Cycles	^{12}C g.s. widths (FWHM)	Level spacings
92-12	1.7 ± 0.4 MeV	11.0 ± 0.5 MeV
93-02	2.0 ± 0.4 MeV	10.7 ± 0.5 MeV
93-03	2.2 ± 0.4 MeV	10.7 ± 0.5 MeV
93-04	2.0 ± 0.4 MeV	10.7 ± 0.5 MeV
total	2.0 ± 0.1 MeV	10.8 ± 0.1 MeV

Table 3.8: Widths of the ground-state peak and level spacings between the s_A and p_A peaks in ^{12}C spectra. The quoted errors are statistical.

3.7.1 Calibration data

$^{12}\text{C}(\pi^+, K^+)$ data

Under the (π^+, K^+) condition, SKS was operated in the 2.2 T mode, where the central momentum was 0.72 GeV/c while the beam spectrometer was set for 1.06 GeV/c. Unfortunately, the beam could not be passed through the two spectrometers under this condition, and there was no good calibration reactions with such a large momentum transfer other than the (π^+, K^+) reaction, itself. Therefore, the $^{12}\text{C}(\pi^+, K^+)$ data were used for the purpose of spectrometer calibration. In this respect, they were taken not at once, but separately, at the beginning and end of each experimental cycle.

We assume that the binding energy² of the ^{12}C ground state is 10.76 MeV. This was based on other experimental data (appendix E). In order to keep this assumption, the SKS momentum scale was shifted by about -4 MeV, with a precision of ± 0.25 MeV (a fitting error). Consequently, all of the energies obtained in this thesis suffer an error based on this assumption. Note that a shift of the SKS momentum is approximately equivalent to a shift of the beam momentum, as shown in Eq.(3.11).

The width of the ^{12}C ground-state peak directly shows the experimental energy resolution. As shown in Table 3.8, the resolution was stable during the experiment. In addition, the level spacing between the s_A and p_A peaks was also stable.

π^+ beam at 0.65~0.82 GeV/c

In order to examine the uniformity of the SKS momentum scale in the 2.2 T mode, π^+ beam data were taken at several central beam momenta from 0.65 to 0.82 GeV/c by a 2% step. Since this momentum scale was not affected by the beam-spectrometer

²See section 4.1 about the definition of the binding energy.

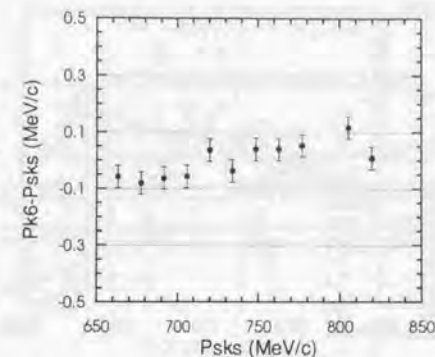


Figure 3.14: Momentum difference measured by the two spectrometers, QDQD and SKS, as a function of the central beam momentum for π^+ beams.

calibration with SKS, it is suitable for checking the SKS momentum scale, except for the absolute value. Figure 3.14 shows the momentum difference measured by the two spectrometers, QDQD and SKS, as a function of the central beam momentum. It was found that the uniformity was better than ± 0.06 MeV/c in the momentum range below 800 MeV/c, which range was relevant to hypernucleus production.

These calibration data were also used for examining the momentum dependence of the momentum resolution of SKS in the 2.2 T mode. Figure 3.15 shows the total momentum resolution, $\sigma = (\sigma_{SKS}^2 + \sigma_{QDQD}^2)^{1/2}$, as a function of the central beam momentum, where σ_{SKS} and σ_{QDQD} are the momentum resolution of SKS and QDQD, respectively. Since the QDQD system was calibrated with SKS, we assume $\sigma_{SKS} \simeq \sigma_{QDQD}$. Then, the momentum dependence can be approximately written as

$$\frac{\sigma_{SKS}}{p_{SKS}} \simeq 4.8 \times 10^{-7} p_{SKS} + 3.0 \times 10^{-4}, \quad (3.12)$$

where σ_{SKS} and p_{SKS} are in MeV/c. The resolution changes by only 0.023 MeV/c (FWHM) for a momentum change of 10 MeV/c. Although the beam angular range is smaller than that of (π^+, K^+) data, these data cover almost the entire acceptance of the spectrometer in total. Therefore, we conclude the dependence is also small for the (π^+, K^+) data.

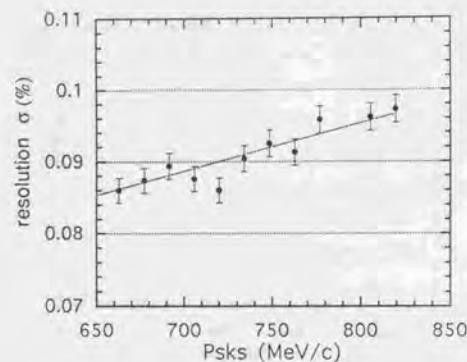


Figure 3.15: Total momentum resolution of the two spectrometers, QDDQQ and SKS, for π^+ beams as a function of the central beam momentum. The solid line is from a least-square fit.

π^+ beam at 1.06 GeV/c

For the beam-spectrometer calibration with SKS, 1.06 GeV/c π^+ beams were passed through the beam spectrometer and SKS in the 3.0 T mode several times in each cycle. The calibration procedure is described in appendix C. The calibration parameters were stable during the experiment.

π^+ beam at 1.06 GeV/c with a target

In order to correct the target energy loss and to estimate the contribution of its fluctuation to the energy resolution, the target energy-loss and its straggling were measured for a 1.06 GeV/c π^+ beam. As an example, Fig.3.16 shows a distribution of the momentum loss measured by SKS and QDDQQ without or with the carbon target. The energy loss was calculated as the centroid shift of Gaussian fitting. The energy-loss straggling was calculated as the root-difference-square of the widths. The results are given in Table 3.9. Since the spectrometer resolution is comparable to the straggling, the obtained energy-loss straggling suffers large errors.

The measured stragglings are compared with calculations based on the Landau or Vavilov distribution [49] in Fig.3.17. (They are almost subject to the Landau distribution.)

The measured energy losses are compared with three kinds of calculations in

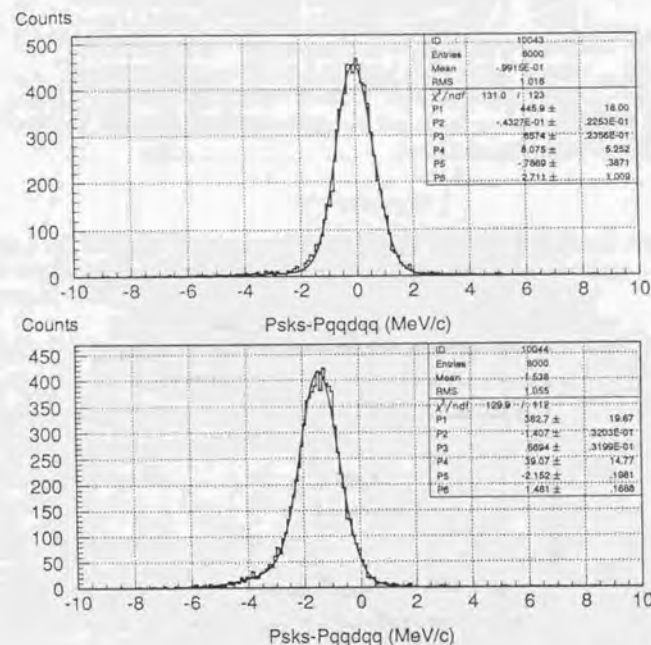


Figure 3.16: Distribution of the momentum loss measured by QDDQQ and SKS without (up) and with (down) the carbon target for a 1.06 GeV/c π^+ beam.

Targets	Notation	Energy loss	Straggling (FWHM)
^{12}C	C(5mm)	1.43 ± 0.1 MeV	0.57 ± 0.57 MeV
^{28}Si	Si(10mm)	3.58 ± 0.1 MeV	0.91 ± 0.41 MeV
^{89}Y	Y(7mm)	3.94 ± 0.1 MeV	1.16 ± 0.34 MeV
^{139}La	La(6mm)	4.13 ± 0.1 MeV	1.25 ± 0.31 MeV
^{208}Pb	Pb(3mm)	3.56 ± 0.1 MeV	1.25 ± 0.31 MeV

Table 3.9: Target energy losses and stragglings measured for a 1.06 GeV/c π^+ beam. The quoted errors are statistical.

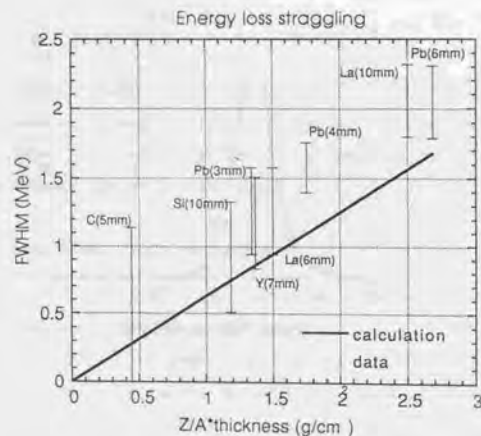


Figure 3.17: Measured target energy-loss stragglings (bars) compared with calculations using the Landau or Vavilov distribution (solid line) for a 1.06 GeV/c π^+ beam.

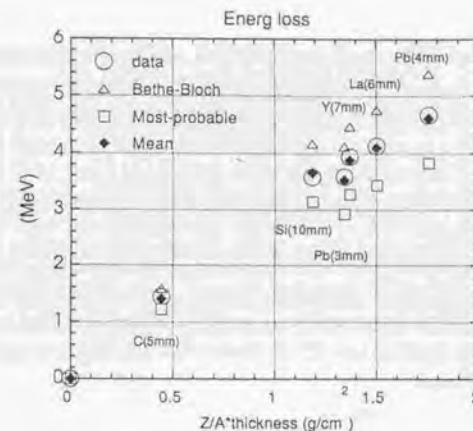


Figure 3.18: Measured target energy losses for 1.06 GeV/c π^+ compared with three kinds of calculations: the Bethe-Bloch formula, the most probable energy loss, and their mean values.

Fig.3.18; the Bethe-Bloch and the most probable energy loss are shown together with their mean values. Since the straggling distribution is asymmetric, the experimentally obtained energy loss by Gaussian fitting is between the mean energy loss and the most probable energy loss. Actually, they agree well with their mean values, as shown in the figure.

3.7.2 Energy precision

The uniformity of the SKS momentum scale was shown to be better than ± 0.06 MeV/c ($\pm 0.0083\%$). Since QQDQQ was calibrated with SKS, the result is expected to be similar for QQDQQ. The momentum scale was shifted in order to adjust the $^{12}_\text{A}\text{C}$ ground-state peak at the defined binding energy with a precision of $\pm 0.25 + \Delta E$ MeV, where ΔE is the error of the definition. Consequently, the total systematic error of the hypernuclear mass becomes $\pm 0.08/\beta_\pi \pm 0.06/\beta_K \pm 0.25 + \Delta E = \pm 0.4 + \Delta E$ MeV for the carbon target by using Eq.(3.11).

For other targets, the π^+ and K^+ momentum have to be corrected by the target energy loss. Table 3.10 shows the energy losses and the stragglings calculated for K^+ (0.72 GeV/c) and π^+ (1.06 GeV/c). Comparisons of Tables 3.10 and 3.9 show that the energy-loss difference between the carbon and another target can be estimated with a precision of better than ± 0.1 MeV. Therefore, the total systematic error is

Targets	Energy-loss straggling		Energy loss		R_{target} (FWHM)
	FWHM(π)	FWHM(K)	E.loss(π)	E.loss(K)	
$^{12}_A\text{C}$	0.27 MeV	0.40 MeV	1.40 MeV	1.78 MeV	0.40 MeV
$^{10}_A\text{B}$	0.66 MeV	0.97 MeV	3.47 MeV	4.36 MeV	0.96 MeV
$^{28}_A\text{Si}$	0.74 MeV	1.07 MeV	3.66 MeV	4.41 MeV	0.95 MeV
$^{89}_A\text{Y}$	0.86 MeV	1.23 MeV	3.88 MeV	4.46 MeV	1.01 MeV
$^{139}_A\text{La}$	0.94 MeV	1.35 MeV	4.10 MeV	4.71 MeV	1.20 MeV
$^{208}_A\text{Pb}$	0.84 MeV	1.21 MeV	3.53 MeV	5.23 MeV	1.42 MeV

Table 3.10: Calculated energy-loss stragglings (FWHM) and the mean values (E.loss) between the Bethe-Bloch mean energy loss and the most probable energy loss for π^+ (1.06 GeV/c) and K^+ (0.72 GeV/c). The target energy-loss fluctuation is denoted by R_{target} .

Spectra	Specifications of the energy scale	
	Systematic errors	Resolution (FWHM)
$^{12}_A\text{C}$	$\pm 0.4 + \Delta E$ MeV	2.0 ± 0.1 MeV
$^{10}_A\text{B}$	$\pm 0.5 + \Delta E$ MeV	2.2 ± 0.1 MeV
$^{28}_A\text{Si}$	$\pm 0.5 + \Delta E$ MeV	2.2 ± 0.1 MeV
$^{89}_A\text{Y}$	$\pm 0.5 + \Delta E$ MeV	2.2 ± 0.1 MeV
$^{139}_A\text{La}$	$\pm 0.5 + \Delta E$ MeV	2.3 ± 0.1 MeV
$^{208}_A\text{Pb}$	$\pm 0.5 + \Delta E$ MeV	2.4 ± 0.1 MeV

Table 3.11: Energy scale precision and the energy resolution for each spectrum, where ΔE is the error of the definition of a $^{12}_A\text{C}$ ground-state binding energy of 10.76 MeV.

$\pm 0.5 + \Delta E$ MeV for other targets. The results are summarized in Table 3.11.

3.7.3 Energy resolution

The experimental energy resolution for the $^{12}_A\text{C}$ ground-state peak was shown to be 2.0 ± 0.1 MeV (FWHM). A question to be answered is how much the resolution would be at different values of the hypernuclear mass and for other targets.

The experimental energy resolution (R_{energy}) consists of the momentum resolution of SKS and QQDQQ (r_{SKS} and r_{QQDQQ}) and the target energy-loss fluctuation (R_{target}):

$$R_{energy}^2 \sim \frac{1}{\beta_K^2} r_{SKS}^2 + \frac{1}{\beta_\pi^2} r_{QQDQQ}^2 + R_{target}^2. \quad (3.13)$$

The momentum dependence of r_{SKS} and r_{QQDQQ} was shown to be small on the

average. Consequently, the energy dependence of R_{energy} may be small, assuming that the correlation between the two spectrometers is small.

For other targets, different values of R_{target} should be used. They were calculated by

$$R_{target}^2 \sim \left(\frac{1}{2}\text{FWHM}(\pi) + \frac{1}{2}\text{FWHM}(K)\right)^2 + \frac{1}{3}(\text{E.loss}(\pi) - \text{E.loss}(K))^2, \quad (3.14)$$

and are shown in Table 3.10. The first term is for the energy-loss straggling for π^+ and K^+ . The second term comes from the ambiguity of the reaction point in the target. The calculated energy resolutions are summarized in Table 3.11 for each target.

Spectra	Background
$^{12}_{\Lambda}\text{C}$	$< 0.03 \mu\text{b/sr/MeV}$
$^{10}_{\Lambda}\text{B}$	$< 0.05 \mu\text{b/sr/MeV}$
$^{28}_{\Lambda}\text{Si}$	$< 0.04 \mu\text{b/sr/MeV}$
$^{89}_{\Lambda}\text{Y}$	$< 0.03 \mu\text{b/sr/MeV}$
$^{139}_{\Lambda}\text{La}$	$< 0.03 \mu\text{b/sr/MeV}$
$^{208}_{\Lambda}\text{Pb}$	$< 0.06 \mu\text{b/sr/MeV}$

Table 3.12: Background levels in the overbound regions.

3.8 Background level

In order to extract spectroscopic information from a spectrum, the background level is important. Ideally, the background cross section and its energy dependence should be known for each spectrum. However, it could not be estimated directly, since most of peaks were not separated with the present energy resolution. Instead, in this section, the overbound regions of the spectra are examined, since the yields in these regions represent the background level. Next, in order to understand the energy dependence of the background level, no-target (π^+ , K^+) data are considered. Furthermore, the background due to K^+ decay is studied by a Monte-Carlo simulation. At last, those discussions are summarized.

3.8.1 Overbound regions in the spectra

Figures 3.19 and 3.20 show the overbound regions of the $^{12}_{\Lambda}\text{C}$, $^{10}_{\Lambda}\text{B}$, $^{28}_{\Lambda}\text{Si}$, $^{89}_{\Lambda}\text{Y}$, $^{139}_{\Lambda}\text{La}$ and $^{208}_{\Lambda}\text{Pb}$ spectra. The background yields are approximately uniform in the overbound regions. The obtained background levels are given in Table 3.12.

3.8.2 No-target (π^+ , K^+) data

The no-target (π^+ , K^+) data were analyzed using the same analysis program as that for the normal (π^+ , K^+) data. These data stand for background events associated with beam particles which passed through the target without any scattering or reaction. As an example, the mass spectrum for the 93-04 cycle no-target data is shown in Fig.3.21-(a), assuming the carbon kinematics. In addition, spectra without some event-selection criteria are also shown in Figs.3.21-(b) and (c). In these spectra, the background levels are approximately uniform over the energy scale. The obtained background cross sections are listed in Table 3.13.

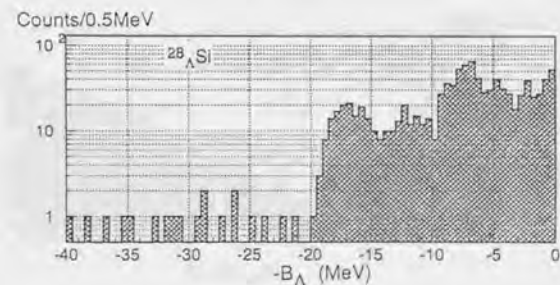
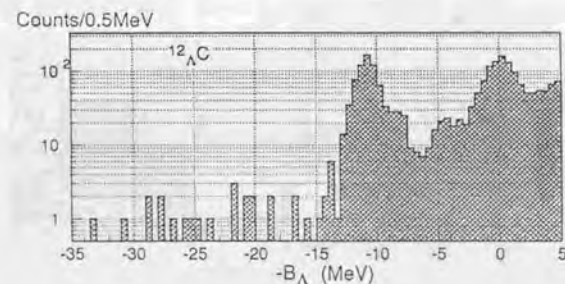
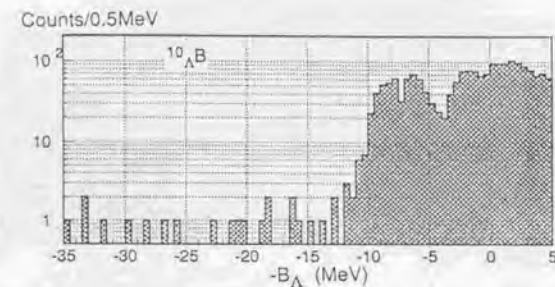


Figure 3.19: Overbound regions of the $^{10}_{\Lambda}\text{B}$, $^{12}_{\Lambda}\text{C}$ and $^{28}_{\Lambda}\text{Si}$ spectra.

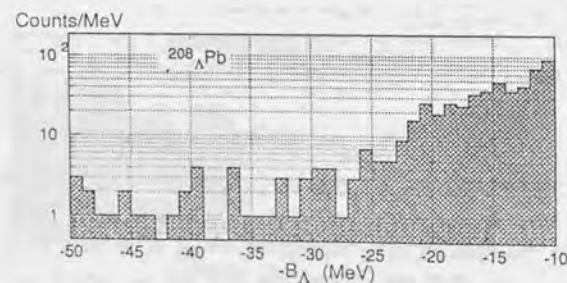
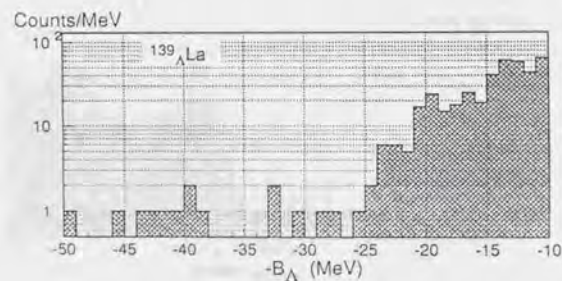
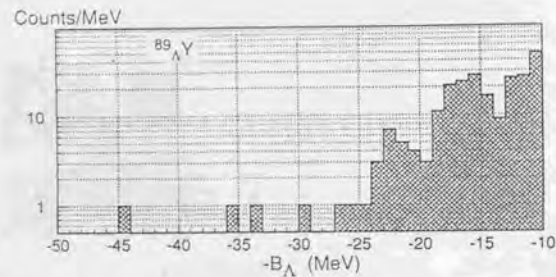


Figure 3.20: Overbound regions of the $^{89}_{\Lambda}\text{Y}$, $^{139}_{\Lambda}\text{La}$ and $^{208}_{\Lambda}\text{Pb}$ spectra.

Cycle	N_{BEAM}	Background (68% C.F.)
92-11	1.15 G	$< 0.03 \mu\text{b/sr/MeV}$
93-03	9.96 G	$< 0.10 \mu\text{b/sr/MeV}$
93-04	14.97 G	$< 0.06 \mu\text{b/sr/MeV}$

Table 3.13: Background levels for the no-target (π^+ , K^+) data.

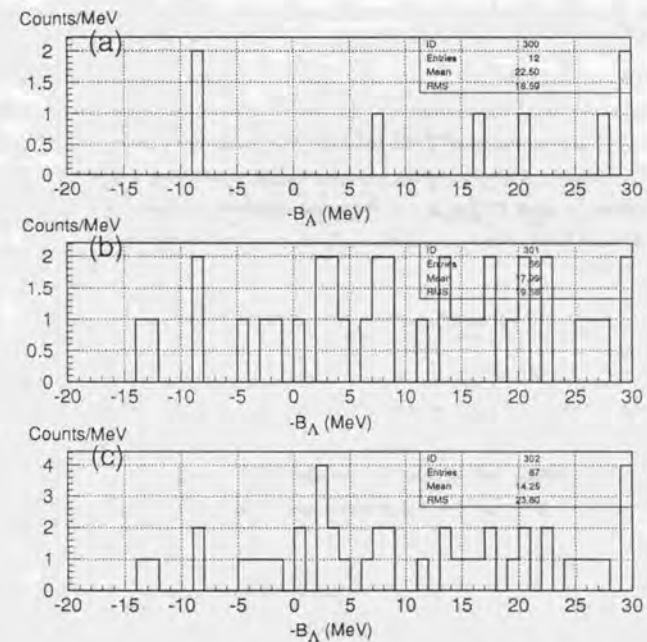


Figure 3.21: Mass spectra for the 93-04 cycle no-target (π^+ , K^+) data assuming the carbon kinematics: (a) by the normal (π^+ , K^+) analysis, (b) without the z -vertex cut, (c) without the z -vertex, the SDC3 tracking deviation and the scattered particle mass cuts.

3.8.3 K^+ decay

A Monte-Carlo simulation of the K^+ decay was described in section 3.6. It was found that, in the case of decays before SDC4XY, all of the decay events were rejected by the event-selection criteria. On the other hand, in the case of decays after SDC4XY, these events did not contribute to the background, since the momentum reconstruction in SKS and the time-of-flight measurement were not affected. Therefore, the background associated with the K^+ decay is negligible.

3.8.4 Summary

First, the background level in the overbound region was examined. It was found that the background level was approximately uniform there. Next, the background level for the no-target (π^+ , K^+) data was shown to be approximately uniform over the energy scale. Last, the background due to K^+ decays was shown to be negligible by a Monte-Carlo simulation. Unfortunately, the background level in the bound region is still unknown without having an assumption concerning the energy dependence. Therefore, in peak fitting in the following chapters, we assume implicitly that the background level is approximately uniform over the energy scale.

Chapter 4

Experimental results

In this chapter, the experimental results are presented. Physics discussions about the results are given in the next chapter.

4.1 Hypernuclear mass spectra

The hypernuclear mass spectra of ${}^{10}_{\Lambda}\text{B}$, ${}^{12}_{\Lambda}\text{C}$, ${}^{28}_{\Lambda}\text{Si}$, ${}^{89}_{\Lambda}\text{Y}$, ${}^{139}_{\Lambda}\text{La}$ and ${}^{208}_{\Lambda}\text{Pb}$ are shown in Figs.4.1, 4.2, 4.3, 4.4, 4.5, and 4.6, respectively, with two kinds of vertical scales: the experimental counts and the cross section,

$$\left(\frac{d\sigma}{d\Omega}\right) = \frac{A}{(\rho x)N_A} \cdot \frac{1}{N_{\text{BEAM}}} \cdot \sum_{i=1}^{N_K} \frac{1}{\epsilon_{\text{total}} d\Omega}, \quad (4.1)$$

where the symbols are defined in section 3.6. The cross section is averaged over the spectrometer angular acceptance, which covers scattering angles from 0° to 15° , as shown in appendix D.

In appendix F, the spectra are presented as tables. For convenience, specifications of the spectra discussed in the last chapter are summarized in Table 4.1.

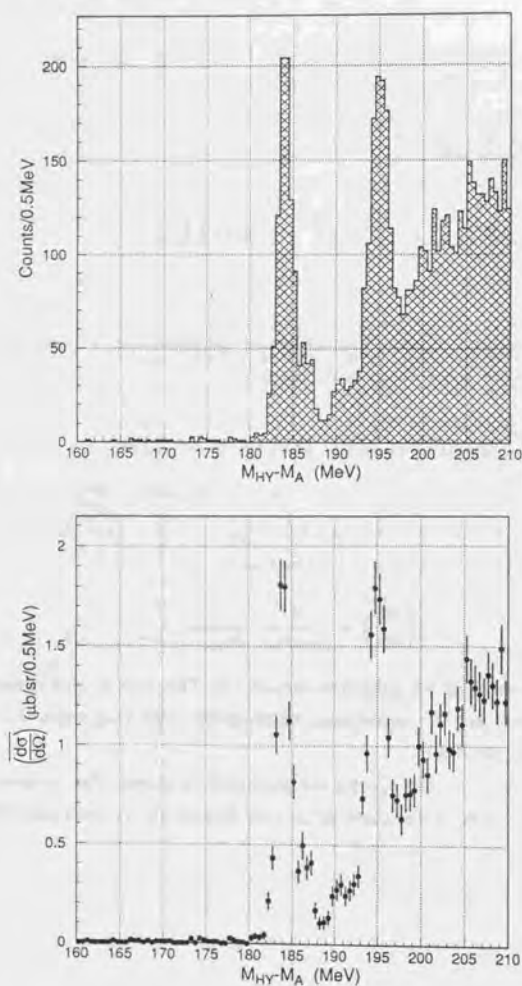


Figure 4.1: Hypernuclear mass spectra for $^{12}_{\Lambda}\text{C}$. The quoted errors are statistical.

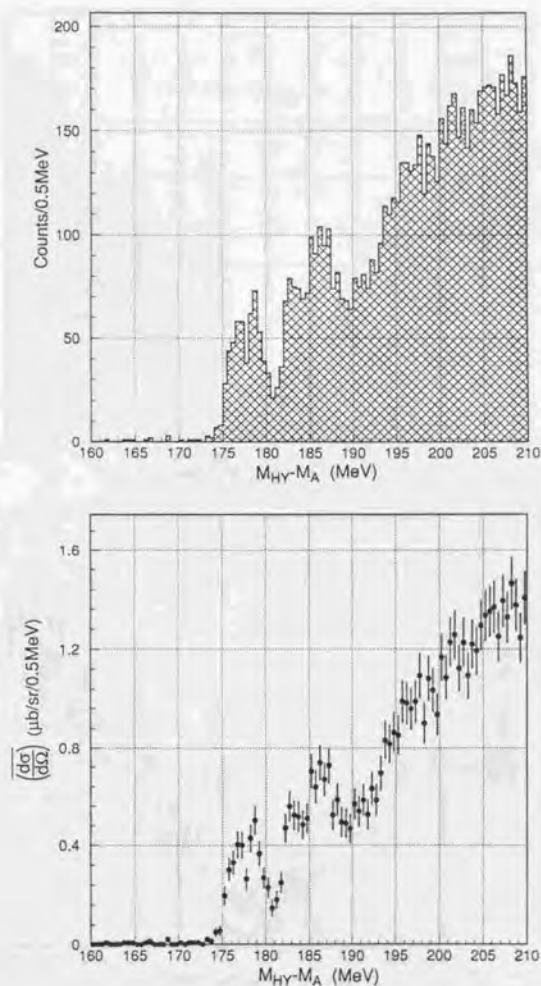


Figure 4.2: Hypernuclear mass spectra for $^{10}_{\Lambda}\text{B}$. The quoted errors are statistical.

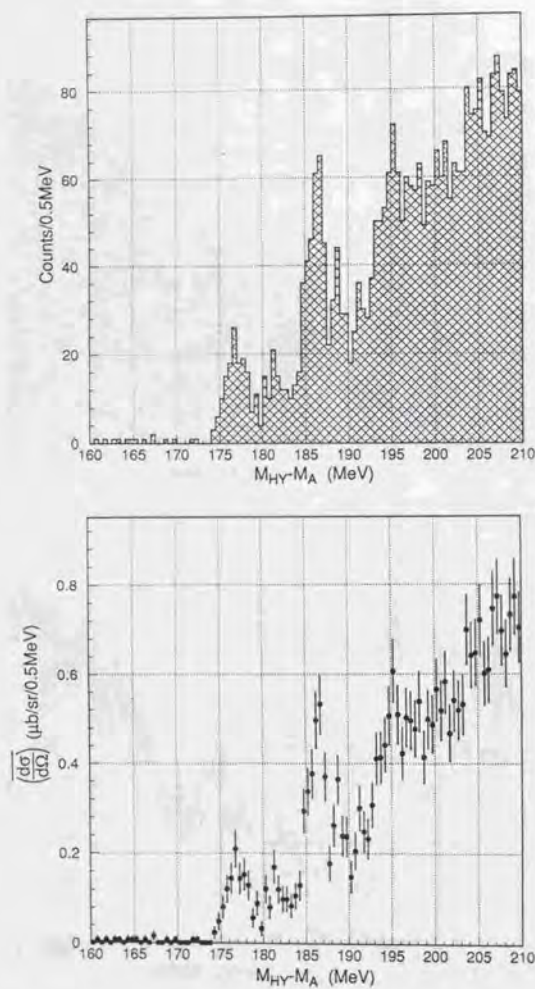


Figure 4.3: Hypernuclear mass spectra for $^{28}_{\Lambda}\text{Si}$. The quoted errors are statistical.

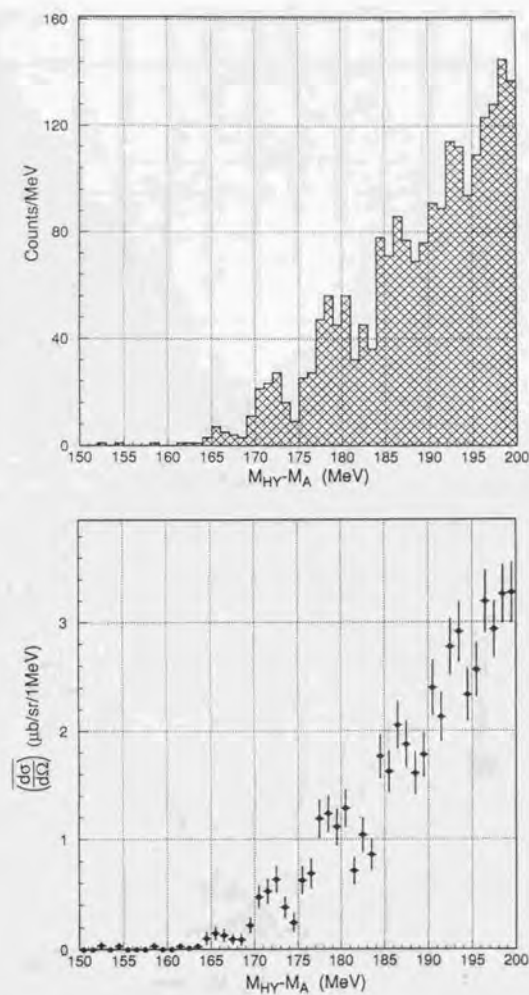


Figure 4.4: Hypernuclear mass spectra for $^{89}_{\Lambda}\text{Y}$. The quoted errors are statistical.

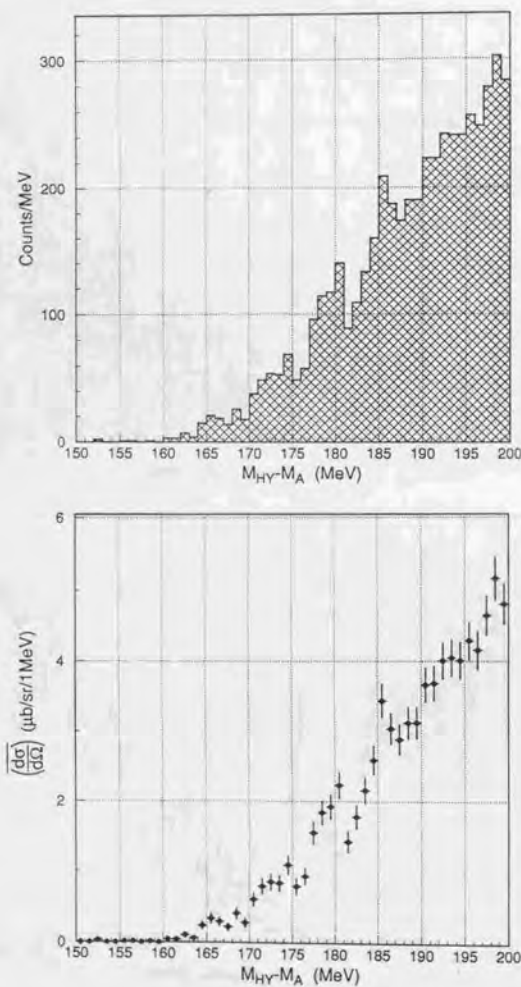


Figure 4.5: Hypernuclear mass spectra for $^{139}_{\Lambda}\text{La}$. The quoted errors are statistical.

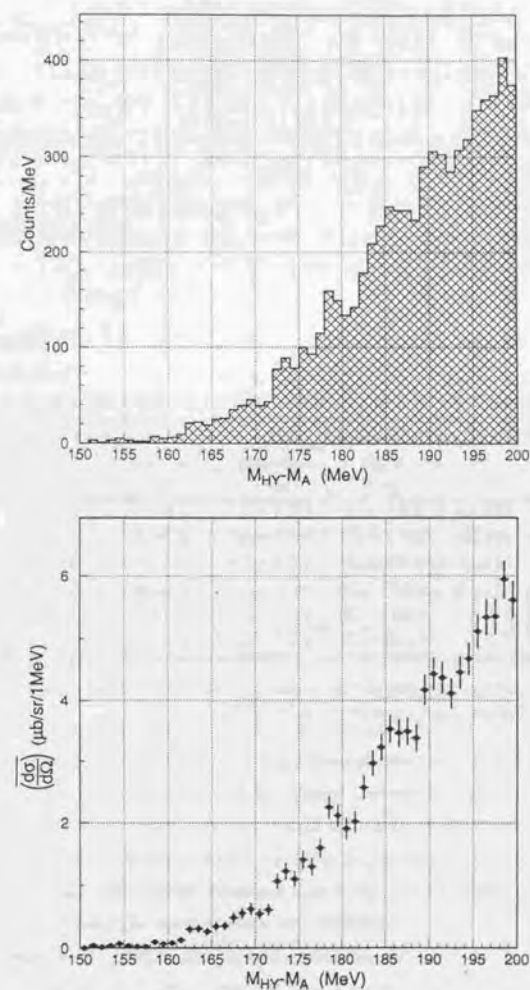


Figure 4.6: Hypernuclear mass spectra for $^{208}_{\Lambda}\text{Pb}$. The quoted errors are statistical.

Spectra	N_{BEAM} (G)	Scattering angle (rad)	Systematics			
			Energy (MeV)	Resolution (MeV)	Cross section	Background ($\mu\text{b}/\text{sr}/\text{MeV}$)
$^{12}_{\Lambda}\text{C}$	288.49	0.01-0.26	$\pm 0.4 + \Delta E$	2.0 ± 0.1	$\pm 14\%$	< 0.03
$^{10}_{\Lambda}\text{B}$	144.99	0.01-0.26	$\pm 0.5 + \Delta E$	2.2 ± 0.1	$\pm 13\%$	< 0.05
$^{28}_{\Lambda}\text{Si}$	147.86	0.01-0.26	$\pm 0.5 + \Delta E$	2.2 ± 0.1	$\pm 13\%$	< 0.04
$^{89}_{\Lambda}\text{Y}$	254.53	0.035-0.26	$\pm 0.5 + \Delta E$	2.2 ± 0.1	$\pm 12\%$	< 0.006
$^{139}_{\Lambda}\text{La}$	513.20	0.035-0.26	$\pm 0.5 + \Delta E$	2.3 ± 0.1	$\pm 12\%$	< 0.008
$^{208}_{\Lambda}\text{Pb}$	853.69	0.035-0.26	$\pm 0.5 + \Delta E$	2.4 ± 0.1	$\pm 16\%$	< 0.011

Table 4.1: Specifications of the spectra; ΔE is the error of the definition of the $^{12}_{\Lambda}\text{C}$ ground-state binding energy of 10.76 MeV.

Chapter 5

Discussion

5.1 Outline

In general, spectroscopic study in nuclear physics cannot avoid some model dependence. Ideally, if the energy resolution is sufficiently high and the background level is sufficiently low, the excitation energies, cross sections and widths can be determined unambiguously from observed spectra. If the system is sufficiently simple, they can be compared with model calculations on the basis of reliable state assignments. However, this will be not the case. Some assumptions based on a model have to be adopted. Furthermore, the model includes not only a nuclear structure part, but also descriptions of the reaction mechanism and models of the interaction. Since these three parts are closely related to one another, it is not easy to discuss one part without depending on some assumptions in the other two parts.

Usually, in order to reduce the ambiguity originating from such a model dependence, one measures additional spectroscopic information, such as the angular distribution, other than claiming a higher energy resolution and higher statistics. Coincidence detection of decay particles would also help to formulate reliable discussions. Unfortunately, in the case of Λ hypernuclei, this direction has not yet been fully explored, because of limited statistics due to the small cross section. In the present study, also, only the mass spectra are available.

Within these limits, physics discussions about the obtained spectra are given in this chapter. We present interpretations of the observed peak structure and calculate binding energies and cross sections by peak fitting based on simple assumptions. The results are compared with theoretical calculations so as to extract physics information. In section 5.2, light hypernuclei ($^{12}_{\Lambda}\text{C}$, $^{10}_{\Lambda}\text{B}$ and $^{28}_{\Lambda}\text{Si}$) are discussed from the viewpoint that fine peak structure corresponds to core-excited states. Precise

comparisons with theoretical calculations would provide us with information about the ΛN interaction. In section 5.3, heavy hypernuclei ($^{89}_{\Lambda}\text{Y}$, $^{139}_{\Lambda}\text{La}$ and $^{208}_{\Lambda}\text{Pb}$) are discussed. The observed peak structure is interpreted with an emphasis on the selectivity of the (π^+, K^+) reaction. In section 5.4, the mass-number dependence of the binding energy is discussed in conjunction with the independent single-particle picture of a Λ hyperon.

In the spectra given in this chapter, two kinds of energy scales are shown. One is the difference between the hypernuclear mass and the target nuclear mass ($M_{HY} - M_A$). The other is the binding energy (B_Λ), defined by

$$M_\Lambda + M_C - B_\Lambda = M_{HY}, \quad (5.1)$$

where M_Λ and M_C are the mass of a Λ hyperon and a core nucleus, respectively. Note that produced core nuclei are not always in their ground states, but are distributed over various neutron-hole states. For example, by analogy with neutron pick-up reactions (see appendix G), they are excited by 0.15, 0.99 and 1.63 MeV on the average for $^{89}_{\Lambda}\text{Y}$, $^{139}_{\Lambda}\text{La}$ and $^{208}_{\Lambda}\text{Pb}$, respectively. In order to take these distributions into account, M_C values shifted by these values are used for $^{89}_{\Lambda}\text{Y}$, $^{139}_{\Lambda}\text{La}$ and $^{208}_{\Lambda}\text{Pb}$ in the calculation of B_Λ .

5.2 Light Λ hypernuclei

5.2.1 $^{12}_{\Lambda}\text{C}$

The $^{12}_{\Lambda}\text{C}$ spectrum exhibits two prominent peaks at $B_\Lambda=11$ and 0 MeV and two small peaks between them. The two large peaks were already observed in previous (π^+, K^+) experiments [24, 25, 26, 27]. They were interpreted as being neutron-hole Λ -particle configurations, $[0p_{3/2}^{-1}s_\Lambda]$ and $[0p_{3/2}^{-1}p_\Lambda]$, respectively, on the basis of measured angular distribution [24]. A level spacing of about 11 MeV is consistent with the other experiments. Since the s_Λ peak consists of almost one state [50, 51], the width represents an experimental energy resolution of 2 MeV (FWHM), as already mentioned in section 3.7.

The two small peaks were resolved for the first time, although non-negligible strength between the s_Λ and p_Λ peaks was in question before [14, 26, 52]. Considering that a hypernucleus ($^{12}_{\Lambda}\text{C}$) consists of a Λ hyperon and a core nucleus (^{11}C), these states will correspond to excited core configurations with the Λ hyperon in the s_Λ orbit. In a neutron pick-up (p, d) reaction on ^{12}C , the excited states of ^{11}C at 2.0

Peaks	$M_{HY} - M_A$ (MeV)	Errors (MeV)	B_Λ (MeV)	FWHM (MeV)	Cross sections ($\mu\text{b/sr}$)
#1	184.0	(fixed)	10.8	2.0 ± 0.1	7.3 ± 0.4
#2	186.7	± 0.2	8.1	2.0 ± 0.1	1.7 ± 0.2
#3	190.9	± 0.3	3.9	3.3 ± 0.7	2.0 ± 0.4
#4	194.9	± 0.1	-0.1	2.6 ± 0.2	9.4 ± 0.6

Table 5.1: Results of the Gaussian fitting for $^{12}_{\Lambda}\text{C}$ described in the text. The numbering of the peaks is from the ground to the excited states. The quoted errors are statistical.

($1/2^-$) and 4.8 ($3/2^-$) MeV are populated with strengths of 10-20% relative to the ground state (see appendix G). Since the neutron pick-up reaction is analogous to the (π^+, K^+) reaction in the respect that a neutron hole is produced, the two small peaks may be closely related to these two core excited states.

In order to obtain the binding energies and cross sections of the observed peaks, the spectrum was fitted by four Gaussians and a quasifree part. The quasifree part, representing a continuum spectrum in the unbound region, was fitted by a 2nd-order polynomial; it was constrained to be zero at $B_\Lambda=0$ and folded with the energy resolution. The Gaussian widths were made free parameters in the fitting. The results are given in Table 5.1 and Fig.5.1-(b). The excitation energies of the #2 and #3 peaks are slightly larger than those of the two excited states of ^{11}C , mentioned above. These energy shifts will reflect the influence of a Λ hyperon on the core nucleus and carry information on the ΛN interaction.

The obtained ground-state cross section is compared with other (π^+, K^+) experimental results [26, 27] in Table 5.2. Taking account of the calculated angular distribution [50, 51], the present result should be multiplied by 1.5, 1.4, 1.2 and 0.8 to be approximately compared with the cross sections at 0° , 3° , 6° and 10° , respectively. The present central values are slightly smaller than those of the other (π^+, K^+) experiments.

A preliminary theoretical $^{12}_{\Lambda}\text{C}$ spectrum based on a configuration-mixing shell model [50, 51, 53] is shown in Fig.5.1-(a). The four-peak structure well coincides with the measured spectrum. In the calculation, two small peaks are dominantly related to the two core excited states. In this model, mixing of core levels due to a

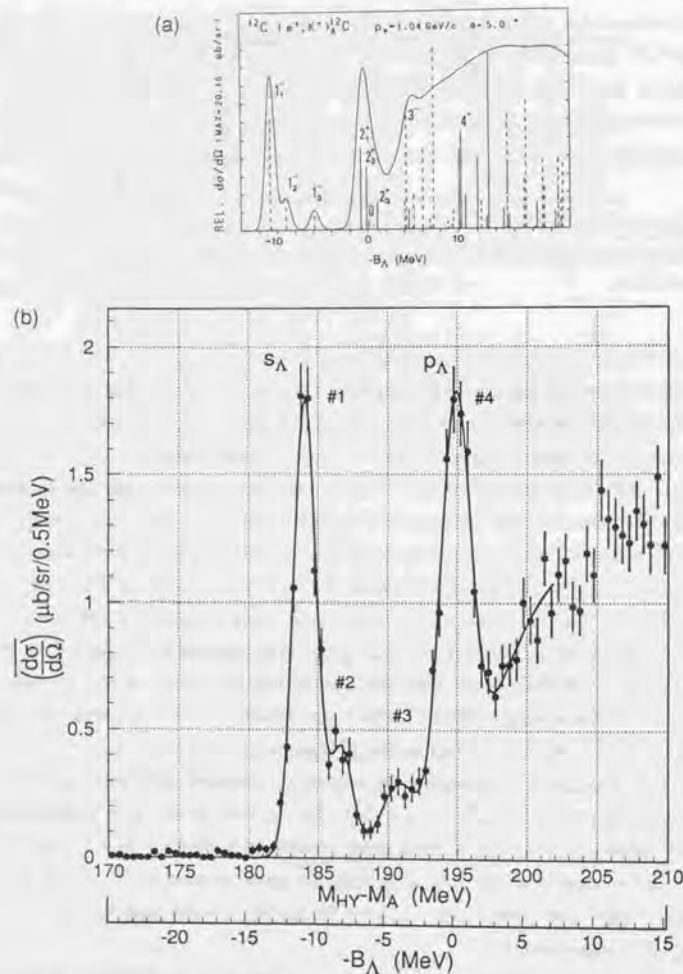


Figure 5.1: (a) Preliminary theoretical ^{12}C spectrum based on a configuration-mixing shell model with the Nijmegen-F AN interaction [50, 51, 53]. (b) The observed ^{12}C spectrum with a fitting curve described in the text.

$\mu\text{b/sr}$	θ	^{12}C g.s.	^{28}Si g.s.	^{89}Y g.s.	^{139}La g.s.	^{208}Pb g.s.
BNL[24]	5.6°	13 ± 2	-	-	-	-
BNL[26]	10°	10.36 ± 0.61	2.06 ± 0.34	0.54 ± 0.38	-	-
KEK[27]	3°	15 ± 4	-	-	-	-
Present	$0.6 \sim 15^\circ$	9.0 ± 0.6	1.2 ± 0.5	-	-	-
	$2.0 \sim 15^\circ$	(#1 + #2)	(#1)	0.6 ± 0.1	0.2 ± 0.1	0.2 ± 0.1
DWIA[17]	0°	17.4	8.9	1.7	1.4	0.7
	10°	8.4	4.6	0.8	0.4	0.2

Table 5.2: Comparisons of the obtained cross sections with other experimental results and DWIA calculations with a Woods-Saxon potential [54, 53]. The quoted errors of the present results are statistical.

A hyperon is introduced by diagonalizing Hamiltonian,

$$\mathcal{H} = H_N^{\text{Cohen-Kurath}} + t_\Lambda + \xi(l_\Lambda \cdot s_\Lambda) + \sum_N v_{\Lambda N}, \quad (5.2)$$

where t_Λ is the kinetic energy of a Λ hyperon, $\xi(l_\Lambda \cdot s_\Lambda)$ is the ls force for Λ orbits, and $v_{\Lambda N}$ is the ΛN interaction. For the core-nucleus part, the Cohen-Kurath shell-model Hamiltonian ($H_N^{\text{Cohen-Kurath}}$) and its wave functions [55] are adopted, since spectroscopic factors of the p-shell nuclei are generally well reproduced by the Cohen-Kurath shell model [55, 56, 57]. The ls term coefficient (ξ) is assumed to be small (-0.4 MeV), which is inferred from a $^{13}\text{C}(K^-, \pi^-)^{12}\text{C}$ experiment [59]. For the interaction part, the YNG interaction [60] with a phenomenological ΛN interaction model, the Nijmegen-F (NF) model [2], is used. In treating the reaction, the DWIA formalism is adopted.

The obtained excitation energies and relative strengths are compared with calculations in Table 5.3, where calculations for other ΛN interaction models (Nijmegen-D (ND), soft core (NS) and Jülich A (JA), B (JB) [2, 3]) are also shown. Concerning the excitation energies, the NS model predicts similar energy shifts best among these models. The NS potential is characterized by a stronger spin singlet (1S_0) component compared to a spin triplet (3S_1) one [30, 31]. In this respect, the present data favor a stronger spin singlet force. It is also supported by experimental data concerning the spin doublet of $^4_\Lambda\text{H}$ ($^4_\Lambda\text{He}$) [31, 61].

To be precise, however, the measured energies and strengths are not consistent with any of the models. The following points should be mentioned at present. The #3 peak is wider than the experimental energy resolution. This may indicate that it is not a single state, and thus stimulate a question about the interpretation of

Peaks	Excitation energies (MeV)						Neutron pick-up
	(π^+, K^+)						
	Exp.	ND	NF	NS	JA	JB	
#1	0.0	0.0	0.0	0.0	0.0	0.0	0.0
#2	$2.6 \pm 0.2 \pm 0.4$	2.0	2.0	2.4	1.7	1.9	2.0
#3	$6.8 \pm 0.3 \pm 0.4$	5.3	5.3	5.9	5.0	4.9	4.8

Peaks	Relative strength						Neutron pick-up
	(π^+, K^+)						
	Exp.	ND	NF	NS	JA	JB	
#1	1.00	1.00	1.00	1.00	1.00	1.00	1.00
#2	0.24 ± 0.05	0.31	0.29	0.12	0.38	1.24	0.10
#3	0.28 ± 0.08	0.15	0.14	0.08	0.17	0.60	0.17

Table 5.3: Comparisons of obtained excitation energies and relative strengths with theoretical calculations ($\theta = 10^\circ$) for $^{12}_\Lambda\text{C}$.

this peak. It is pointed out that one may have to consider a two-step process [53] where an incoming π^+ excites the core nucleus before the (π^+, K^+) reaction, or an outgoing K^+ excites the hypernucleus, as in the case of neutron pick-up reactions [57, 62]. Furthermore, the Cohen-Kurath wave functions in the model should be examined more carefully. There might be a possibility of a large core deformation, as is important for $^9_\Lambda\text{Be}$ and $^{20}_\Lambda\text{Ne}$ in connection with cluster aspects [17]. Thus, for conclusive discussions about the ΛN interaction, the reaction mechanism and the hypernuclear wave functions must be better understood.

The width of the p_Λ peak is wider than the energy resolution. The p_Λ peak populated by the (π^+, K^+) reaction includes an $1s$ pair, $p_{1/2}$ and $p_{3/2}$, as the major components. Although the p_Λ states are proton unbound, the corresponding width is expected to be as narrow as 0.4 MeV [64]. Therefore, the wider width may indicate a finite value of the $1s$ splitting. Assuming two Gaussians of equal strength with a width of 2.0 ± 0.1 MeV for the p_Λ peak, fitting leads to a splitting of 1.2 ± 0.5 MeV. This value is consistent with an emulsion result of 0.75 ± 0.1 MeV [64].

5.2.2 $^{10}_\Lambda\text{B}$

The $^{10}_\Lambda\text{B}$ spectrum exhibits three narrow peaks in the bound region and a broader peak in the unbound region. This fine peak structure was resolved for the first time. A ground-state binding energy of about $B_\Lambda = 8$ MeV is consistent with emulsion [65] and (K^-, π^-) [66] results. Since the excitation energies of the p_Λ orbit are expected

Peaks	$M_{HY} - M_\Lambda$ (MeV)	Errors (MeV)	B_Λ (MeV)	FWHM (MeV)	Cross sections ($\mu\text{b}/\text{sr}$)
#1	176.4	± 0.2	8.1	2.2 (fixed)	1.8 ± 0.3
#2	179.0	± 0.2	5.5	2.2 (fixed)	2.0 ± 0.3
#3	182.3	± 0.2	1.7	2.2 (fixed)	2.2 ± 0.4
#4-L	185.1	± 0.2	-0.6	2.2 (fixed)	2.0 ± 0.3
#4-R	186.9	± 0.2	-2.4	2.2 (fixed)	2.0 ± 0.3

Table 5.4: Results of the Gaussian fitting for $^{10}_\Lambda\text{B}$ described in the text. The numbering of the peaks is from the ground to the excited states. The quoted errors are statistical.

to be larger than 13 MeV [50, 51], all of these peaks belong to configurations of a Λ hyperon in the s_Λ orbit coupled with a core nucleus (^9B). By analogy with a neutron pick-up (p, d) reaction on ^{10}B , where the excited states of ^9B at 2.4 ($5/2^-$), 7.1 ($7/2^-$) and 11.5 ($7/2^-$) MeV are populated with considerable strengths (see appendix G), the three excited peaks are possibly related to these three core-excited states.

The spectrum was fitted by five Gaussians and a 2nd-order polynomial representing the continuum part. The width of the Gaussians was fixed to the energy resolution. Since the fourth peak is wider than the energy resolution, it is represented by two Gaussians. The results are shown in Table 5.4 and Fig.5.2-(b). The obtained excitation energies (2.6, 6.3 and 9.6 MeV) approximately correspond to the three excitation energies of ^9B mentioned above. A slight change of the levels will reflect the influence of a Λ hyperon on the core nucleus.

A preliminary theoretical $^{10}_\Lambda\text{B}$ spectrum based on the configuration-mixing shell model with the NF potential [50, 51, 53] is shown in Fig.5.2-(a). All four states are produced by $l=1$ transitions from p_N to s_Λ . It should be emphasized that the populations of these low-lying states are an advantage of the (π^+, K^+) reaction compared to the (K^-, π^-) reaction. Theoretical studies have to be progressed for quantitative discussions.

5.2.3 $^{28}_\Lambda\text{Si}$

The $^{28}_\Lambda\text{Si}$ spectrum exhibits three clear peaks at $B_\Lambda = 17, 12$ and 8 MeV in the bound region and a broad peak at $B_\Lambda = -1$ MeV in the unbound region. This spectrum shape is consistent with that reported by a BNL (π^+, K^+) experiment [26]. Considering

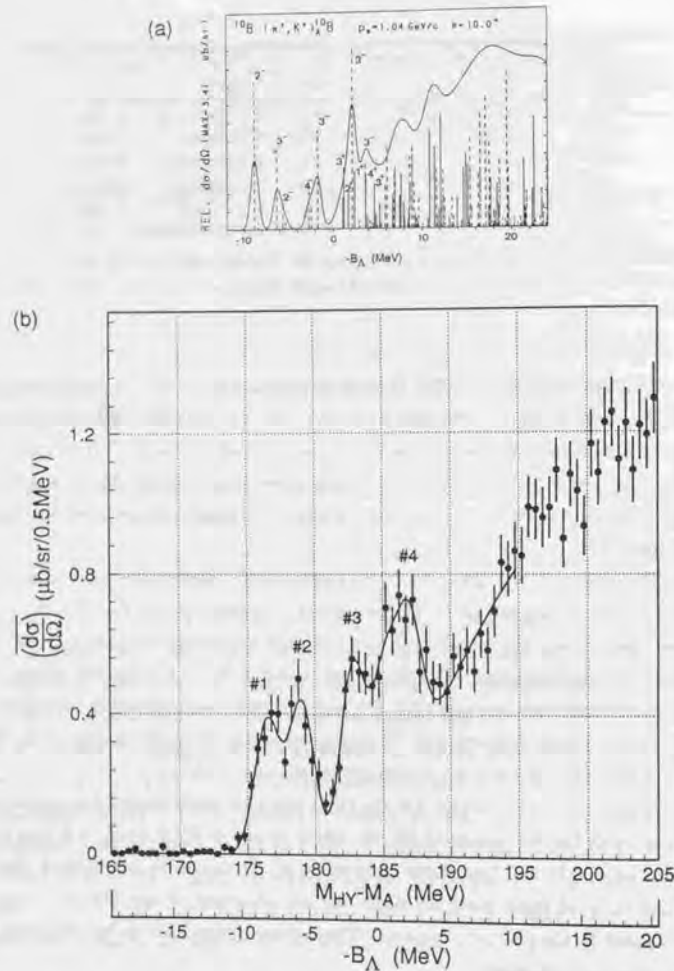


Figure 5.2: (a) Preliminary theoretical ^{10}B spectrum based on a configuration-mixing shell model with the Nijmegen-F AN interaction [50, 51, 53]. (b) The observed ^{10}B spectrum with the fitting curve described in the text.

Peaks	$M_{HY} - M_{\Lambda}$ (MeV)	Errors (MeV)	B_{Λ} (MeV)	FWHM (MeV)	Cross sections ($\mu\text{b/sr}$)
#1-L	177.5	± 0.5	17.4	2.2 (fixed)	0.7 ± 0.3
#1-R	175.9	± 0.5	15.8	2.2 (fixed)	0.5 ± 0.2
#2	181.7	± 0.4	11.5	3.4 ± 1.0	0.9 ± 0.4
#3-L	185.6	± 0.3	7.7	2.2 (fixed)	1.3 ± 0.2
#3-R	186.6	± 0.3	6.6	2.2 (fixed)	1.3 ± 0.2
#4	189.0	± 0.3	4.3	2.2 (fixed)	1.2 ± 0.3
#5	191.4	± 0.3	1.8	2.2 (fixed)	0.7 ± 0.4
#6	194.4	± 0.8	-1.2	4.0 ± 0.4	3.1 ± 0.8

Table 5.5: Results of the Gaussian fitting for ^{28}Si described in the text. The numbering of the peaks is from the ground to the excited states. The quoted errors are statistical.

the selectivity of the (π^+, K^+) reaction and the shallower Λ potential depth of about 30 MeV, the three peaks at $B_{\Lambda}=17, 8$ and -1 MeV can be interpreted as being the largest l neutron-hole Λ -particle configurations: $[0d_{5/2}^{-1}, s_{\Lambda}]$, $[0d_{5/2}^{-1}, p_{\Lambda}]$ and $[0d_{5/2}^{-1}, d_{\Lambda}]$, respectively.

The spectrum was fitted by six Gaussians and a 2nd-order polynomial standing for the continuum part with the following assumptions. Since the lowest and the third peaks are wider than the energy resolution, each peak was represented by two Gaussians. The broader peaks at $B_{\Lambda}=12$ and -1 MeV (#2 and #6) were fitted by Gaussians whose widths were free parameters. The strength at around $B_{\Lambda}=6\sim 3$ MeV (#4 and #5) was represented by two Gaussians. The results are shown in Table 5.5 and Fig.5.3-(b). The obtained ground-state binding energy ($17.4 \pm 0.5 \pm 0.5$ MeV) is larger than that obtained in the BNL experiment (16.00 ± 0.29 MeV [26]). This may be because the lowest peak is represented by two Gaussians in the present case. The cross section of the lowest peak is compared with the BNL result and a DWIA calculation [54] in Table 5.2. The present central values are slightly smaller than them.

A calculation based on a configuration-mixing shell model [21, 54, 58] is shown in Fig.5.3-(a). In the model, nuclear core wave functions are treated in a full $[0d_{5/2}^{-1}, 1s_{1/2}^{-1}, 0d_{3/2}^{-1}]$ model space. The observed three major peaks are well reproduced by the calculation. However, the observed strength at $B_{\Lambda}=12$ MeV (#2) is significantly larger than the prediction. A similar strength was observed in the BNL ^{28}Si spectrum [26].

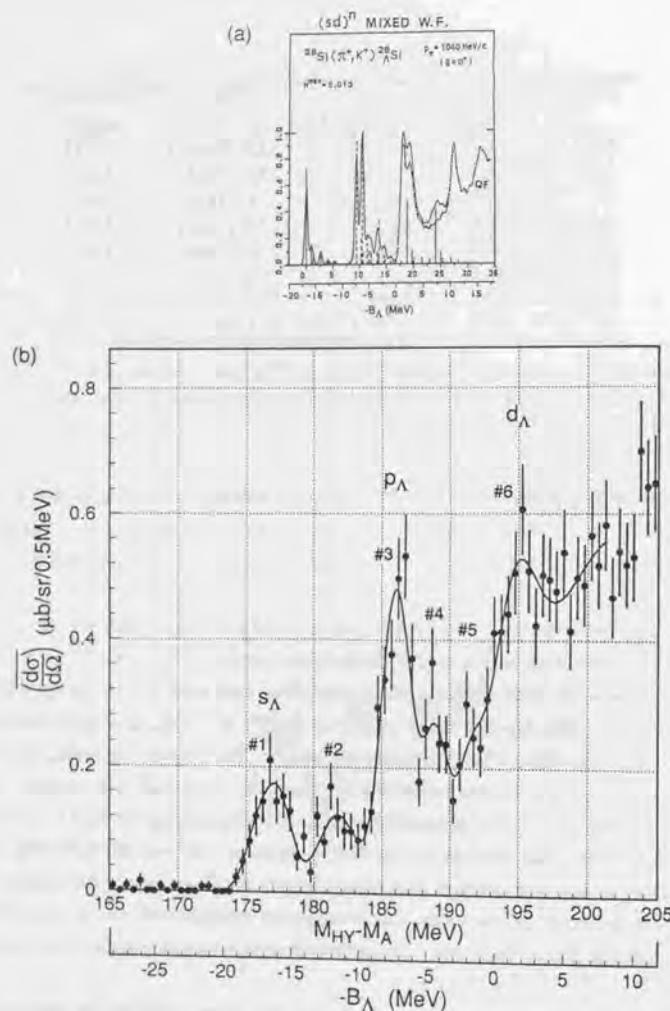


Figure 5.3: (a) Theoretical $^{28}_{\Lambda}\text{Si}$ spectrum based on a configuration-mixing shell model [21, 54, 58]. (b) The observed $^{28}_{\Lambda}\text{Si}$ spectrum with the fitting curve described in the text.

5.3 Heavy Λ hypernuclei

5.3.1 $^{89}_{\Lambda}\text{Y}$, $^{139}_{\Lambda}\text{La}$ and $^{208}_{\Lambda}\text{Pb}$

The obtained $^{89}_{\Lambda}\text{Y}$, $^{139}_{\Lambda}\text{La}$ and $^{208}_{\Lambda}\text{Pb}$ spectra show characteristic peak structure. Considering the selectivity of the (π^+, K^+) reaction, this peak structure is expected to reflect the Λ -shell structure. Major peaks possibly correspond to angular momentum stretched states which have neutron holes in the largest l orbits. The observed $^{89}_{\Lambda}\text{Y}$ spectrum shape appears to be consistent with that of the BNL (π^+, K^+) experiment [26].

Figures 5.4-(b), 5.5-(b) and 5.6-(b) show the bound regions of the $^{89}_{\Lambda}\text{Y}$, $^{139}_{\Lambda}\text{La}$ and $^{208}_{\Lambda}\text{Pb}$ spectra with marks indicating the peaks corresponding to the following major neutron-hole series: $[0g_{9/2}^{-1}, l_{\Lambda}]$, $[0h_{11/2}^{-1}, l_{\Lambda}]$ and $[0i_{13/2}^{-1}, l_{\Lambda}]$ for $^{89}_{\Lambda}\text{Y}$, $^{139}_{\Lambda}\text{La}$ and $^{208}_{\Lambda}\text{Pb}$, respectively. The correspondence was inferred from calculations using a Woods-Saxon potential [54]. We could identify peaks which could be assigned to deeply bound single-particle states, such as the s_{Λ} and p_{Λ} states. The width of these deeply bound states seems to be consistent with the experimental energy resolutions, although the spectrum, itself, is rather smooth in the case of $^{208}_{\Lambda}\text{Pb}$. This situation is quite in contrast with the nucleon case, where the nucleon deep-hole states cannot be observed as narrow peaks because of their large widths. The present results will indicate that the independent single-particle picture may be a good approximation, even in the heavy Λ hypernuclear states, as predicted.

The width of highly lying Λ orbits should also be noticed. Those states are expected to keep narrow widths, because of the absence of the Pauli blocking, relatively weak ΛN interaction, and the centrifugal barrier due to the large angular momentum [23, 21]. Although most of those highly lying states are unstable against nucleon emission, the corresponding widths were predicted to be less than 0.5 MeV at most, where the nuclear Auger effect dominates [22]. As predicted, the observed $^{89}_{\Lambda}\text{Y}$ and $^{139}_{\Lambda}\text{La}$ spectra exhibit some peak structure even in the highly excited regions, although the $^{208}_{\Lambda}\text{Pb}$ spectrum is smoother.

Theoretical spectra calculated by DWIA [20, 21, 54, 53] are shown in Figs. 5.4-(a), 5.5-(a) and 5.6-(a). They clearly demonstrate the powerful selectivity of the (π^+, K^+) reaction, where the Λ single-particle levels appear prominently. These figures were folded with an energy resolution of 2 MeV (FWHM). The calculation shows that, in addition to the major neutron-hole series, non-major neutron-hole series are also populated with considerable strength. In particular, the following

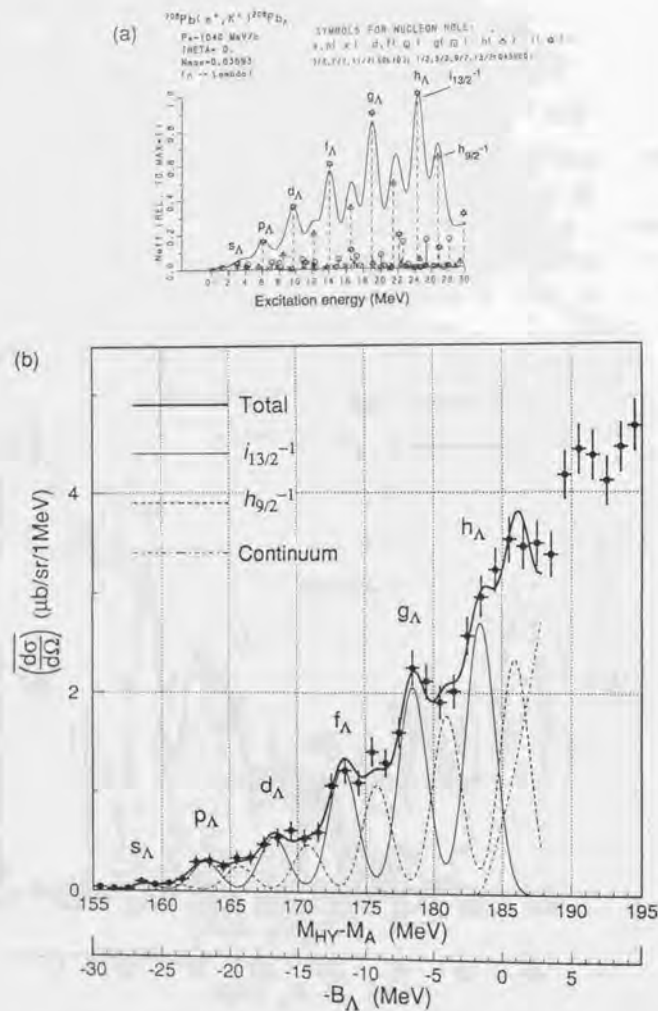


Figure 5.6: (a) Preliminary ^{208}Pb spectrum calculated by DWIA assuming a width of 2 MeV (FWHM) [20, 53]. (b) The observed ^{208}Pb spectrum with the fitting curve described in the text.

sub-major series are conspicuous: $f_{5/2}^{-1}$ and $f_{7/2}^{-1}$ for ^{89}Y , $g_{7/2}^{-1}$ and $g_{9/2}^{-1}$ for ^{139}La , $h_{9/2}^{-1}$ for ^{208}Pb . The sub-major series peaks are placed between those of the major series. Even if considering the experimental energy resolution and those non-major series strengths, the observed spectra are smoother than the calculated ones, particularly, in the case of ^{208}Pb . Since those states are expected to be narrow (as mentioned above), the smoothness may indicate that non-major neutron-hole series are populated more strongly than according to the predictions.

To obtain the binding energies of the observed major peaks, the bound regions of the spectra were fitted assuming not only the major neutron-hole series, but also the sub-major series. The major series were represented by Gaussians whose widths were fixed to be the experimental energy resolution. The sub-major series strengths were assumed to have the same spectral shapes as those of the major series, except for energy shifts and overall normalization factors. The energy shifts relative to the major series were assumed to be the energy differences of those neutron-hole states: 4.50, 10.05, 3.44, 8.92 and 2.48 MeV for $f_{5/2}^{-1}$, $f_{7/2}^{-1}$, $g_{7/2}^{-1}$, $g_{9/2}^{-1}$ and $h_{9/2}^{-1}$, respectively [53]. Although some of these assumptions may be over simplified, they are used in order to avoid depending on details of theoretical models.

The results of the fitting are shown in Table 5.6 and Figs. 5.4-(b), 5.5-(b), 5.6-(b). The fitting curves agree well with the observed spectra. It should again be noted that the assignments of the Λ single-particle states are based on calculations with a Woods-Saxon potential (as mentioned already). The quoted errors of the ^{89}Y mass for the p_Λ , d_Λ and f_Λ peaks were made larger, considering that the observed major peaks are wider than the fitting curve. The obtained ground-state cross sections are compared with the BNL result [26] and DWIA calculations [54] in Table 5.2. The present results are smaller than the calculations, while they are consistent with the BNL result for ^{89}Y . The discrepancies are larger for heavier hypernuclei.

5.4 Mass-number dependence of B_Λ

Table 5.7 summarizes the obtained binding energies of the states which were interpreted as being the Λ single-particle orbits for the major neutron-hole series. They are plotted in Fig. 5.7 as a function of the mass number compared with calculations with a Woods-Saxon potential whose depth is 30 MeV [21]. The binding energies in this table were corrected for the energy shifts due to the neutron-hole fragmentation, as mentioned in section 4.1. The mass-number dependence is well reproduced by the calculation over the entire mass-number range down to the s_Λ orbits. In

Spectra	Peaks	$M_{HY} - M_A$ (MeV)	Errors (MeV)	FWHM (MeV)	Cross sections ($\mu\text{b/sr}$)
$^{89}_{\Lambda}\text{Y}$	s_{Λ}	165.6	± 0.3	2.3(fixed)	0.6 ± 0.1
	p_{Λ}	171.8	± 0.3	2.3(fixed)	1.7 ± 0.1
	d_{Λ}	179.0	± 0.3	2.3(fixed)	3.5 ± 0.3
	f_{Λ}	186.1	± 0.2	2.3(fixed)	5.4 ± 0.4
	Ratio $(f_{5/2}^{-1}/g_{9/2}^{-1}) = 0.9 \pm 0.1$ Ratio $(f_{7/2}^{-1}/g_{9/2}^{-1}) = 1.0 \pm 0.1$				
$^{139}_{\Lambda}\text{La}$	s_{Λ}	161.3	± 1.0	2.4(fixed)	0.2 ± 0.1
	p_{Λ}	165.4	± 0.2	2.4(fixed)	1.0 ± 0.2
	d_{Λ}	171.6	± 0.2	2.4(fixed)	2.4 ± 0.3
	f_{Λ}	177.9	± 0.3	2.4(fixed)	4.3 ± 0.5
	g_{Λ}	184.3	± 0.2	2.4(fixed)	7.0 ± 0.8
	Ratio $(g_{7/2}^{-1}/h_{11/2}^{-1}) = 0.5 \pm 0.2$ Ratio $(g_{9/2}^{-1}/h_{11/2}^{-1}) = 1.5 \pm 0.3$				
$^{208}_{\Lambda}\text{Pb}$	s_{Λ}	158.7	± 0.5	2.5(fixed)	0.2 ± 0.1
	p_{Λ}	163.2	± 0.3	2.5(fixed)	0.8 ± 0.2
	d_{Λ}	168.2	± 0.4	2.5(fixed)	1.5 ± 0.2
	f_{Λ}	173.4	± 0.2	2.5(fixed)	3.3 ± 0.3
	g_{Λ}	178.5	± 0.2	2.5(fixed)	5.5 ± 0.4
	h_{Λ}	183.4	± 0.3	2.5(fixed)	7.2 ± 0.6
	Ratio $(h_{9/2}^{-1}/i_{13/2}^{-1}) = 0.9 \pm 0.1$				

Table 5.6: Results of the peak fittings for $^{89}_{\Lambda}\text{Y}$, $^{139}_{\Lambda}\text{La}$ and $^{208}_{\Lambda}\text{Pb}$. The quoted ratios are the ratios of the normalization factors. The quoted errors are statistical. The assignments of the Λ single-particle orbits are based on calculations with a Woods-Saxon potential, as described in the text.

	$B_{\Lambda}(\text{MeV})$					
	s_{Λ}	p_{Λ}	d_{Λ}	f_{Λ}	g_{Λ}	$s_{\Lambda}([26])$
$^{10}_{\Lambda}\text{B}$	8.1 ± 0.2	-	-	-	-	-
$^{12}_{\Lambda}\text{C}$	10.76 (fixed)	-0.1 ± 0.1	-	-	-	10.75 ± 0.10
$^{28}_{\Lambda}\text{Si}$	17.4 ± 0.5	7.1 ± 0.3	-1.2 ± 0.8	-	-	16.00 ± 0.29
$^{89}_{\Lambda}\text{Y}$	22.1 ± 0.3	15.8 ± 0.8	8.7 ± 1.0	1.4 ± 0.9	-	22.12 ± 1.56
$^{139}_{\Lambda}\text{La}$	24.5 ± 1.0	20.4 ± 0.2	14.3 ± 0.2	8.0 ± 0.3	1.5 ± 0.2	-
$^{208}_{\Lambda}\text{Pb}$	26.3 ± 0.5	21.9 ± 0.3	16.8 ± 0.4	11.7 ± 0.2	6.6 ± 0.2	-

Table 5.7: Obtained binding energies of the major Λ shell orbits. The quoted errors are statistical.

this respect, the present results are consistent with the independent single-particle picture of a Λ hyperon.

It was pointed out by Dover [67] that the mass-number dependence of the binding energy could be changed if the distinguishability and identity of a Λ hyperon became ambiguous in conjunction with a partial de-confinement of quarks. It would consequently be possible that the level spacing between the s_{Λ} and p_{Λ} states increases by about 2 MeV in a heavy hypernucleus, such as $^{208}_{\Lambda}\text{Pb}$. Figure 5.8 shows plot of the level spacing between the s_{Λ} and p_{Λ} states, and between the p_{Λ} and d_{Λ} states as a function of the mass number. As shown in the figures, the present results deny such a possibility.

Beyond a simple Woods-Saxon potential, a phenomenological Λ one-body potential has been developed within the framework of a Skyrme-Hartree-Fock approach [28, 29]. Successful agreement with the Λ single-particle energy data up to $A=89$ was attained with a potential depth of 28 MeV and with an effective Λ mass of 0.8-times the Λ mass. There is another approach starting from effective ΛN interaction models [30, 31]. This approach relates two-body ΛN interaction to a one-body Λ potential in a hypernucleus by the YNG interaction in the density-dependent Hartree-Fock formalism. Recent ΛN interaction models, such as the Nijmegen D (ND), F (NF), SC (NSC) and Jülich A (JA), B (JB) potentials, were adopted and compared in order to reproduce those experimental data. The present new data extend the available mass-number range, and are expected to be incorporated into further theoretical studies.

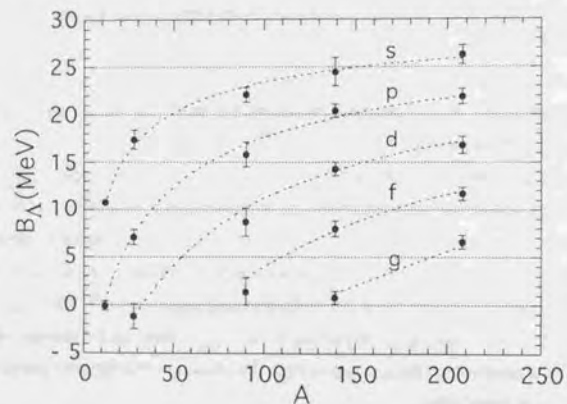


Figure 5.7: Obtained binding energies of the major Λ shell orbits as a function of the mass number. Calculations with a Woods-Saxon potential [21] are indicated by dotted lines.

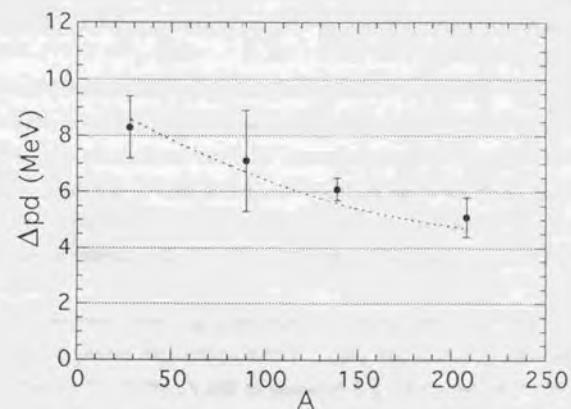
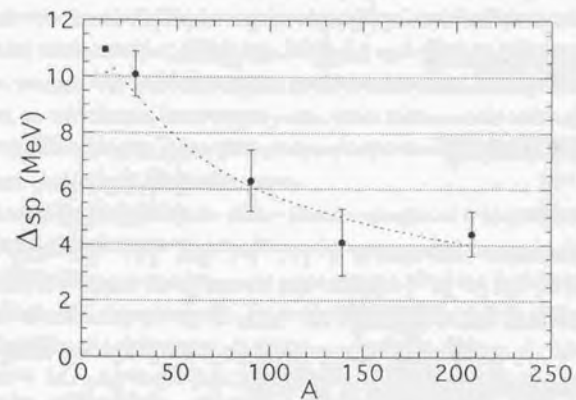


Figure 5.8: Level spacing between the s_Λ and p_Λ peaks (Δ_{sp}) and between the p_Λ and d_Λ peaks (Δ_{pd}) as a function of the mass number. Calculations with a Woods-Saxon potential [21] are indicated by dotted lines.

Chapter 6

Summary

The hypernuclear mass spectra of ${}^{10}_{\Lambda}\text{B}$, ${}^{12}_{\Lambda}\text{C}$, ${}^{28}_{\Lambda}\text{Si}$, ${}^{89}_{\Lambda}\text{Y}$, ${}^{139}_{\Lambda}\text{La}$ and ${}^{208}_{\Lambda}\text{Pb}$ were measured by the (π^+, K^+) reaction with an energy resolution of 2 MeV (FWHM). The experiment used a 1.06 GeV/c π^+ beam of the K6 beam line of KEK 12-GeV PS and the superconducting kaon spectrometer (SKS), which was newly constructed for the present experiment.

All of the measured spectra showed characteristic peak structure which reflects the selectivity of the (π^+, K^+) reaction. The binding energies of a Λ hyperon and the cross sections were obtained for observed peaks by peak fitting based on simple assumptions.

In the ${}^{12}_{\Lambda}\text{C}$ spectrum, two core-excited peaks were resolved for the first time in addition to the well-known $[0p_{3/2}^{-1}, s_{\Lambda}]$ and $[0p_{3/2}^{-1}, p_{\Lambda}]$ states, which had already been observed in previous experiments. The two small peaks can be interpreted as having configurations of an excited ${}^{11}\text{C}$ nucleus with a Λ hyperon in the s_{Λ} orbit. The obtained excitation energies and strengths were compared with calculations based on a configuration-mixing shell model with phenomenological ΛN interaction potentials.

In the ${}^{10}_{\Lambda}\text{B}$ spectrum, three core-excited peaks were resolved for the first time other than the ground-state peak. These states also belong to configurations of an excited ${}^9\text{B}$ nucleus with a Λ hyperon in the s_{Λ} orbit. The spectrum shape was compared with a preliminary configuration-mixing shell-model calculation.

The ${}^{28}_{\Lambda}\text{Si}$ spectrum exhibited three distinct peaks, which belong to configurations of $[0d_{5/2}^{-1}, s_{\Lambda}]$, $[0d_{5/2}^{-1}, p_{\Lambda}]$ and $[0d_{5/2}^{-1}, d_{\Lambda}]$. In addition to these major peaks, between the s_{Λ} and p_{Λ} peaks, the spectrum showed considerable strength, which was not predicted by a configuration-mixing shell model.

In all three cases, further theoretical studies are required in order to obtain

conclusive information about the hypernuclear structure and the ΛN interaction.

In the ${}^{89}_{\Lambda}\text{Y}$, ${}^{139}_{\Lambda}\text{La}$ and ${}^{208}_{\Lambda}\text{Pb}$ spectra, peak structure possibly reflecting the Λ shell structure was observed. This represents the first observation for ${}^{139}_{\Lambda}\text{La}$ and ${}^{208}_{\Lambda}\text{Pb}$. These peaks can be attributed to angular-momentum stretched states of Λ -particle neutron-hole configurations: $[0g_{9/2}^{-1}, l_{\Lambda}]$, $[0h_{11/2}^{-1}, l_{\Lambda}]$ and $[0i_{13/2}^{-1}, l_{\Lambda}]$, respectively. In particular, peaks which could be assigned to the ground states were identified. It was found that, in addition to those major series, other neutron-hole series contributed significantly. The obtained cross sections were smaller than those obtained by DWIA calculations, particularly for heavier cases.

The mass-number dependence of the binding energies of Λ single-particle states was well reproduced with a simple Woods-Saxon potential having a depth of 30 MeV over the wide mass-number range up to 208 for all of the Λ shell orbits down to s_{Λ} . This result is consistent with the independent single-particle picture and the distinguishability of a Λ hyperon.

Acknowledgements

First of all, I would like to thank my supervisor, Prof. O. Hashimoto. I have been able to study physics further, because he accepted me as a graduate student five years ago and gave me an opportunity to participate in the present experiment. I could not imagine how much he has been troubled by me, and how much he has made efforts to assist me in studying physics, carrying out experiments, and completing the present work. I have always been feeling a certain peace of mind because I could believe that he has guided me as a physicist.

I am deeply grateful to Dr. T. Nagae. He has been one of the closest seniors of mine since I entered graduate school. He has been sincerely concerned about me, and have given me countless pieces of advice while studying experimental techniques and physics. We have spent much time together for chattering, discussions, lunch and dinner, and so on.

I also express my special thanks to Ms. M. Sekimoto. Her contributions to the experiment are greatly appreciated, although sometimes they were not likely to be conspicuous. Furthermore, she has given our group a warm and comfortable atmosphere. It was also a great pleasure to enjoy delicious food prepared by her.

I must express appreciation to Prof. S. Homma. He is the head of the INS intermediate energy physics division to which I belong, and gave me invaluable advice. I remember his first advice was that we should never trust a rumor about another person.

I am indebted to Profs. T. Fukuda, T. Kishimoto, K. Maeda, H. Sakaguchi, and T. Shibata, who were important collaborators in the present experiment, and who gave me various comments and advice not only concerning the experiment, but also about physics.

I express my thanks to Mr. T. Takahashi. He is another graduate student who took part in our group from an early stage of the experiment, and who contributed to the data-acquisition system. I also thank Ms. K. Aoki, one of three members who tried to complete doctor theses through SKS experiments. Her career as a company worker for a few years was very interesting to me and brought fresh air to our group. I express my appreciation to Dr. H. Noumi, being impressed by his tireless efforts to assist graduate students. I also thank Mr. S. Ajimura and Mr. A. Ohkusu, who were not only indispensable young workers, but also important friends.

I am indebted to Prof. H. Bhang. He stayed at KEK for more than a half

year as a collaborator of the present experiment, and contributed a great deal to the experiment. Our group was greatly supported by his existence. I express my thanks to Mr. H. Yu and Mr. H. Park. They were important workers in the present experiment during the preparation stage. I have learned many interesting cultural differences between Japan and Korea from discussions with them. I was impressed by their innocent, patient attitude and efforts to try to absorb everything as much as possible. I would like to acknowledge Dr. M. Youn for his careful and detailed proofreading of this manuscript. He was one of the closest foreigners to me and gave me much advice about writing in English.

I also express my thanks to other foreign collaborators: Prof. R. P. Redwine, Prof. R. Sawafu and Prof. Y. Gavrilov. They not only helped with the experiment, but also gave our group an international atmosphere, from which I could learn various things other than English.

I would like to express my appreciation to the KEK staff, without whom the present experiment could not have been carried out: the circuit group comprising Prof. T. K. Ohsaka, Dr. O. Sasaki and others; the online group comprising Prof. K. Fujii, Dr. H. Kodama, Dr. M. Noumachi, Dr. Y. Yasu and others; the beam channel group comprising Prof. M. Takasaki, Prof. Y. Suzuki, Dr. K. H. Tanaka, Dr. M. Ieiri, Mr. Y. Yamanoi and others; the machinery center staff comprising Mr. Y. Sakakibara and others; the refrigerator group comprising Prof. T. Shintomi, Prof. Y. Doi, Mr. Y. Kondo, Mr. Y. Makita and others; the PS accelerator group; the physics office staff; and the PS executive staff comprising Prof. K. Nakai, Prof. T. Ohshima, Prof. K. Takamatsu and others. I feel very sorry that I could not list all of the staff members who supported the present experiment.

I am deeply grateful to Prof. T. Motoba and Prof. K. Itonaga for invaluable discussions concerning the physics of the experimental results. In particular, I would like to thank Prof. T. Motoba for commenting on the manuscript.

I also express my gratitude to the INS staff members, who have provided a characteristic friendly, warm and kind atmosphere, which has relaxed me very much. I learned from Dr. H. Hamagaki the importance of adopting new and challenging technology in spite of some unavoidable risks of failure. Mr. Y. Matsuyama is an expert of wire chambers, and designed the beam drift chambers. Mr. K. Omata is an expert of data-acquisition systems. His data-acquisition program for a personal computer has been very useful. Dr. T. Miyachi contributed a great deal to the field measurement. Mr. T. Morimoto is a member of the INS machinery center and

gave me invaluable advice about engineering work. Mr. T. Kitami took charge of the small refrigerator of the SKS magnet. Dr. Y. Fujita gave me friendly greetings any time. Mr. Y. Kakiguchi is one of a few staff members of the same generation and a good friend. I am indebted to the secretary of the INS branch at KEK, Ms. Y. Iwamoto, for various office procedures.

I would like to thank Dr. H. Tamura, Dr. H. Outa, Dr. M. Aoki, and the other members of the troidal and T-violation groups, who were important seniors or friends of mine and have been showing me warm and kind friendship. I express my gratitude to Dr. H. Enyo for giving me much advice concerning experimental techniques. I was very much impressed by his excellent cleverness regarding both experiments and physics as well as his talent to attract students. I thank Dr. A. Higashi, who was one of the closest seniors of mine at INS during graduate-school days. I also express my appreciation to Prof. C. Rangacharyulu for his kind proofreading of this manuscript.

I acknowledge the referees of the present thesis, Prof. R. Hayano, Prof. M. Ishihara, Prof. T. Nomura, Prof. S. Yamada and Prof. T. Yamazaki, for giving me invaluable advice and comments. In particular, I express my special thanks to the chief referee, Prof. R. Hayano, who made a considerable effort to assist me in completing the present thesis.

Finally, I want to dedicate this thesis to my parents, Tomoyo and Hiroshi Hasegawa, to my brother's family, Hiroaki, Teruko, Kazuhiro and Kaori Hasegawa, and to my sister's family, Yumiko, Kouji and Risa Hashimoto, who have been supporting me not only financially, but also mentally.

Appendix A

Magnetic field measurement of SKS

A.1 Introduction

The superconducting kaon spectrometer (SKS) features a good momentum resolution of about 0.1%(FWHM) and a large angular acceptance of 100 msr in the 1-GeV/c momentum range. To realize these specifications, the spectrometer adopted a large powerful sector-shape dipole magnet. The momentum is determined by reconstructing particle tracks with the Runge-Kutta method using a measured magnetic field map. By a Monte-Carlo simulation (appendix B), the precision of the magnetic field map was shown to be the most important factor limiting the momentum resolution. It was shown that the probe positions, orientation and calibration parameters should be typically measured with precisions of 0.5 mm, 3 mrad and 0.03%, respectively.

A.2 Apparatus

Volume-scanning device

A large volume of 6 m³ must be covered in the field measurement, since there is considerable fringing field due to saturation and a large aperture of 1.5^W × 0.5^H m². To scan the large volume automatically, a large-scale volume-scanning device (Fig.A.1) was constructed. The principal components are made of aluminum. Hall probes were fitted on a small holder which moved along the z-beam. The z-beam, itself, moved on two x-beams. The x-beams were supported by four vertical rails and screws. Although the 6-m z-beam bent by about 1.5 mm at the center, z rails were fitted on the z-beam so that they should be straight and horizontal within

Sensitive size	$0.5 \times 1.0 \text{ mm}^2$
Maximum field	3.0 T
Precision	0.02% (25°)
Temperature stability	$\pm 0.01\%$ ($^{\circ}\text{C}$)
Long-term stability	$\pm 0.1\%$ (1 year)

Table A.1: Specifications of the Hall probes, *GMW DTM-141-S*.

$\pm 0.2 \text{ mm}$. Similarly, x and y rails were fitted so that they should be horizontal or vertical within $\pm 0.2 \text{ mm}$. On the z -beam, the x -beams and two of the four y -beams, optical linear scales with a resolution of 0.1 mm were attached for probe-position measurements.

These were driven by pulse motors with lubber timing belts in the z and x directions, or with gears and screws in the y direction. A rotary encoder was set for each pulse motor in order to monitor the rough movement. In order to limit the movement for safety purposes, micro switches were fitted at the ends of the rails; they could electrically cut the pulse-motor DC-power lines forcibly.

To avoid thermal expansion and contraction of the structure, the room temperature was kept at $22^{\circ} \pm 2^{\circ}$. The central magnetic field was monitored with an NMR probe to correct its fluctuation, which was found to be less than 0.01% .

Hall probes

High-precision Hall probes (*GMW Group 3 DTM-141-S*¹) were employed as field-measuring sensors. Specifications are given in Table A.1. Although the probes were calibrated by the company, they were also calibrated by us with an NMR probe (as described in section A.4). The temperature dependence was automatically compensated by a temperature sensor fitted on each probe.

Two sets of three Hall probes were mounted on the top and bottom of an aluminum bar, as shown in Fig.A.2. The probe positions relative to the bar were precisely measured, where the machining precisions of the bar were better than $\pm 20 \mu\text{m}$ and $\pm 1 \text{ mrad}$. The bar was fitted on the probe holder vertically with a precision of 1 mrad . The position and the phase angle of the bar relative to the magnet were measured with a scale having precisions of 0.2 mm and 2 mrad , respectively, by refer-

¹Group 3 Technology Ltd., 2 Charann Place, Avondale, Auckland 7, New Zealand, P.O.Box 71-11.

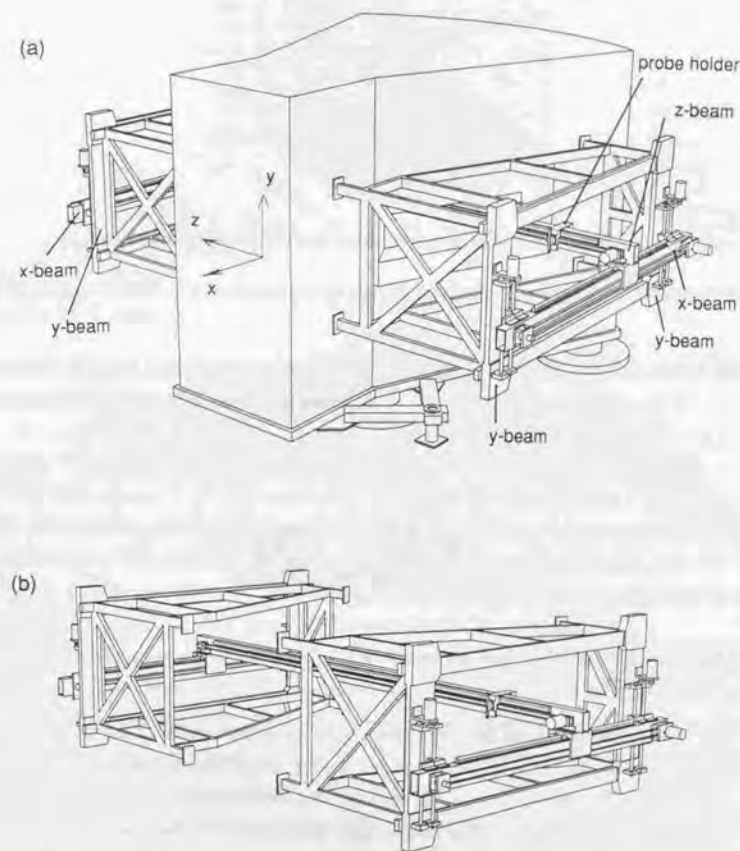


Figure A.1: Schematic views of the volume-scanning device (a) with and (b) without the magnet.

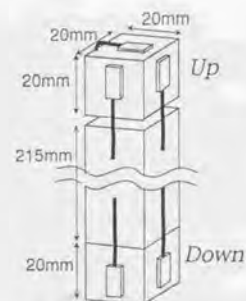


Figure A.2: Schematic view of the Hall-probe mount bar.

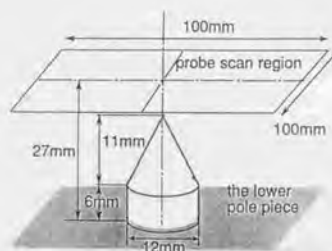


Figure A.3: Schematic view of the pin on the lower pole piece used for probe-position measurements.

ring to precise marks on the lower pole piece. As a cross check of the probe-position measurement, the probes were scanned over a small pin on the lower pole piece, (Fig.A.3). By fitting, the probe position was determined with a precision of 0.3 mm, as shown in Fig.A.4. The results were consistent with the direct measurements with a scale.

Control by a personal computer

The entire system was controlled by a personal computer (NEC-PC9801 or EPSON-PC286). The Hall probes, pulse motors, rotary encoders and optical linear scales were handled through RS232C ports. The NMR probe and a digital voltage meter

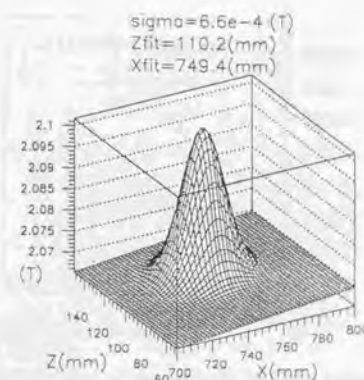


Figure A.4: Result of a probe scan over a small pin for a probe-position measurement in the 2.2 T mode.

used to monitor the magnet current were connected to a GPIB port. Measured data were recorded on an optical magnetic disk.

A.3 Field measurement

To cover a wide momentum range from 0.5 to 1.1 GeV/c, the magnetic field was measured for the following six excitations: 3.0, 2.7, 2.4, 2.2, 1.9, 1.7 and 1.5 T modes. In the measurement, the total volume was divided into ten subregions, in which the excitations were changed downward for each subregion.

The scanning firstly proceeded in the z -direction, secondly in the x -direction, and lastly in the y -direction. The step-size was typically 2 cm. The scanning speed in the z -direction was typically 2 sec per point, which was determined so as to wait for the dumping of mechanical vibration. The measurement took about one month in total, except for the Hall-probe calibration.

Probe-position measurements with the small pin were carried out during the field measurement, once in a few hours in each subregion, when possible. As a result, no systematic shifts were detected.

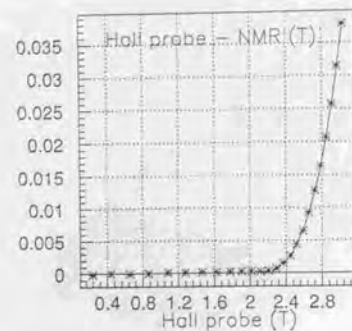


Figure A.5: Typical result of the Hall-probe normal-component calibration.

A.4 Hall-probe calibration

Normal-component calibration

The Hall probes were calibrated about the normal component with an NMR probe. Figure A.5 shows a typical result of the normal-component calibration. The calibration curve rises above 2 T because the company's calibration was only for below 2 T. The normal-component calibration was performed four times during the field measurement for all of the probes. No significant drift was observed.

Hall planar effect calibration

The Hall planar effect can be represented by the following relation [68]:

$$B_{\text{measured}} = B_3 + 2p_H B_1 B_2, \quad (\text{A.1})$$

where B_1 , B_2 and B_3 are the field components in the Hall-probe local coordinate system (Fig.A.6); B_{measured} is the measured field; p_H is the Hall planar coefficient. The calibration was carried out for each probe at four field values in the SKS magnet: 1.5, 2.2, 2.5 and 3.0 T. For the calibration, a special probe rotation device with which the orientation of the rotation axis and the rotation angle could be measured with a precision of 2 mrad was prepared. In the calibration, a Hall probe was rotated with the rotation axis being vertical to the magnetic field. Figure A.7 shows a typical result of the calibration and a fitting function, which is a superposition of $\sin \theta$ and $\sin 2\theta$ with different phase offsets. Figure A.8 shows typical measured B dependence of the Hall planar coefficient.

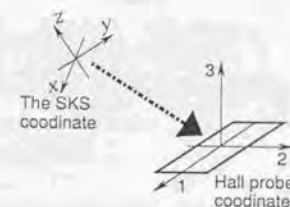


Figure A.6: Definition of the Hall-probe local coordinate system.

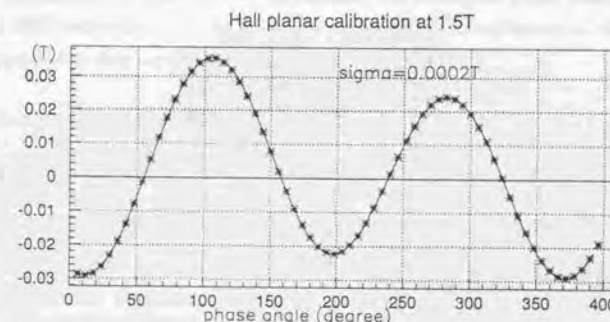


Figure A.7: Typical result of the Hall planar effect calibration at 1.5 T. The symbols and the solid line are data and a fitting curve, respectively.

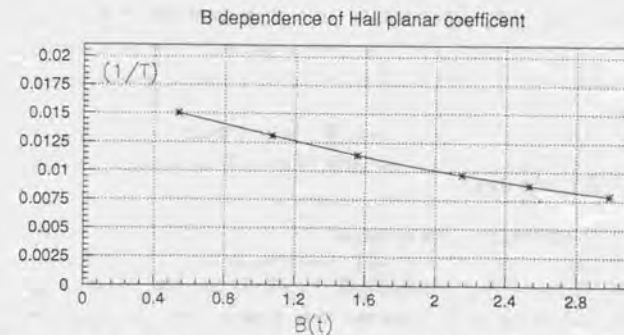


Figure A.8: Typical measured B dependence of the Hall planar coefficient.

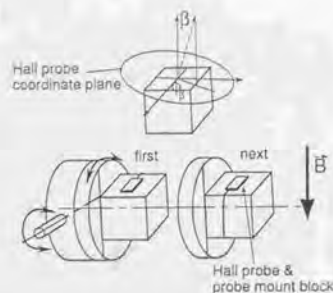


Figure A.9: Procedure of the Hall-probe orientation measurement.

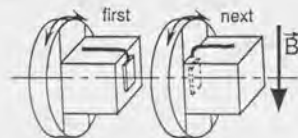


Figure A.10: Procedure of the Hall-probe phase measurement.

Orientation of the Hall probes

The orientation of the Hall probes relative to the prove-mount bar was measured with the probe rotation device, as shown in Fig.A.9. First, two independent angles were scanned in order to find the maximum of the field; then, after the cube was rotated 180° , they were scanned again. From these measurements, β and ϕ_β defined in the figure were obtained. The Hall-probe phase angle relative to the prove-mount bar was measured with the rotation device by a similar procedure, as shown in Fig.A.10.

A.5 Analysis

A.5.1 Field reconstruction

The measured field data were interpolated by the third-order Spline method in order to obtain field values at 2-cm normal-mesh points. Then, the magnetic field was reconstructed point by point using Eq.(A.1). The Hall-probe local coordinate system

is related to the magnet coordinate system by a rotation matrix which is determined by the probe orientation parameters.

A.5.2 Internal consistency

In order to check the measured magnetic field data, their internal consistency was examined by the following three methods.

Overlap region

The total volume was scanned with two sets of three Hall probes. There were therefore several overlapping regions where the magnetic field was measured in duplicate by different probes, or as different subregions. Those magnetic field data were compared with each other in order to examine the internal consistency of the data. It was found that they agreed reasonably well.

Surface-to-volume calculation

The magnetic field at an arbitrary point in a volume can be calculated using the magnetic field at the surface of the volume. In fact, there is a good algorithm to perform this calculation (the surface-to-volume calculation) [69]. In the calculation, the magnetic field is represented as an expansion of trigonometric and hypertrigonometric functions; the coefficients should be determined from the surface magnetic field. A program for the surface-to-volume calculation was made by ourselves and used for examining the internal consistency of the data. Figure A.11 shows a distribution of the difference between the measured magnetic field in the 2.2 T mode and the surface-to-volume calculation. The distribution is sufficiently narrow.

Divergence of \vec{B}

The real magnetic field satisfies $\nabla \cdot \vec{B} = 0$. This relation was used to check the internal consistency of the data. This check is important because the three independent field components are related by this relation. Figure A.12 shows a $\nabla \cdot \vec{B}$ distribution for the 2.2 T mode together with that for a Helmholtz coil having a diameter and distance of 100 and 70 cm, respectively. The Helmholtz-coil size parameters were chosen so as to simulate the SKS field. The result is consistent with the required precision.

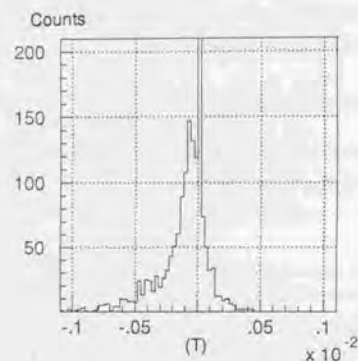


Figure A.11: Distribution of the difference between the measured magnetic fields for the 2.2 T mode and surface-to-volume calculations.

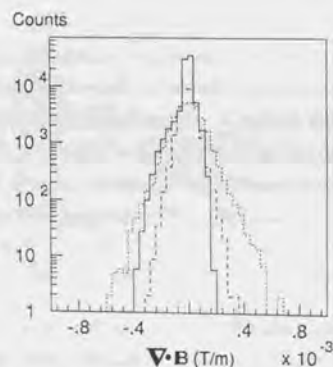


Figure A.12: Distributions of $\nabla \cdot \vec{B}$ for the measured magnetic field for the 2.2 T mode and Monte-Carlo calculations for the Helmholtz coil, assuming precisions of $\sigma=0.02\%$ (dashed line) and $\sigma=0.04\%$ (dotted line).

A.5.3 Field subroutines

Two kinds of field subroutines were prepared. One is based on a simple linear interpolation algorithm, in which the field values at a point are linearly interpolated from those of the nearest-eight mesh points.

The other uses a Chebyshev polynomial expansion,

$$\vec{B}(x, y, z) = \sum_{i=0}^{imax} \sum_{j=0}^{jmax} \sum_{k=0}^{kmax} \vec{C}_{i,j,k,iregion} T_i(x') T_j(y') T_k(z'), \quad (A.2)$$

where *iregion* specifies a subregion; $T_i(x')$, $T_j(y')$ and $T_k(z')$ are Chebyshev polynomials; x' , y' and z' are normalized coordinates ($-1 < x', y', z' < 1$). The coefficients of the expansion ($\vec{C}_{i,j,k,iregion}$) were determined by the orthogonality relations,

$$\sum_{\alpha=1}^{N_\alpha} T_i(x_\alpha) T_l(x_\alpha) = \delta_{i,l} \frac{N_\alpha}{2^{1-\delta_{i,0}}} \quad (A.3)$$

$$x_\alpha \equiv \cos \frac{(\alpha - 0.5)\pi}{N_\alpha}, \quad (A.4)$$

where x_α are the zero points of the Chebyshev polynomials; N_α are integers larger than *imax*, *jmax* and *kmax*. In general, when a function can be sampled at arbitrary points, the Chebyshev polynomials are better than the trigonometric functions, since there is no boundary-condition problem [70]. There is an empirical rule used to minimize the computer space-time product: the interval over which a function is to be defined should be divided into so many subintervals that per interval about $-\ln E$ terms are needed to obtain a relative precision E [70]. In the present case, the number of terms was set to be about six, so that the total region had to be divided into 282 subregions.

Although the former method requires a much larger data size compared to the latter method, the former subroutine is faster than the latter. On a workstation (HP720), it takes about 0.03 msec and 0.5 msec to calculate three components at one position with the linear-interpolation version and the Chebyshev expansion version, respectively. In the present analysis, the linear-interpolation version with 2-cm normal-mesh data was used.

A.6 Summary

The magnetic field of the SKS large sector-shape dipole magnet was measured with high-precision Hall probes over a large volume of 6 m^3 . The whole volume was automatically scanned under the control of a personal computer. The probe position and orientation were measured with precisions of 0.5 mm and 3 mrad, respectively. The Hall probes were calibrated about the normal component and the Hall planar effect with a precision of 0.03% in total. The internal consistency of the data was examined by three methods. It was found that the data were consistent with the required precision.

Appendix B

Monte-Carlo simulation of the SKS momentum resolution

The following three factors limit the momentum resolution of SKS: multiple scattering by the drift chambers and the He bags, the drift-chamber resolution, and the precision of the measured magnetic field map. In this appendix, these three effects are estimated by a Monte-Carlo simulation. In the simulation, a uniform angular distribution covering the whole spectrometer acceptance and a momentum of 0.72 GeV/c were assumed.

Figure B.1 is a plot of the momentum resolution as a function of the drift-chamber resolution for four cases of multiple-scattering materials. It shows that He bags are definitely required. Assuming $\sigma=300\mu\text{m}$ for the drift-chamber resolution, the momentum resolution is about 0.55 MeV/c (FWHM).

Table B.1 shows the momentum resolution for four typical cases of the magnetic-field measurement precision. Since *case-2* or *case-3* may be similar to the actual situation, the momentum resolution is 0.69~0.90 MeV/c (FWHM).

Cases	Measurement precision			Momentum resolution (FWHM)
	Probe position	Probe orientation	Probe calibration	
<i>case-1</i>	0.2 mm	0.5 mrad	0.01%	0.34 MeV/c
<i>case-2</i>	0.5 mm	1.0 mrad	0.01%	0.69 MeV/c
<i>case-3</i>	0.5 mm	3.0 mrad	0.03%	0.90 MeV/c
<i>case-4</i>	1.0 mm	2.0 mrad	0.02%	0.98 MeV/c

Table B.1: SKS momentum resolution for four typical cases of the magnetic-field measurement precision.

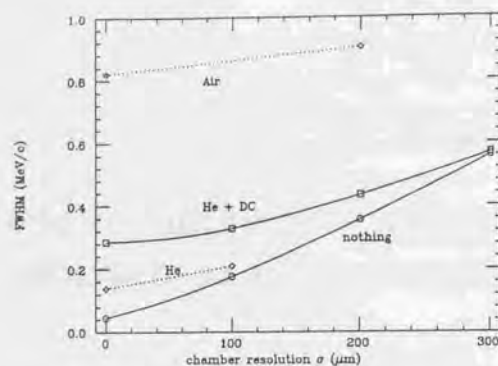


Figure B.1: SKS momentum resolution as a function of the drift-chamber resolution. The lines named (a) "nothing", (b) "He + DC", (c) "He" and (d) "Air" are (a) without multiple scattering, (b) with multiple scattering by He bags and drift chambers, (c) only by He bags, and (d) by air instead of He bags and drift chambers, respectively.

Thus, the precision of the magnetic field map is the most important factor that limits the momentum resolution. In total, the momentum resolution amounts to $0.88 \sim 1.10 \text{ MeV/c}$ ($0.12 \sim 0.15\%$) (FWHM). This result is consistent with the measured momentum resolution (Fig. 3.3), where the FWHM is about $2.04 \text{ MeV} = \sqrt{2} \times 0.136\%$ for a $1.06 \text{ GeV/c } \pi$ beam.

Appendix C

Beam momentum correction

To achieve the required momentum resolution of 0.1% (FWHM), the beam momentum calculated with a 3rd-order *Orbit* transfer matrix needs a correction, as mentioned in section 3.2. The correction terms were calibrated using SKS. For the calibration, a $1.06 \text{ GeV/c } \pi$ beam was led through the two spectrometers, QQDQQ and SKS, in the 3.0 T mode. Then, the momentum difference was represented as a function of eight measured variables: the horizontal and vertical coordinates and angles at the entrance and exit of QQDQQ. The functional form was determined by a general-purpose fitting program, *Erika* [71].

The program *Erika* determines the coefficients of a Chebyshev expansion when a *parameter* is to be represented as a function of some *variables*. In the present case, the *parameter* and the *variables* are the momentum difference and the eight variables mentioned above, respectively. A special feature of *Erika* is that it does not use the *variables* as the arguments of the Chebyshev polynomial directly, but rather uses linear combinations of the *variables*. This linear transformation is determined by a principal-component analysis [71, 72], in which correlations between the *variables* are examined. Consequently, the convergence of the expansion series can be much better.

Figure 3.3 shows the momentum resolutions before and after the *Erika* correction for a $1.06 \text{ GeV/c } \pi^+$ beam.

Appendix D

Acceptance of SKS

In this appendix, the angular acceptance of SKS is estimated by Monte-Carlo calculation. In the calculation, the beam profile was assumed to be a realistic Gaussian distribution with $\sigma = 6.0$ and 7.5 mm in the horizontal and vertical directions, respectively.

Figure D.1 shows the differential angular acceptance, $\int d\phi$, as a function of $\cos\theta$, where θ and ϕ are for a polar coordinate system defined along the central trajectory of SKS at the target. Figure D.2 shows the differential angular acceptance, $\int d(\cos\theta)$, as a function of ϕ . The area under a line corresponds to the integrated angular acceptance, $d\Omega = \int d\phi d(\cos\theta)$. The integrated acceptance is shown in Fig.D.4 as a function of the momentum as the dotted line. Note that $d\Omega$ does not include sufficient information for specifying the spectrometer angular acceptance.

The angle in the above estimation is the incident angle relative to the central trajectory. However, the acceptance should be estimated for the scattering angle of the reaction. With taking account of realistic incident-beam angle distributions (Fig.D.3), the integrated angular acceptance for the scattering angle was calculated, and is shown in Fig.D.4 as the solid line.

$\int d\phi$ V.S. $\cos\theta$

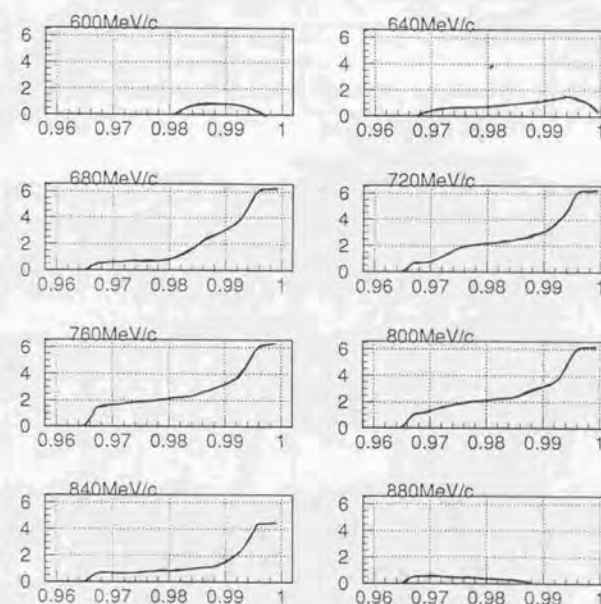


Figure D.1: Differential angular acceptance, $\int d\phi$, as a function of $\cos\theta$ for the 2.2 T mode. The area under a line corresponds to the integrated angular acceptance ($d\Omega$).

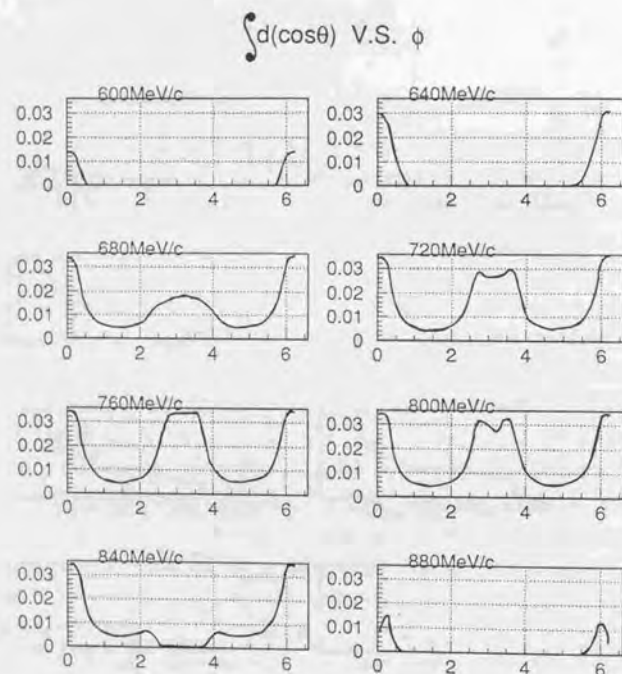


Figure D.2: Differential angular acceptance, $\int d(\cos\theta)$, as a function of ϕ for the 2.2 T mode. The area under a line corresponds to the integrated angular acceptance ($d\Omega$).

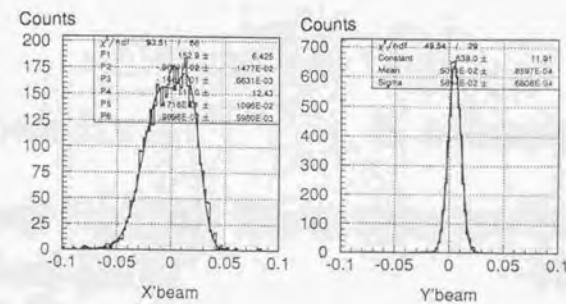


Figure D.3: Distributions of x' and y' at the target measured for a 1.06 GeV/c π^+ beam.

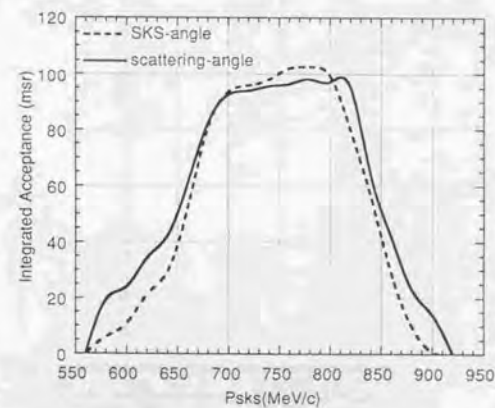


Figure D.4: Integrated angular acceptance of SKS as a function of the momentum in the 2.2 T mode. The dotted line is for the incident angle to the central trajectory of SKS. The solid line is for the scattering angle of the reaction when taking account of the measured beam angular distributions.

Appendix E

Binding energy of the $^{12}_{\Lambda}\text{C}$ ground state

Table E shows the binding energies of the $^{12}_{\Lambda}\text{C}$ ground state obtained in other experiments. On the basis of these experimental data, the binding energy is assumed to be 10.76 MeV in the momentum scale calibration (sections 3.7).

Experiments	$^{12}_{\Lambda}\text{C}$ g.s. $B_{\Lambda}(\text{MeV})$
Emulsion [5]	10.76 ± 0.19
inflight (K^{-}, π^{-}) [10]	11
inflight (K^{-}, π^{-}) [73]	10.79 ± 0.11
(stopped K^{-}, π^{-}) [14]	11
(π^{+}, K^{+}) [26]	10.75 ± 0.10
(π^{+}, K^{+}) [27]	11

Table E.1: Binding energies of the $^{12}_{\Lambda}\text{C}$ ground state obtained in other experiments.

Appendix F

Hypernuclear mass spectra as tables

The hypernuclear mass spectra shown in Figs.4.1, 4.2, 4.3, 4.4, 4.5, and 4.6 are presented as tables in Tables F.1, F.2, F.3, F.4, F.5 and F.6, respectively. The quoted values of $M_{HY} - M_A$ are the centers of the bins.

$M_{HY} - M_A$ (MeV)	Counts (/0.5MeV)	$\left(\frac{d\sigma}{d\Omega}\right)$ ($\mu\text{b}/\text{sr}/0.5\text{MeV}$)
160.25	0	.000
160.75	0	.000
161.25	1	.009
161.75	0	.000
162.25	0	.000
162.75	0	.000
163.25	0	.000
163.75	0	.000
164.25	1	.010
164.75	0	.000
165.25	0	.000
165.75	0	.000
166.25	0	.011
166.75	1	.009
167.25	1	.010
167.75	0	.000
168.25	1	.010
168.75	0	.000
169.25	1	.009
169.75	1	.007
170.25	1	.009
170.75	1	.009
171.25	0	.000
171.75	0	.000
172.25	0	.000
172.75	0	.000
173.25	0	.000
173.75	0	.000
174.25	2	.024
174.75	2	.016
175.25	1	.009
175.75	1	.007
176.25	1	.008
176.75	0	.000
177.25	0	.000
177.75	3	.026
178.25	2	.018
178.75	1	.009
179.25	1	.007
179.75	0	.000
180.25	0	.000
180.75	3	.038
181.25	4	.045
181.75	5	.054
182.25	26	.237
182.75	51	.433
183.25	121	1.057
183.75	204	1.806
184.25	204	1.797
184.75	129	1.125
185.25	91	.815
185.75	41	.364
186.25	53	.496
186.75	42	.385
187.25	44	.398
187.75	18	.171
188.25	12	.109
188.75	12	.112
189.25	13	.135
189.75	27	.244
190.25	31	.276
190.75	34	.301
191.25	28	.246
191.75	30	.273
192.25	33	.304
192.75	38	.344
193.25	82	.735
193.75	106	.964
194.25	172	1.559
194.75	194	1.782
195.25	192	1.737
195.75	176	1.588
196.25	114	1.043
196.75	82	.751
197.25	77	.727
197.75	68	.632
198.25	81	.754
198.75	81	.758
199.25	86	.778
199.75	104	1.001
200.25	102	.934
200.75	91	.856
201.25	124	1.174
201.75	102	.963
202.25	118	1.111
202.75	125	1.146
203.25	104	.988
203.75	101	.972
204.25	123	1.194
204.75	114	1.112
205.25	149	1.439
205.75	138	1.327
206.25	132	1.296
206.75	132	1.265
207.25	124	1.234
207.75	140	1.359
208.25	133	1.307
208.75	123	1.226
209.25	150	1.489
209.75	124	1.223

Table F.1: ^{12}C spectrum as a table.
123

$M_{HY} - M_A$ (MeV)	Counts (/0.5MeV)	$\left(\frac{d\sigma}{d\Omega}\right)$ ($\mu\text{b}/\text{sr}/0.5\text{MeV}$)
160.25	0	.000
160.75	0	.000
161.25	0	.000
161.75	1	.007
162.25	0	.000
162.75	0	.000
163.25	0	.000
163.75	1	.007
164.25	1	.006
164.75	2	.006
165.25	0	.000
165.75	0	.000
166.25	0	.000
166.75	2	.014
167.25	0	.000
167.75	0	.000
168.25	0	.000
168.75	0	.021
169.25	0	.030
169.75	1	.007
170.25	0	.000
170.75	0	.007
171.25	1	.007
171.75	1	.007
172.25	1	.007
172.75	0	.000
173.25	2	.021
173.75	2	.014
174.25	7	.049
174.75	8	.055
175.25	28	.197
175.75	44	.332
176.25	48	.351
176.75	58	.403
177.25	58	.401
177.75	38	.264
178.25	62	.428
178.75	73	.502
179.25	53	.367
179.75	39	.269
180.25	33	.230
180.75	21	.148
181.25	24	.181
181.75	36	.280
182.25	68	.470
182.75	79	.559
183.25	75	.523
183.75	74	.517
184.25	69	.482
184.75	72	.509
185.25	99	.704
185.75	91	.639
186.25	104	.739
186.75	95	.670
187.25	103	.728
187.75	74	.523
188.25	82	.494
188.75	69	.586
189.25	68	.488
189.75	64	.467
190.25	79	.569
190.75	75	.538
191.25	81	.583
191.75	74	.525
192.25	88	.632
192.75	82	.589
193.25	96	.695
193.75	114	.832
194.25	110	.816
194.75	118	.866
195.25	116	.853
195.75	135	.989
196.25	135	.983
196.75	121	.960
197.25	134	.988
197.75	148	1.094
198.25	120	.901
198.75	144	1.082
199.25	138	1.035
199.75	126	.937
200.25	156	1.167
200.75	144	1.086
201.25	162	1.227
201.75	188	1.257
202.25	147	1.123
202.75	161	1.224
203.25	142	1.094
203.75	160	1.220
204.25	154	1.193
204.75	169	1.294
205.25	171	1.334
205.75	172	1.351
206.25	171	1.368
206.75	158	1.250
207.25	177	1.394
207.75	167	1.328
208.25	186	1.465
208.75	173	1.378
209.25	199	1.455
209.75	176	1.408

Table F.2: ^{10}B spectrum as a table.
124

$M_{HY} - M_A$ (MeV)	Counts (/0.5MeV)	$\left(\frac{d\sigma}{d\Omega}\right)$ ($\mu\text{b}/\text{sr}/0.5\text{MeV}$)
160.25	0	.000
160.75	1	.008
161.25	0	.000
161.75	1	.008
162.25	0	.000
162.75	1	.008
163.25	1	.008
163.75	0	.000
164.25	1	.008
164.75	0	.000
165.25	1	.008
165.75	0	.000
166.25	0	.000
166.75	0	.000
167.25	2	.015
167.75	0	.000
168.25	0	.000
168.75	1	.008
169.25	0	.000
169.75	1	.008
170.25	0	.000
170.75	0	.000
171.25	0	.000
171.75	1	.008
172.25	1	.008
172.75	0	.000
173.25	0	.000
173.75	0	.000
174.25	0	.000
174.75	6	.048
175.25	10	.081
175.75	12	.096
176.25	18	.144
176.75	26	.210
177.25	18	.144
177.75	19	.153
178.25	16	.129
178.75	7	.057
179.25	11	.089
179.75	4	.033
180.25	15	.121
180.75	10	.081
181.25	21	.169
181.75	15	.120
182.25	12	.099
182.75	12	.096
183.25	10	.084
183.75	13	.106
184.25	16	.129
184.75	36	.294
185.25	41	.337
185.75	44	.377
186.25	61	.497
186.75	63	.513
187.25	43	.370
187.75	22	.178
188.25	32	.262
188.75	44	.364
189.25	29	.239
189.75	29	.237
190.25	18	.149
190.75	25	.204
191.25	36	.300
191.75	30	.248
192.25	28	.233
192.75	37	.307
193.25	50	.411
193.75	50	.414
194.25	53	.442
194.75	61	.507
195.25	72	.607
195.75	62	.510
196.25	52	.425
196.75	60	.503
197.25	58	.476
197.75	57	.478
198.25	63	.538
198.75	43	.358
199.25	59	.415
199.75	58	.490
200.25	66	.548
200.75	60	.518
201.25	68	.582
201.75	55	.468
202.25	63	.540
202.75	61	.519
203.25	61	.532
203.75	80	.699
204.25	74	.647
204.75	75	.662
205.25	82	.720
205.75	70	.601
206.25	69	.609
206.75	83	.745
207.25	87	.773
207.75	79	.696
208.25	73	.644
208.75	83	.732
209.25	84	.772
209.75	79	.704

Table F.3: ^{28}Si spectrum as a table.

$M_{HY} - M_A$ (MeV)	Counts (/MeV)	$\left(\frac{d\sigma}{d\Omega}\right)$ ($\mu\text{b}/\text{sr}/\text{MeV}$)
130.50	0	.000
131.50	0	.000
132.50	1	.008
133.50	0	.000
134.50	1	.033
135.50	0	.000
136.50	0	.000
137.50	0	.000
138.50	1	.032
139.50	0	.000
140.50	0	.000
141.50	1	.029
142.50	1	.015
143.50	1	.028
144.50	3	.101
145.50	7	.150
146.50	4	.129
147.50	4	.093
148.50	3	.090
149.50	11	.221
150.50	21	.474
151.50	23	.525
152.50	27	.632
153.50	16	.380
154.50	9	.246
155.50	25	.623
156.50	27	.686
157.50	47	1.187
158.50	56	1.238
159.50	45	1.111
160.50	56	1.284
161.50	32	.711
162.50	45	1.038
163.50	56	.858
164.50	78	1.764
165.50	71	1.624
166.50	86	2.054
167.50	77	1.875
168.50	69	1.610
169.50	76	1.781
170.50	91	2.399
171.50	69	2.132
172.50	114	2.775
173.50	112	2.913
174.50	94	2.355
175.50	109	2.564
176.50	123	3.195
177.50	118	2.936
178.50	145	3.262
179.50	137	3.277

Table F.4: ^{86}Y spectrum as a table.

$M_{HY} - M_A$ (MeV)	Counts (/MeV)	$\left(\frac{d\sigma}{d\Omega}\right)$ ($\mu\text{b}/\text{sr}/\text{MeV}$)
150.50	0	.000
151.50	0	.000
152.50	0	.033
153.50	0	.000
154.50	0	.000
155.50	1	.014
156.50	1	.014
157.50	0	.000
158.50	0	.015
159.50	0	.000
160.50	3	.044
161.50	3	.047
162.50	7	.106
163.50	4	.062
164.50	15	.240
165.50	23	.336
166.50	19	.296
167.50	14	.220
168.50	26	.414
169.50	18	.282
170.50	38	.612
171.50	49	.791
172.50	54	.855
173.50	53	.838
174.50	69	1.096
175.50	49	.790
176.50	59	.936
177.50	96	1.351
178.50	114	1.838
179.50	117	1.922
180.50	140	2.231
181.50	89	1.427
182.50	109	1.776
183.50	133	2.159
184.50	160	2.588
185.50	209	3.438
186.50	187	3.040
187.50	174	2.887
188.50	190	3.123
189.50	190	3.126
190.50	223	3.666
191.50	223	3.686
192.50	242	4.004
193.50	241	4.044
194.50	241	4.009
195.50	236	4.284
196.50	248	4.152
197.50	278	4.638
198.50	302	5.151
199.50	283	4.800

Table F.5: $^{139}_{\Lambda}\text{La}$ spectrum as a table.

$M_{HY} - M_A$ (MeV)	Counts (/MeV)	$\left(\frac{d\sigma}{d\Omega}\right)$ ($\mu\text{b}/\text{sr}/\text{MeV}$)
150.50	0	.000
151.50	3	.044
152.50	1	.014
153.50	3	.041
154.50	5	.069
155.50	3	.040
156.50	2	.026
157.50	2	.026
158.50	7	.100
159.50	5	.069
160.50	6	.082
161.50	9	.124
162.50	21	.295
163.50	22	.307
164.50	19	.257
165.50	25	.341
166.50	26	.346
167.50	33	.479
168.50	39	.550
169.50	45	.619
170.50	39	.543
171.50	43	.606
172.50	77	1.070
173.50	89	1.228
174.50	78	1.103
175.50	100	1.413
176.50	93	1.304
177.50	115	1.603
178.50	159	2.251
179.50	149	2.118
180.50	134	1.911
181.50	142	2.020
182.50	178	2.576
183.50	209	2.970
184.50	228	3.236
185.50	248	3.534
186.50	244	3.467
187.50	244	3.495
188.50	234	3.287
189.50	290	4.172
190.50	306	4.431
191.50	303	4.370
192.50	285	4.114
193.50	307	4.455
194.50	318	4.672
195.50	348	5.117
196.50	359	5.241
197.50	363	5.333
198.50	403	5.946
199.50	374	5.417

Table F.6: $^{208}_{\Lambda}\text{Pb}$ spectrum as a table.

Appendix G

S-factors for neutron pick-up reactions

The (π^+, K^+) reaction is analogous to the neutron pick-up reaction in the respect that a neutron hole is produced. Therefore, fragmentations of neutron-hole strengths are expected to be similar to each other approximately. Tables G.1 and G.2 show S-factors measured for neutron pick-up reactions on ^{12}C , ^{10}B , ^{28}Si , ^{89}Y , ^{139}La and ^{208}Pb .

Reaction	J^π	Ex (MeV)	S-factor
$^{12}\text{C}(p, d)^{11}\text{C}$ $E_p=185\text{ MeV}$ [63]	3/2 ⁻	0.00	1.000
	1/2 ⁻	2.00	0.174
	3/2 ⁻	4.80	0.097
	7/2 ⁻	6.49	0.006
	5/2 ⁺	6.92	0.007
	3/2 ⁺	7.53	0.004
$^{10}\text{B}(p, d)^9\text{B}$ $E_p=156\text{ MeV}$ [74]	3/2 ⁻	8.13	0.007
	3/2 ⁻	0.0	0.44
	5/2 ⁻	2.4	0.60
	7/2 ⁻	7.1	0.52
	(7/2 ⁻)	11.5	1.12

Table G.1: Relative S-factors for neutron pick-up reactions on ^{12}C and ^{10}B .

Reaction	Series	Ex (MeV)	S-factor
$^{28}\text{Si}(p, d)^{27}\text{Si}$ [75]	$J^\pi = d_{5/2}^+, l = 2$	0.00	6.8
		2.65	0.9
		2.87	1.6
		4.29	0.7
		6.34	0.9
$^{89}\text{Y}(p, d)^{88}\text{Y}$ [76]	$J^\pi = g_{9/2}^+, l = 4$	0.000	5.2
		0.233	6.9
		1.125	0.19
$^{139}\text{La}(d, t)^{138}\text{La}$ [76]	$J^\pi = h_{11/2}^-, l = 5$	0.737	1.12
		0.823	0.81
		0.836	1.65
		0.900	0.79
		0.937	1.43
		0.962	1.42
		1.067	1.61
$^{208}\text{Pb}(p, d)^{207}\text{Pb}$ [76]	$J^\pi = i_{13/2}^+, l = 6$	1.255	2.66
		1.630	8.5

Table G.2: Relative S-factors for neutron pick-up reactions on ^{28}Si , ^{89}Y , ^{139}La and ^{208}Pb .

Bibliography

- [1] C. Mahaux, P. F. Bortignon, R. A. Broglia and C. H. Dasso, Phys. Rep. **120**(1985)1.
- [2] Th. A. Rijken, Nucl. Phys. **A547**(1992)245c.
- [3] K. Holinde, Nucl. Phys. **A547**(1992)255c.
- [4] M. Danysz et al., Phil. Mag. **44**(1953)348.
- [5] D. H. Davis, Nucl. Phys. **A547**(1992)369c.
- [6] M. A. Faessler et al., Phys. Lett. **46B**(1973)468.
- [7] W. Brückner et al., Phys. Lett. **55B**(1975)107.
- [8] G. C. Bonazzola et al., Phys. Rev. Lett. **34**(1975)683.
- [9] W. Brückner et al., Phys. Lett. **62B**(1976)481.
- [10] W. Brückner et al., Phys. Lett. **79B**(1978)157.
- [11] R. Bertini et al., Phys. Lett. **83B**(1979)306.
- [12] E. H. Auerbach, A. J. Baltz, C. B. Dover, A. Gal, S. H. Kahana, L. Ludeking and D. J. Millener, Nucl. Phys. **A148**(1983)381.
- [13] D. J. Millener, A. Gal, C. B. Dover and R. H. Dalitz, Phys. Rev. C **31**(1985)499.
- [14] H. Tamura, Doctor Thesis, Univ. of Tokyo, December(1987).
- [15] H. Tamura et al., Phys. Rev. C **40**(1989)479.
- [16] H. Tamura et al., Phys. Rev. C **40**(1989)483.
- [17] H. Bandō, T. Motoba and J. Žofka, Int. Journal of Modern Phys. **A5**(1990)4021.
- [18] H. A. Thiesen, AGS proposal, 758 (1980).
- [19] C. B. Dover, L. Ludeking and G. E. Walker, Phys. Rev. C **22**(1980)2073.
- [20] H. Bandō and T. Motoba, Prog. Theor. Phys. **76**(1986)1321.
- [21] T. Motoba, H. Bandō, R. Wünsch and J. Žofka, Phys. Rev. C **38**(1988)1322.
- [22] A. Likar, M. Rosina and B. Povh, Z. Phys. **A324**(1986)35.
- [23] H. Bandō, T. Motoba and Y. Yamamoto, Phys. Rev. C **31**(1985)265.
- [24] C. Milner et al., Phys. Rev. Lett. **54**(1985)1237.
- [25] R. E. Chrien, Nucl. Phys. **A478**(1988)705c.
- [26] P. H. Pile et al., Phys. Rev. Lett. **66**(1991)2585.
- [27] M. Akei et al., Nucl. Phys. **A534**(1991)478.
- [28] D. J. Millener, C. B. Dover and A. Gal, Phys. Rev. C **38**(1988)2700.
- [29] Y. Yamamoto, H. Bandō and J. Žofka, Prog. Theor. Phys. **80**(1988)757.
- [30] Y. Yamamoto and H. Bandō, Prog. Theor. Phys. **83**(1990)254.
- [31] Y. Yamamoto, A. Reuber, H. Himeno, S. Nagata and T. Motoba, Czech. Jour. of Phys. **42**(1992)1249.
- [32] O. Hashimoto et al., KEK 12-GeV PS proposal, E140a (1990).
- [33] O. Hashimoto et al., IL Nuovo Cimento **102A**(1989)679.
- [34] O. Hashimoto et al., eds. T. Yamazaki et al., Perspectives of Meson Science (1992)547.
- [35] K. H. Tanaka et al., Nucl. Phys. **A450**(1986)533c.
- [36] K. L. Brown et al., CERN 80-04(1980).
- [37] M. Ieiri, private communication.
- [38] T. Shintomi et al., IEEE Trans. on Magnetics, Mag-**27**(1992)585.
- [39] T. Shintomi et al., IEEE Trans. on Magnetics, Mag-**28**(1992)805.
- [40] T. Hasegawa et al., Nucl. Instr. and Meth. **A342**(1994)383.
- [41] T. K. Ohsaka et al., IEEE Trans. on Nucl. Sci. **33**(1986)98.
- [42] Table of Isotopes, 7th edition, A Wiley-Interscience Publication.
- [43] Review of Particle Properties, Phys. Rev. D **45**(1992).
- [44] S. Morinobu, private communication.
- [45] H. Grote, CERN/81-03(1981)136.
- [46] J. Myrheim et al., Nucl. Instr. and Meth. **160**(1979)43.
- [47] K. L. Brown et al., CERN 74-2(1974).
- [48] C. B. Dover and G. E. Walker, Phys. Rep. **89**(1982)1.
- [49] B. Schorr, Comp. Phys. Comm. **7**(1974)215.
- [50] K. Itonaga, T. Motoba and H. Bandō, Prog. Theor. Phys. **84**(1990)291.

- [51] K. Itonaga, T. Motoba, O. Richter and M. Sotona, Phys. Rev. C **49**(1994)1045.
- [52] R. E. Chrien, AIP Conf. Proc. No.224, Particles and Fields Series **43**(1991)28.
- [53] T. Motoba and K. Itonaga, private communication.
- [54] T. Motoba, Nuovo Cimento **102A**(1989)345.
- [55] S. Cohen and D. Kurath, Nucl. Phys. **73**(1965)1.
- [56] S. Cohen and D. Kurath, Nucl. Phys. **A101**(1967)1.
- [57] P. G. Roos et al., Nucl. Phys. **A255**(1975)187.
- [58] T. Motoba, AIP Conf. Proc. No.224, Particles and Fields Series **43**(1991)115.
- [59] M. May et al., Phys. Rev. Lett. **47**(1981)1106.
- [60] Y. Yamamoto and H. Bandō, Prog. Theor. Phys. **73**(1985)905.
- [61] M. May et al., Phys. Rev. Lett. **51**(1983)2085.
- [62] M. Tanaka et al., Nucl. Phys. **A372**(1981)173.
- [63] F. Ajzenberg-selove, Nucl. Phys. **A248**(1975)1.
- [64] R. H. Dalitz et al., Nucl. Phys. **A450**(1986)311c.
- [65] M. Jurić et al., Nucl. Phys. **B52**(1973)1.
- [66] R. E. Chrien et al., Phys. Rev. C **41**(1990)1062.
- [67] C. B. Dover, BNL40074(1987).
- [68] K. Amako et al., Nucl. Instr. and Meth. **197**(1982)325.
- [69] H. Wind, Nucl. Instr. and Meth. **84**(1970)117.
- [70] H. Wind, CERN72-21(1972)53.
- [71] J. C. Alder et al., Nucl. Instr. and Meth. **160**(1979)93.
- [72] H. Wind, CERN NP Internal Report 72-S(1972).
- [73] R. E. Chrien et al., Phys. Lett. **89B**(1979)31.
- [74] F. Ajzenberg-selove et al., Nucl. Phys. **A227**(1974)1.
- [75] P. M. Endt et al., Nucl. Phys. **A214**(1973)1.
- [76] Nuclear Data Sheets.

